Defect Characterization of $Cu_2ZnSnSe_4$ Thin Film Solar Cells Using Advanced Microscopic Techniques

By

Mingjie Xu

A dissertation submitted in partial fulfillment
of the requirements for the degree of
Doctor of Philosophy
(Materials Science and Engineering)
in The University of Michigan
2017

Doctoral Committee:

Professor Xiaoqing Pan, Co-Chair, University of California, Irvine
Assistant Professor Emmanouil Kioupakis, Co-Chair
Adjunct Professor George Graham
Professor Wei Lu

Mingjie Xu

mjxu@umich.edu

ORCID iD: 0000-0001-8334-6936

DEDICATION

To my parents Hong Xu and Linghua Hao

& wife Jiachen Chen

ACKNOWLEDGEMENTS

I would like to express my sincere gratitude to my advisor Prof. Xiaoqing Pan for his continuous support and expert guidance throughout my PhD study. I would also like to express my appreciation to Prof. George Graham, Prof. Emmanouil Kioupakis, and Prof. Wei Lu for having served on my committee.

All the work in this thesis wouldn't be possible without the help of numerous friends and colleagues. I would like to thank Dr. Yi Zhang (younger), Dr. Linze Li, Dr. Jacob Jokisaari, Dr Sheng Dai for their insightful comments and contribution on my work. I would also like to thank Dr. Toshihiro Aoki and Dr. Jianguo Zheng from Irvine Materials Research Institute (IMRI) who trained me in TEM and other scientific instruments.

The work has been done in close collaboration with IMRA America, Inc. I owe a deep sense of gratitude to Dr. Wei Guo and Dr. Bing Liu for introducing me into the field of thin film solar cell.

Table of Contents

LIST OF FIGURES

LIST OF TABLES

ABSTRACT

Thin film chalcogenide solar cells have been utilized in a broad range of application for their tunable direct bandgap and high efficiency. In this work, we performed a novel fabrication and multiple high-resolution characterizations of $Cu_2ZnSnSe_4$(CZTSe) solar cells, which is believed to be a better candidate compared to well-developed $CuIn_xGa_{(1-x)}Se_2$(CIGS)for its earth-abundant contents. The fabrication is based on nanoparticle precursor production by liquid-phase pulsed laser ablation, electrophoretic deposition of precursor thin film under ambient condition, and selenization. Such non-vacuum fabrication has the advantage of low cost and minimum impact on the environment.

By studying the CZTSe and CIGS fabricated in the above methods using techniques including Raman integrated scanning probe microscope, electron holography, scanning transmission electron microscopy and in-situ transmission electron microscopy. We discovered the origin of the performance limit of the CZTSe compared to CIGS as well as the defect of our non-vacuum fabrication methods. The presented results, including the characterization methods, create a novel way to correlate the solar cell performance with the microstructure in a nanometer scale. It opens up the possibility for developing high performance solar cell devices from the prospective of nanostructure and defect engineering.

Chapter 1

Introduction

1.1 Thin film solar cells from earth abundant materials

The energy production industry is facing challenges brought by the increasing risk of global climate change. Emissions of CO_2, generated during combustion of fossil fuels such as coal, oil, and natural gas, need to be reduced, which means that current sources of energy need to be replaced by carbon-free energy sources. Current world energy consumption is 18 terawatts (TW), and by the end of 2050 it is expected to reach 30 TW. To maintain a CO_2 concentration below 450 ppm, the maximum allowable contribution of fossil fuel power should not exceed 8 TW. Carbon-free energy sources will thus have to provide 22 TW by 2050 if this target concentration of CO_2 is to be attained.[1]

Solar power is the most abundant renewable energy source on Earth, supplying the amount of energy equivalent to annual human consumption in just one hour radiation.[2] The solar energy reaching the Earth's surface per year (3.85 YJ)[3] is approximately twice the accumulation of all Earth's non-renewable energy resources can provide.[4] However, compared to its enormous capacity, solar energy is currently a "niche" renewable source that remains a minor share in the world's energy supply map, mainly through the form of light-to-electricity conversion in solar cells. The obstacles hindering the extensive use of solar energy include the lack of a sustainable and high-throughput photovoltaic (PV) power generation technology, the high construction cost of PV facilities, and the intermittent nature of solar energy which requires matching energy storage method.[5]

Since the development of the first practical silicon (Si) solar cell in the 1950s,[6] extensive efforts have been devoted to searching for alternative solar absorbing materials, among which two principle materials, CdTe[7, 8] and $Cu(In,Ga)Se_2$(CIGS),[9, 10] have been proposed to be more efficient and more cost-effective than Si.

Due to their direct bandgap that can be optimized to 1.5 eV to match the solar spectrum and their high adsorption coefficients ($>10^4$ cm^{-1}) and high internal quantum efficiencies,[11] thin film solar cells based on these two materials have a higher thermodynamic limit of power conversion efficiency (PCE) (at about 30%) than Si for single-junction cells, and the absorber layer thickness can be controlled to within 1-2 µm, which is thinner than that of Si cells by an order of magnitude.[12] PCE of lab-scale CIGS thin film solar cells has reached 20.3% in 2011 fabricated by vacuum-based deposition.[13-15] In the meantime, commercialized thin film solar panels are generating PV power as much as a few gigawatts per year.[16, 17]

However, when aiming at a terawatt-scale PV energy production to meet the world's energy demands, the current thin film solar cell technologies are facing crucial challenges, such as the high cost of vacuum deposition systems, toxicity of Cd, and the limited global supply and the consequent high prices of In, Ga, and Te.

In these regards, there is a surge of interest recently in developing $Cu_2ZnSn(S,Se)_4$ (CZTS) as the light-absorbing material. As the sister chalcopyrite of CIGS, CZTS is ideal in both ecological and economical aspects, because all constituent elements are non-toxic, and the precious In and Ga are replaced by earth-abundant elements Zn and Sn.

In order to have significant impact on future energy infrastructure, however, TW-scale deployment of photovoltaic technology is needed, which requires a massive amount of raw materials and energy[18]. Table 1 shows the limitations and maximum energy production of the three major commercialized solar cell technologies. By the year 2100, the combined impact of all three technologies could provide no more than 4% of the total energy demand[19]. In practice, the combined power production available from PV would be only about 300 GW-peak (GWp) per year, which is significantly lower than the 2.4 TWp/year required for 60 TWp steady-state installation. Hence, none of the currently commercialized technologies will meet the requirements for TW-scale deployment, for that the absorbing materials should be of low cost, non-toxic, earth abundant while still has competitive energy conversion efficiencies compared to the traditional solar cell systems.

Table 1. Estimated, best-scenario maximum wattages for current commercial solar cell technologies based on the reserve of the limiting material in each technology[19]

Technology	Limiting material	Reserve (metric ton)	Maximum wattage	Averaged output	% of 2100 energy demand
Wafer-Si	Ag	540,000	10.3 TW_p	1.03-2.06 TW	3.3
CdTe	Te	24,000	492 GW_p	49-98 GW	0.16
CIGS	In	11,000	1.1 TW_p	110-220 GW	0.34

Thin-film Si is not listed as it competes for In with CIGS and Ag with wafer Si

Given the TW-scale PV energy production needed to meet the world's energy demands and the consistent pressure to reduce module prices in the future, the current thin film solar cell technologies are facing additional crucial challenges, such as high cost of vacuum deposition systems, toxicity of Cd, and particularly the significant material constraints of earth-rare elements In, Ga, and Te. Consequently, a market shakeout has stricken several thin film PV companies since 2009, when the price of Si-based PV modules collapsed due to technology innovation and overproduction. In these regards, surging interest has recently occurred to develop low cost PV technologies based on truly earth-abundant materials, such as organic, dye-sensitized, and inorganic $Cu_2ZnSn(S,Se)_4$ (CZTS). Due to the similarity in the crystal structures and bonding characteristics between CZTS and CIS, the two materials are expected to have similar electronic structures, and indeed, they have a similar bandgap of ~1.5 eV and a band-edge absorption coefficient of above 10^4 cm^{-1}.[20] CZTS is considered promising as a low-cost alternative to CIGS.

As the sister chalcopyrite of CIGS, CZTS is superior to Si, CdTe and CIGS because it is made of low cost, earth abundant elements such as Cu, Zn, Sn, S, and Se. The annual production of Cu, Zn, Sn, S, and Se are 17,000, 13,000, 230,000, 70,000, and 2000 metric tons/year, respectively. This allows production of CZTS modulus on the order of 1.4 TWp/year, which is 20 times larger than CIGS, assuming similar PCE.

1.2 Background of CZTSe Solar cell

CZTS is a quaternary compound with the kesterite structure which is derived from the chalcogenide zinc blende structure via sequential cation mutations (cross-substitutions).[21] In the zinc blende structure, cations (e.g. Zn) and anions (e.g. S and Se) occupy two interpenetrating *fcc* lattice sites, respectively. By substituting Zn of group II with Cu of group I and In of group III, the structure evolves to the I-III-VI_2 chalcopyrite $CuIn(S,Se)_2$ (CIS) structure with unit cell doubled along the c-axis. By further substituting In with ordered Zn of group II and Sn of group VI, it evolves to the I_2-II-IV-VI_4 kesterite CZTS structure. Figure 1 shows the evolutionary relationship between the binary ZnS, ternary CuInS2, and quaternary Cu2ZnSnS4.

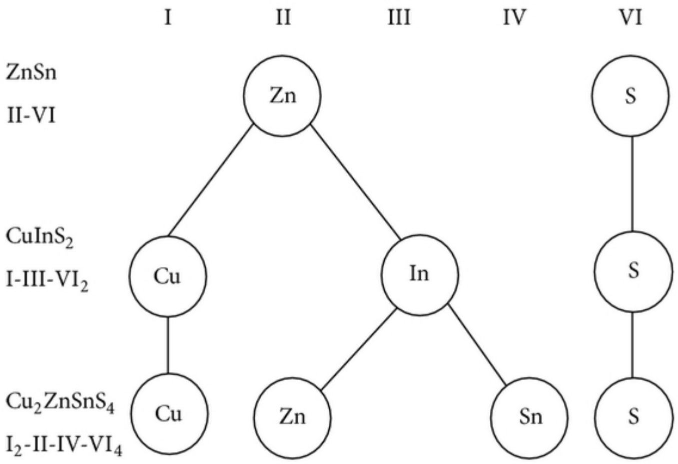

Figure 1 Relationship between binary, ternary, and quaternary semiconductors to produce Cu2ZnSnS4, starting from a II–VI parent compound[22].

By changing the arrangement of Cu and Zn, Cu2ZnSnS4 can form two different structures: Stannite and Kesterite. The evolution from Chalcopyrite CuInSe2 to Stannite Cu2ZnSnS4 involves the Cu-In layer being replaced by an alternation of Cu-Cu and Zn-Sn layers, with two Cu atoms located at 2a and 2c position, and the Zn atom located at 2d position; the evolution from Chalcopyrite to Kesterite CZTS involves the Cu-In layer being replace by alternating Cu-Zn and Cu-Sn layers, with both Cu atoms located at 4d position and the Zn atom located at 2a position. In both cases, Sn atom is located at 2b position [23, 24].The two different structures are shown in Figure 2. It is still controversial whether CZTS is naturally found in kesterite phase or stannite phase. Some suggested that the CZTS is most stable in kesterite[22, 24-29], while other people found it to be the opposite case[30, 31]. Nateprove et al. suggested that the partial disorder of Cu and Zn in the Cu-Zn layer of the kesterite structure may lead to a crystal symmetry change from $I\bar{4}$ to $I\bar{4}2m$, which is the same as that of stannite structure. The difficulty to distinguish between the kesterite and stannite CZTS using the traditional methods, for example X-ray diffraction, is that the structural properties and electronic properties of Cu and Zn ion are very similar. However, recent study using neutron diffraction and anomalous diffusion has confirmed that CZTS is more stable in the form of kesterite structure[32, 33], and the observation of stannite structure is indeed due to partial disorder of Cu and Zn in the Cu-Zn layer[32, 34, 35].

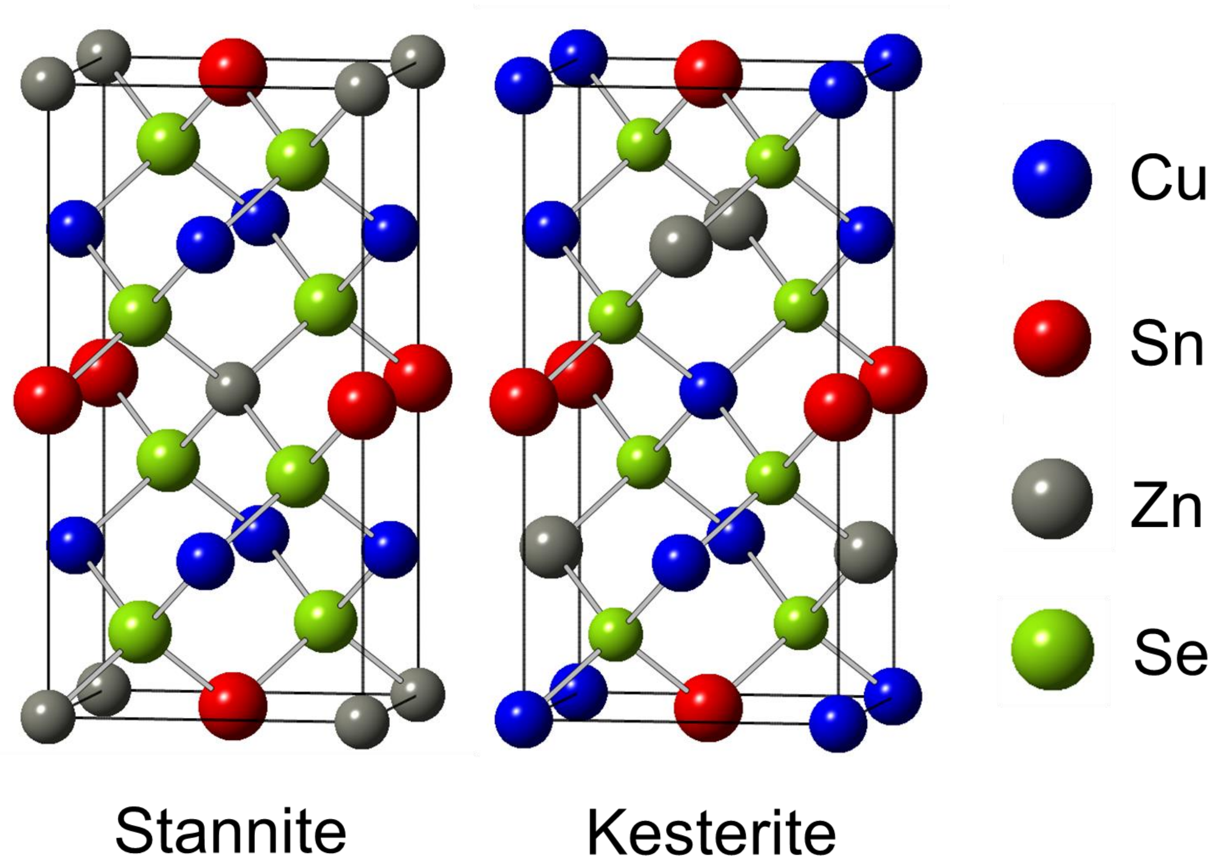

Figure 2 Crystal structure of a Stannite CZTSe and a Kesterite CZTSe.

Compared to silicon, metal chalcogenides usually have direct bandgaps and thus exhibit much higher light absorption coefficient[36]. In addition, the ability to tune the band gap by metal and/or chalcogen substitutions offers the ability to achieve the optimum band gap for the solar spectrum[37].

The Band gap of Cu_2ZnSnS_4 (CZTS) and $Cu_2ZnSnSe_4$(CZTSe) are 1.5 eV and 1.0 eV. When doping CZTS with Se, the bandgap can be tuned depending on the concentration of Se. Researches has shown that for $Cu_2ZnSnS_{4-x}Se_x$, the band gap follows the linear rule of doping[37]:

$$E_g(eV) = -0.5x + 1.5$$

The ability of tuning the band gap gives new approach towards high efficiency. Yang et al. reported that a 12.3% efficient CZTSSe has been achieved using gradient S/Se ratio[38].

Figure 3a. a cold rolled Mo sheet is used as the standard back contact. The p-type CZTSe absorber layer with thickness of 2 μm is grown on the Mo film. A thin layer of n-type CdS layer with 50nm thickness is deposited on the CZTSe film. Subsequently, a 50 nm ZnO window layer and a 300 nm indium tin oxide (ITO) layer, serving as transparent conductive oxide (TCO), are sputtered on top of the CZTSe subsequently. Finally, Ni/Au grid lines are thermally evaporated on top of the ITO layer as top contacts. An MgF2 anti-reflection coating is usually deposited on top of the cell to capture the incident light more efficiently, but is not used in our devices.

Since the a CZTS solar cells that has 0.66% PCE has been reported in 1988 by Ito et al.,[39] The highest efficiency for CZTS solar cells has reached 12.6% in 2014. [40]

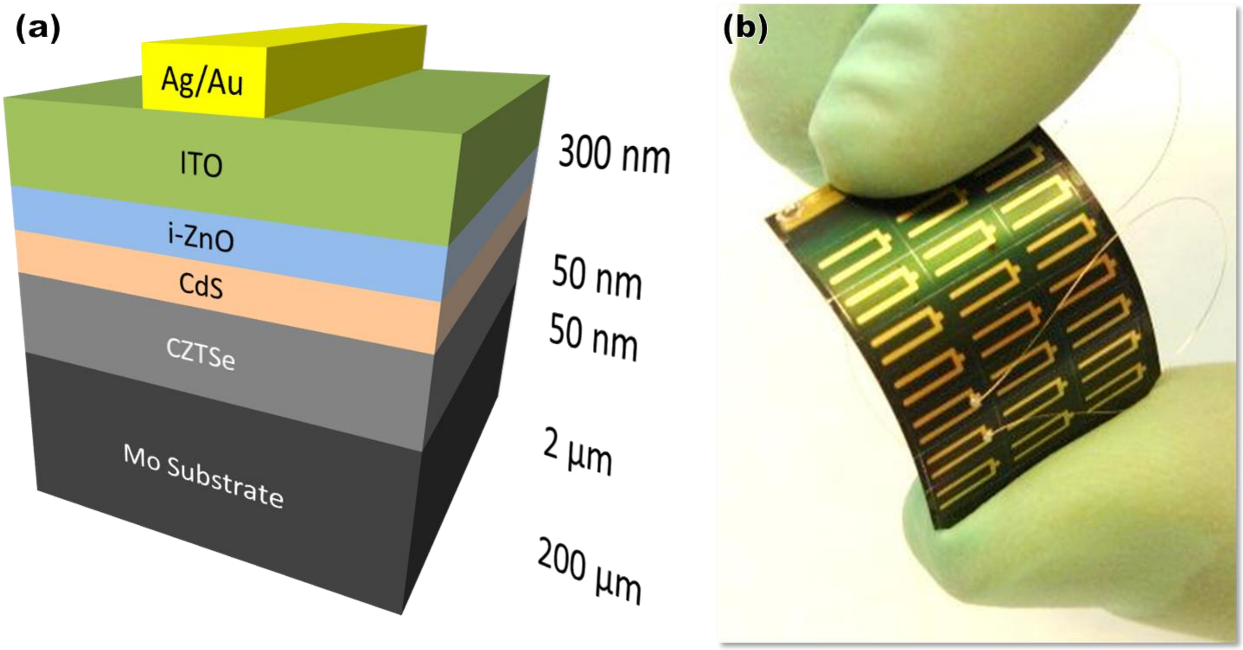

Figure 3 Device structure of CZTSe (a) is a schematic of a CZTSe thin film solar cell device. (b) is the CZTSe thin film solar cell array grown on a flexible Mo substrate.

1.3 Non-vacuum synthesizing of CZTSe Solar cell devices

Rapid progress in synthesizing CZTS thin films and fabricating CZTS solar cells has been made in the past several years. It is especially interesting to see that, in addition to traditional vacuum-based thin film deposition processes such as thermal co-evaporation,[41, 42] co-sputtering,[43, 44] and hybrid electron beam evaporation,[45] various non-vacuum fabrication approaches have been developed, including hydrazine-based solution spin coating,[46-49] synthesis of nanocrystals,[50-52] and electroplating[53, 54]. In 2012, PCE of lab-scale CZTS solar cells fabricated by solution-based methods has reached the benchmark 11%, undoubtedly putting CZTS as a strong competitor to CdTe and CIGS.[49] The interesting fact that recent fabrication of high-efficient CZTS absorber layer does not rely on vacuum deposition suggests a promising possibility of low-cost fabrication technology for high-throughput PV production. These progresses have made the newly emerged CZTS solar cell to be included in the famous worldwide "Research Cell Efficiency Records" roadmap maintained by the National Renewable Energy Laboratory (NREL),[51] and its performance is expected to improve rapidly given the currently worldwide intense research effort.

In contrast to vacuum deposition processes, use of nanoparticle precursors and electrophoretic deposition (EPD), developed by our collaborators in IMRA, provides a non-vacuum technology that is energy efficient while producing minimal material waste. Colloidal nanoparticles of metallic Cu, Zn, Sn or their alloys are synthesized with liquid phase pulsed laser ablation in appropriate solvents. This method has proven to be an expedient way of fabricating high quality colloidal nanoparticles of many metals and compounds in various solvents.[55] Significantly, the nanoparticles are stabilized with electric charge acquired in the laser-induced plasma, and thus additional stabilization agents are not needed, thus ensuring a high purity colloid into which dopants may precisely be added when desired. Precursor CuZnSn (CZT) thin films are fabricated using EPD.[56] The deposition is facilitated by the electro-kinetic mobility acquired by the electrically charged nanoparticles under an external electric field applied in the solvent. The particular advantage of EPD is the high deposition rate, in the micron/min range. CZTS or CZTSe films are obtained following standard sulfurization or selenization procedures, respectively. Using this unique approach, our preliminary studies at IMRA have demonstrated that CZTS solar cells may be fabricated on flexible substrates that have 4.8% efficiency (Fig. 2c).

This unique method for fabricating CZTS solar cells has the particular advantage of fast processing due to the non-vacuum synthesis of high purity nanoparticles and high-speed deposition of precursor thin films. Fabrication of lab scale cells can be performed in about 1 day, which is 2-3 times faster than vacuum deposition and chemical synthesis methods. This will significantly reduce the screening time needed for identification of critical process parameters. We anticipate that the quality of CZTS films and related devices will be improved by optimizing the composition, especially the Cu/(Zn+Sn) and the Zn/Sn ratios and the quality of the interface between CZTS and the Mo substrates or by mixing Se with S, which is generally accepted as the best way to optimize the optical band gap of CZTS.

1.4 Development of CZTSe solar cells and challenges

With just a few years of research, IBM's researchers improved CZTS lab-scale solar cell efficiency to the 11% level in 2012.[49] Such unforeseen success has subsequently stimulated huge interest and rapid progress in CZTS solar cell processing research. The best cell efficiency for CZTS so far achieved is 12%, by Winkler et al.[57], using hydrazine-processed devices. It is especially interesting to see that, in addition to the traditional vacuum-based thin film deposition processes such as thermal co-evaporation,[41, 58, 59] co-sputtering,[43, 44] and hybrid electron beam evaporation,[45] various non-vacuum fabrication approaches have been developed to fabricate the CZTS converter layers, including hydrazine-based[46-49] or other organic solution based[60] spin coating processes, synthesis of nanocrystals,[50-52] and electroplating.[53, 54] These non-vacuum approaches have generally demonstrated higher lab-scale PCEs (5%-11%) than contemporary vacuum deposition methods. In addition, these non-vacuum based technologies have shown their potential to be applicable to roll-to-roll mass production on light-weight and/or flexible substrates. The incredible fact that an efficient CZTS converter layer does not rely on vacuum-based fabrication has opened up the exciting possibility of realizing a truly low-cost and high-throughput thin film PV technology that is competitive with the Si-based technology. This progress has led to the newly emerging CZTS solar cell being included in the worldwide "Research Cell Efficiency Records" roadmap maintained by the National Renewable Energy Laboratory (NREL),[61] and its performance is expected to improve further, given the current worldwide intense research effort.

However, compared with the encouraging short-term success in CZTS solar cell research, fundamental studies on the CZTS material and devices, especially structural and chemical characterization at the atomic scale, are severely lacking due to the material complexity. One of the fundamental issues with CZTS is its narrow composition window (<2% deviation) of thermodynamic stability,[62, 63] which typically results in a multitude of secondary and ternary impurity phases during fabrication,[54, 58, 64] especially when a strict composition control is lacking.[58, 65] An even more challenging issue is that of defects in the material, including defect formation, properties of intrinsic point defects, defect complexes, grain boundaries and their electrical characteristics (often controversial according to theoretical and experimental reports).[15, 66-73] There are also device fabrication issues that require knowledge about atomic level structure and properties of defects and interfaces, such as the structure, spatial distribution, and stability of defects and grain boundaries, their dynamic behaviors under applied field, and the effects of residual carbon impurities[51] introduced during many of the non-vacuum coating processes, as well as the formation of voids at the back contact interface during annealing treatment.[48]

Any prediction of the long-term marketability of CZTS PV technology solely based on lab success without a complete understanding of the material, the device, and structure-property relationships in device fabrication and aging has significant risk. It is therefore imperative to characterize the microstructure and defects of CZTS films for precise understanding and possible better material synthesis and property control. In particular, understanding of the atomic structure and local properties of interfaces and defects at the atomic scale will provide extremely important insight into the role of defects in device performance, which has been controversial in its sister chalcopyrite material CIGS.

Due to lack of information on defect formation mechanisms and precise control of phase separation, synthesis of high quality CZTS film is a complicated task. Previously, most CZTS devices that demonstrate high efficiency were synthesized using non-vacuum deposition techniques. These non-vacuum methods are also believed to be more favorable due to the cost reduction and better composition control. Todorov et al. [47] reported 11.1% efficiency CZTSSe solar cells using spin coating of precursor ink containing Cu-Sn chalcogenide solution and Zn chalcogenide particle suspension followed by a post-coating annealing process to remove the excess binding agent. This was recently improved to 12% by engineering the thickness of top coatings to enhance short-wavelength absorption[57]. However, despite having the highest efficiency, this fabrication process includes use of hydrazine (N_2H_4), which has high reactivity, flammability and is hazardous to health. The requirements for handling the precursor materials and a laborious fabrication process will hinder the commercialization of this process. Other studies using low-toxicity solutions or nanoparticles have reached efficiencies larger than 8%. Guo et al.[74] achieved 8.4% efficient CZTGeS using multinary sulfide nanocrystal inks. Vacuum based techniques such as sputtering and evaporation have made significant progress within the last two years. Chawla et al. reported 9.3% efficient CZTSSe using co-sputtering of compound targets[75]. Buffiere et al. reported efficiencies of 9.7% for CZTSe produced by sputtering $Cu_{10}Sn_{90}$, Zn and Cu multilayers[76] and Repins et al. reported to have 9.15% efficiency in CZTSe using co-evaporation[77].

Compared to non-vacuum techniques, sputtering and evaporation usually produce superior film qualities. Non-vacuum methods usually include post-annealing of precursor ink or solution which can leave voids and residual binding agent near interface of film and back contact which can significantly reduce the adhesion and impede hole collection. It is clear that many synthesis techniques are under active development. Before one can compare technologies and predict the marketability of CZTS thin film PVs, it is necessary to completely understand the material and properties, optimize and regulate the fabrication process, and improve the device reliability.

Chapter 2

Transmission Electron Microscopy (TEM) and Scanning Probe Microscopy(SPM) on solar cells

2.1 Preparation of solar cell TEM specimen using different techniques

The sample preparation is the key to high quality TEM imaging. In order to be electron transparent, the sample needs be less that 100nm in the beam direction. And for high resolution imaging this value needs to be even smaller. Additionally, the surface must be smooth, and free of contamination such as adsorbed organics, water, solvents, or similar substances.

A few methods have been developed to prepare a high-quality TEM specimen and they have become more specialized and sophisticated[78-80]. In this work, the CZTSe TEM specimen are prepared in three different methods: hand polishing, particle dispensing, and focused ion beam (FIB).

2.1.1 Sample preparation using hand polishing technique

The most commonly used technique of ceramic materials is the traditional hand polishing technique. this method involves the film being glued to a sacrificial silicon, mounted to a tripod polisher and hand polished to less than 1μm. After that the film will be iron milled by PIPS until the desired thickness is reached. The ion milling step in Gatan PIPSII removes most contaminants and provides a very thin and smooth surface. However, a thin amorphous layer of ion beam induced damage can be introduced on the surface of the sample. In the case of CZTSe device, a layer of MoSe2 is formed between the CZTSe and the Mo substrate during the selenization process and thus makes the adhesion between the film and the substrate very week. To prevent the delamination during the hand polishing and ion milling, the film was lift out and laminated between two sacrificial Si wafers. The advantage of this method is that it allows one to prepare samples with high quality, low contamination, and low cost. However it usually consumes a large amount of sample to prepare one TEM specimen and the area of interest can’t be controlled for anisotropic films.

2.1.2 Sample preparation using powder dispensing technique

For in-situ measurements, especially the ones that involves electrical measurements, the absence of the substrate in the hand polishing methods makes it difficult to form a close loop for that the film is stand-alone and the glue and the Si wafer are all non-conductive. An easier way to do is to disperse the CZTSe crystals inside a solvent and transfer them on to a Cu half grid. During this process, a certain amount of crystals will be sit on the edge of the Cu grid, thus the probe, sample and the Cu grid can form a close loop for the in-situ electrical measurements.

However, for the particle methods, there is no control over the orientation, grain size and thickness. Besides, since the concentration of the particles needs to be high enough for them to be found at the edge of the Cu half grid, the in-situ experiment will be difficult to interpret when you have a group of randomly distributed particles around the area of interest.

2.1.3 Sample preparation using FIB

FIB method, on the other hand, has more control over the specimen size and orientation. One can select the region of interest and lift out a FIB sample with the direction well defined. The thickness is also more uniform.

When preparing sample using FIB, a focused Ga ion beam is used to for both etching and deposition/welding purposes. A specimen of 15μm×3μm×5μm was cut by the ion beam. A probe is then used to transfer and the specimen to a Φ3 lift-out grid. After being welded to the grid using the ion beam induced Pt deposition, the specimen is thinned and polished by the ion beam until electron transparent. Figure 4 shows the SEM and STEM imaging of sample preparation using FIB in different stages. The issue with the FIB method however, is that the beam damage during the thinning process as well as the contamination of gallium on the surface of the sample. The e-beam/ion beam induced damage usually forms amorphous region at the surface of the sample. And will form shunting paths when combined with Ga contamination. Thus to make a good FIB sample that is suitable for in-situ electrical measurement, the sample needs to be carefully cleaned after FIB using other techniques such as Nanomill ion polisher.

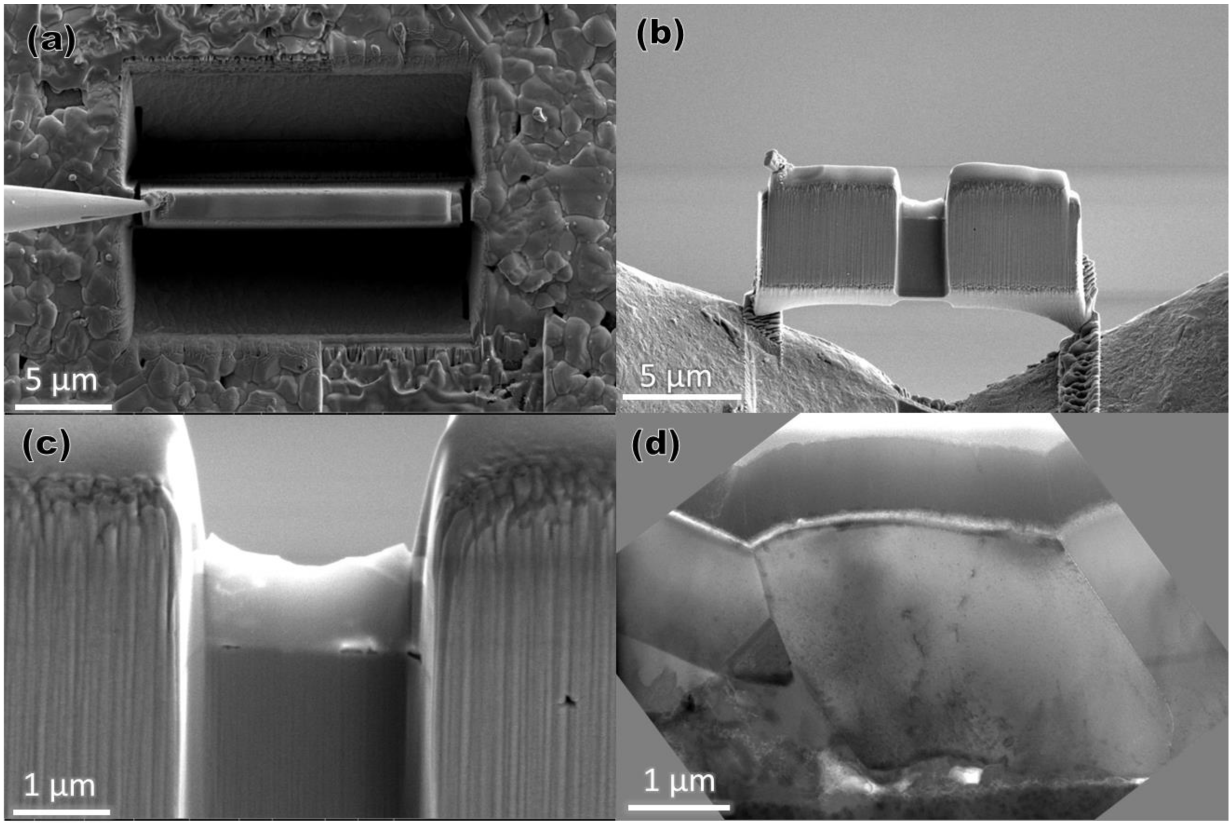

Figure 4 Process of TEM sample preparation using FIB. (a) shows the SEM imaging of a slice of CZTSe sample being welded to a probe before lift-out. (b) shows a SEM imaging of the sample being welded to the TEM lift-out grid, and the center being thinned down. (c) is a zoomed-in view of the center region in (b), and (d) is the STEM BF imaging of the region in (c).

2.2 Scanning Transmission Electron Microscopy (STEM) and X-ray Energy Dispersive Spectroscopy (EDS)

To study the atomic-scale mechanism of the CZTSe solar cell, advance aberration-corrected(Cs-corrected) STEM imaging with sub-angstrom resolution is required. The traditional high resolution TEM (HRTEM) imaging which is also known as phase-contrast imaging, doesn’t generally reveal the real atomic structure because the phase contrast imaging is complicated to interpret. Furthermore, the phase contrast imaging is highly sensitive to dynamic effects such as the sample thickness variation, tilting, and orientation. Compared to HRTEM, STEM is much more straight forward to use when studying the CZTSe solar cells for the imaging is much easier to analyses and its ability to acquire multiple analytical spectroscopies simultaneously.

In STEM mode, a converged beam is used as a probe to scan on the sample. This process is much like that of a conventional SEM, only that STEM uses much higher beam energy. When combined with the condenser lens aberration corrector. The probe size will be small enough for atomic resolution imaging. Furthermore, unlike conventional SEM, STEM not only collect secondary electron beam, but also transmitted and scattered beams. Besides the bright field imaging, the scattered transmission electrons are collected by a ring-shaped detector. Depending on the annular angle, one can acquire high-angle annular dark field (HAADF) imaging, annular dark field (ADF) imaging, and annular bright field imaging (ABF). The HAADF imaging is the most commonly used technique in STEM for that the intensity contrast (C) of the HAADF imaging is proportional to the Z-contrast factor ($Z^{1.7}$) where Z is the atomic number of the element[81]. In the CZTSe systems, heavy atoms such as Sn will have a much brighter contrast and can be easily distinguished.

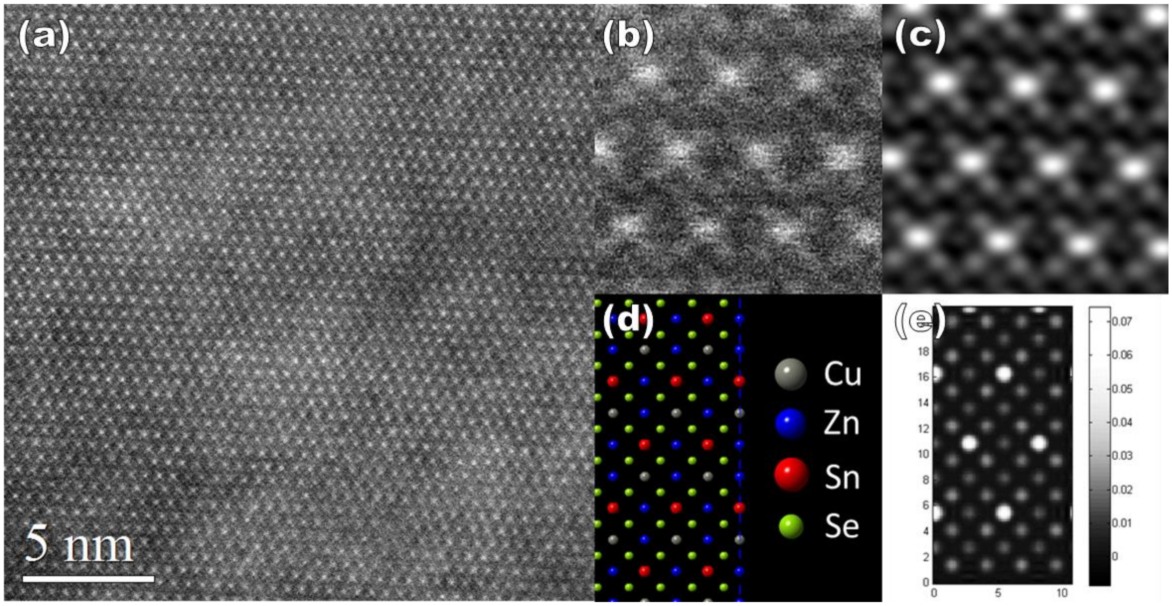

Figure 5 Atomic resolution imaging if CZTSe. (a) is a STEM HAADF image of a CZTSe single crystal at [100] zone axis. (b) is an enlarged field in (a); (c) is a FFT filtered image of (b); (d) is the model of the corresponding structure, and (e) is the simulation of the HAADF imaging of the structure in (d) using the QSTEM software.

One advantage of using the STEM mode is that one can collect several types of data simultaneously during a single acquisition such as secondary electron imaging (SEI), x-ray energy dispersive spectroscopy (EDS) mapping, and electron energy loss spectroscopy(EELS) mapping. The major techniques that are used in this work were STEM HAADF imaging, BF imaging and EDS mapping.

EDS spectroscopy in TEM is a powerful characterization method so study the chemical composition variation of materials. In TEM, the electrons that occupies the inner shells are ejected by interacting with highly accelerated electron beams. As an electron is excited, an electron hole forms at its position and will soon be fill by an electron that occupies a high, outer energy shell. During this process, the difference between the outer and inner energy shell will be emitted in the form of a characteristic x-ray photon. Depending on the position of the hole and the electron that fills it, multiple characteristic x-rays may be generated from a single atom. The emitted x-ray photons are collected by the EDS detector and a spectrum of intensity versus x-ray energy is acquired.

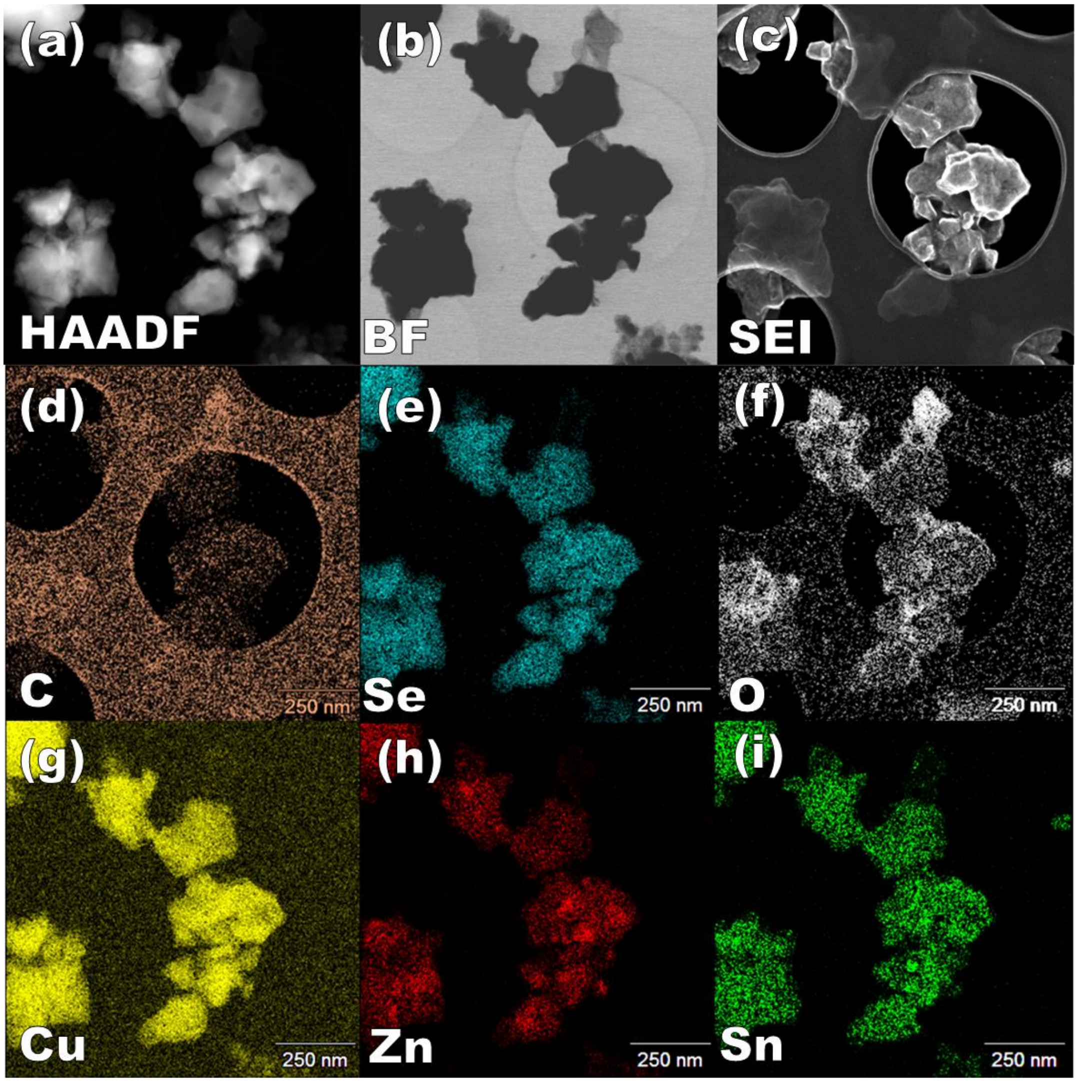

Figure 6 EDS mapping of CZTSe particles.(a) HAADF imaging, (b) BF imaging, (c) SEI imaging, (d)-(i) EDS mapping can be acquired in STEM simultaneously.

2.3 TEM imaging and Off-axis electron holography

In the TEM mode, a parallel electron beam is used to pass the specimen and form phase contrast imaging. When the objective aperture is inserted, one can also acquire diffraction contrast imaging. It is also capable of doing selected area electron diffraction (SAED) that contains the crystallography information.

Another commonly used imaging method is called the diffraction-contrast imaging, also known as “dark-field/bright-field” imaging. Compared to the normal TEM imaging, for example phase contrast imaging, where the image contrast comes from the interference between the transmitted and diffracted electron wave, the contrast in the diffraction-contrast imaging comes from a certain amount of diffracted electron beam that is chosen by the aperture at the back focal plane. When the incident electron beam exit from the sample, a fair amount of beam is diffracted and form diffraction spot on the back focal plane. Each diffraction spot consists of the electrons that are diffracted by a specific plane, which means that when selecting a diffraction spot with the objective aperture located at the back focal plane, the final image will highlight the region that contains the information of the plane that corresponds to the diffraction spot. This technique allows one to highlight structures such as adjacent grains sharing low Σ twin boundaries, which is usually hard to be seen using regular imaging methods. In addition, diffraction contrast imaging also highlights small precipitations and dislocations, which are commonly found in thin film CZTS solar cell materials.

The off-axis electron holography is commonly used for mapping the potential distribution at nanoscale. Hence it can play an important role in characterization of electrical properties in the CZTSe solar cell system. When doing off-axis electron holography, an interference pattern is formed at the image plane by superimposing the exit-plan waves(EPW) with a reference wave that passes through vacuum. Such interference can be achieved using a Möllenstedt biprism[82]. A Möllenstedt biprism is a positively charged filament that is located below the specimen. When the electron beam passes through this plan, the two parts of the beam are deflected towards each other and form a hologram at the region of interference. The image wave $\mathrm{img}(\vec{\mathrm{r}})$ at the image plane may be expressed by:

$$img(\vec{r}) = FT^{-1}[FT[obj(\vec{r})]WTF(\vec{q}) = A(\vec{r})\,exp\big(i\phi(\vec{r})\big),$$

Where FT and FT^{-1} are Fourier and inverse Fourier transformation, WTF is the wave transfer function, and A and $\phi(\vec{r})$ are amplitude and phase of $\mathrm{img}(\vec{\mathrm{r}})$. The detector on the image plane, however, can only record the beam intensity as the function of the amplitude part of the image wave:

$$I(r) = |img(\vec{r})|^2 = A^2(r).$$

Therefore, in conventional TEM, a considerable information regarding the phase information of the image wave is lost. For example, in medium-resolution imaging scale, the object phase shift caused by magnetic or electrical field variation of dopant, grain boundaries or other structure in semiconductors are virtually invisible to the conventional imaging techniques.[83, 84] The development of electron holography enables the ability to record both phase $\phi(\vec{r})$ and amplitude $A(\vec{r})$. This is achieved by recording the interference of the image wave and a coherent wave. The interference pattern is called hologram and contains the information of both $\phi(\vec{r})$ and $A(\vec{r})$. This idea was proposed by Gabor in 1948[85], and is realized in TEM by Möllenstedt et al. in 1956 using the technique called off-axis electron holography[82].

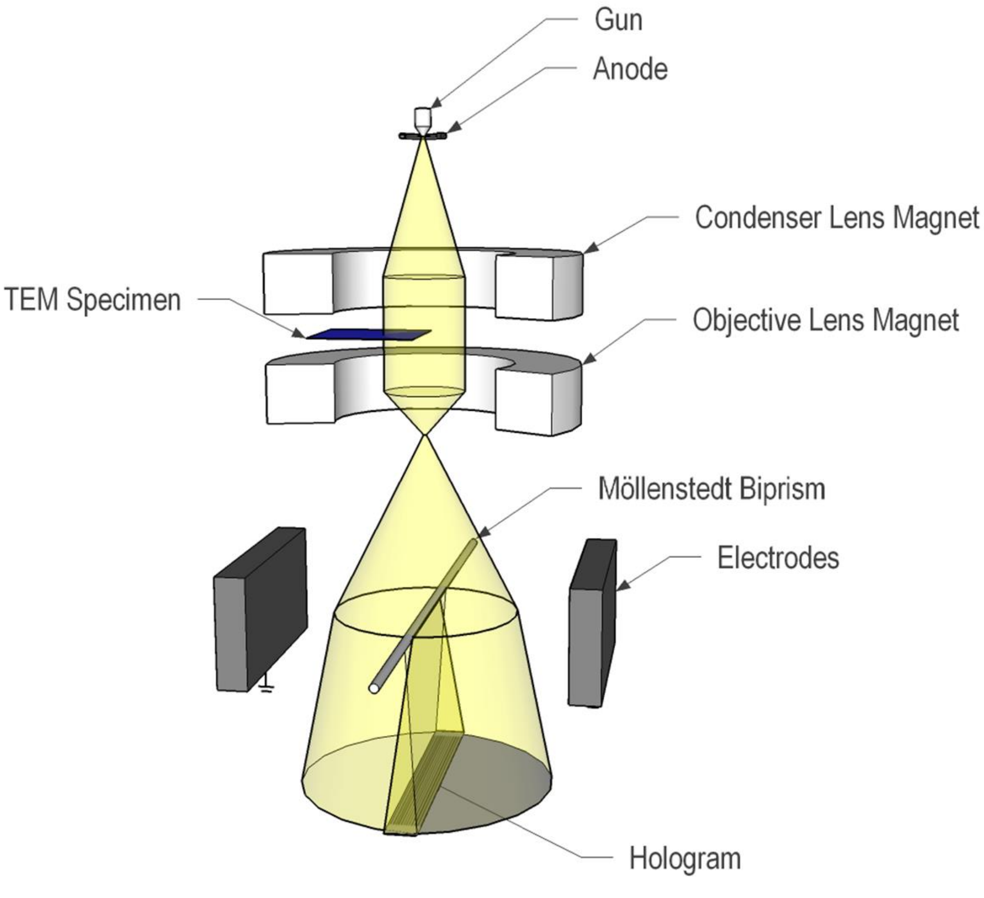

Figure 7 A schematic of the setup of a Möllenstedt biprism inside a TEM.

The biprism system consists of two parts: a positively charged conductive filament and a pair of grounded electrodes. Because of the positive voltage being applied to the filament, it has the ability to split the wave front of an incoming electron wave into two coherent partial waves and deflect them towards each other. The two partial waves are then superimposed at the imaging plan to form the hologram (Figure 7). The intensity distribution of the hologram is:

$$I_{holo}(\vec{r}) = 1 + I_{elast}(\vec{r}) + I_{inelast}(\vec{r}) + 2\mu A(\vec{r})\, cos\big(2\pi\vec{q}_c\vec{r} + \phi + \gamma(\vec{r})\big),$$

where $\vec{q}_c \approx k_0\beta$ is the carrier spatial frequency of the interference fringes, and μ is the fringe contrast. $I_{elast}(\vec{r})$ and $I_{inelast}(\vec{r})$ are the intensity caused by elastically and inelastically scattered electrons. The phase shift $\gamma(\vec{r})$ consists distortions caused by the instrument and can thus be corrected by acquire a hologram of vacuum region under the same condition:

$$I_{vacuum}(\vec{r}) = 2\big(1 + \mu\, cos\big(2\pi\vec{q}_c\vec{r} + \gamma(\vec{r})\big)\big).$$

The phase $\phi(\vec{r})$ and amplitude $A(\vec{r})$ can be derived from the above two holograms by the follow procedure. The Fourier transformation of the hologram $I_{holo}(\vec{r})$ is the complex form:

$$FT\{I_{holo}(\vec{r})\} = \underset{Centerband}{FT\{1 + A^2(\vec{r})\}} + \underset{Sideband\,+1}{\mu FT\big\{A(\vec{r})e^{i\phi(\vec{r})}\big\}\otimes\delta(\vec{q} - \vec{q}_c)} + \underset{Sideband\,-1}{\mu FT\big\{A(\vec{r})e^{-i\phi(\vec{r})}\big\}\otimes\delta(\vec{q} + \vec{q}_c)}$$

The centerband contains the information of the conventional TEM imaging, and the two sidebands represents the complex diffraction pattern and its complex conjugate. By centering one of the sideband (for example sideband +1), filtering the centerband information, and performing an inverse Fourier transformation of this sideband, the reconstructed image will be:

$$img_{rec}(\vec{r}) = \mu\, A(\vec{r})e^{i\phi(\vec{r})},$$

Where the amplitude $A(\vec{r})$ and phase $\phi(\vec{r})$ are the real and imaginary part of the reconstructed image. Off-axis holography has two key parameters: the fringe spacing s and hologram width w_{hol}. The s and w_{hol} is defined by the geometric position of the biprism in the path of the beam:

$$s = \frac{a + b}{2k_0 a\gamma},$$

and

$$w_{hol} = 2b\gamma - 2r_f\frac{a + b}{a},$$

where k_0 is the nominal wavenumber. $\gamma = \gamma_0 U_f$ is the deflection angle that is proportional to the biprism voltage U_f. r_f is the radius of the biprism filament. a is the distance between the biprism and the virtual source, and b is the distance between the filament and the first image plane. Because of the nature of the hologram, the area that is suitable for the off-axis electron holography needs to be adjacent to the vacuum where the reference wave passes. Hence the w_{hol} needs to be in the same scale of the feature that is characterized in the holography experiment. It is clear that the w_{hol} can be directly increased by increasing the biprism voltage U_f, but in the same time s will also decrease, which eventually will become less than the resolution of the CCD and lose contrast because of the coherence loss. Hence special lens condition is needed to lower the first image plane and higher the virtual electron source, so that both w_{hol} and s can be improved.

With the objective lens turned on, one can achieve higher magnification of the sample, however the whol of the hologram will only be in the range of tens of nanometers. In order to achieve a maximum whol for the solar cell application, we set the current of the objective lens to zero and turn on the objective mini-lens (Holo-LB mode in ARM300F). By using this condition, we can adjust the w_{hol} from 510 nm to 764 nm and s from 2nm to 1.26 nm by tuning the Bias voltage on the biprism from 125 V to 170 V. Using such condition, the focus of the sample is adjusted by the objective mini-lens (T-OM). The lack of magnification in this mode can be compensated by the 4k by 4k resolution Gatan Oneview CCD camera. Figure 8 illustrates the process of extracting phase information from a hologram of a BFO/TSO multi-domain thin film sample.

One of the important application of off-axis holography is to quantitatively measure the electrostatic potential distribution of a specimen. The electrostatic potential is constituted by several sources: potential from the atoms, local compositional variations, change of bonds and strain of the lattice, doping potentials, contact potentials, defects, Schottky effect, and external biasing. The contribution of the atioms in a solid material is called mean inner potential (V_{MIP}). The origin of the V_{MIP} is the superposition of atomic potentials and charge distribution caused by the bonds. The V_{MIP} can be expressed as the following approximation:[86]

$$V_{(\vec{r})} = \frac{Ze^2}{4\pi\varepsilon_0 \vec{r}} exp|-b\vec{r}|,$$

where Z is the atomic number, e is the electron charge, ε_0 is the dielectric constant in the vacuum, r is the distance from the nucleus, and $exp|-br|$ is the screening of the nucleus by the electrons. The V_{MIP} for silicon is roughly 12 V. [87]

In the absence of strong effects of dynamical electron diffraction, and the phase object approximation (POA) holds, the phase component is directly related to the electrostatic potential:

$$V_{(\vec{r})} = \frac{\phi(\vec{r})}{\sigma t},$$

where t is the thickness of the sample that is related to the inelastic mean free path of the sample. And σ is an interaction constant that is 0.00729/Vnm for electrons accelerated to 200 keV. In order to measure the weaker potential change, for example, the built-in potentials of a p-n junction, the sample must be sufficiently thick to distinguish the built-in potential from the inner potential of the material. In this case, the object must be oriented in such way that the dynamic scattering conditions are eliminated so that the POA still holds.[88, 89]

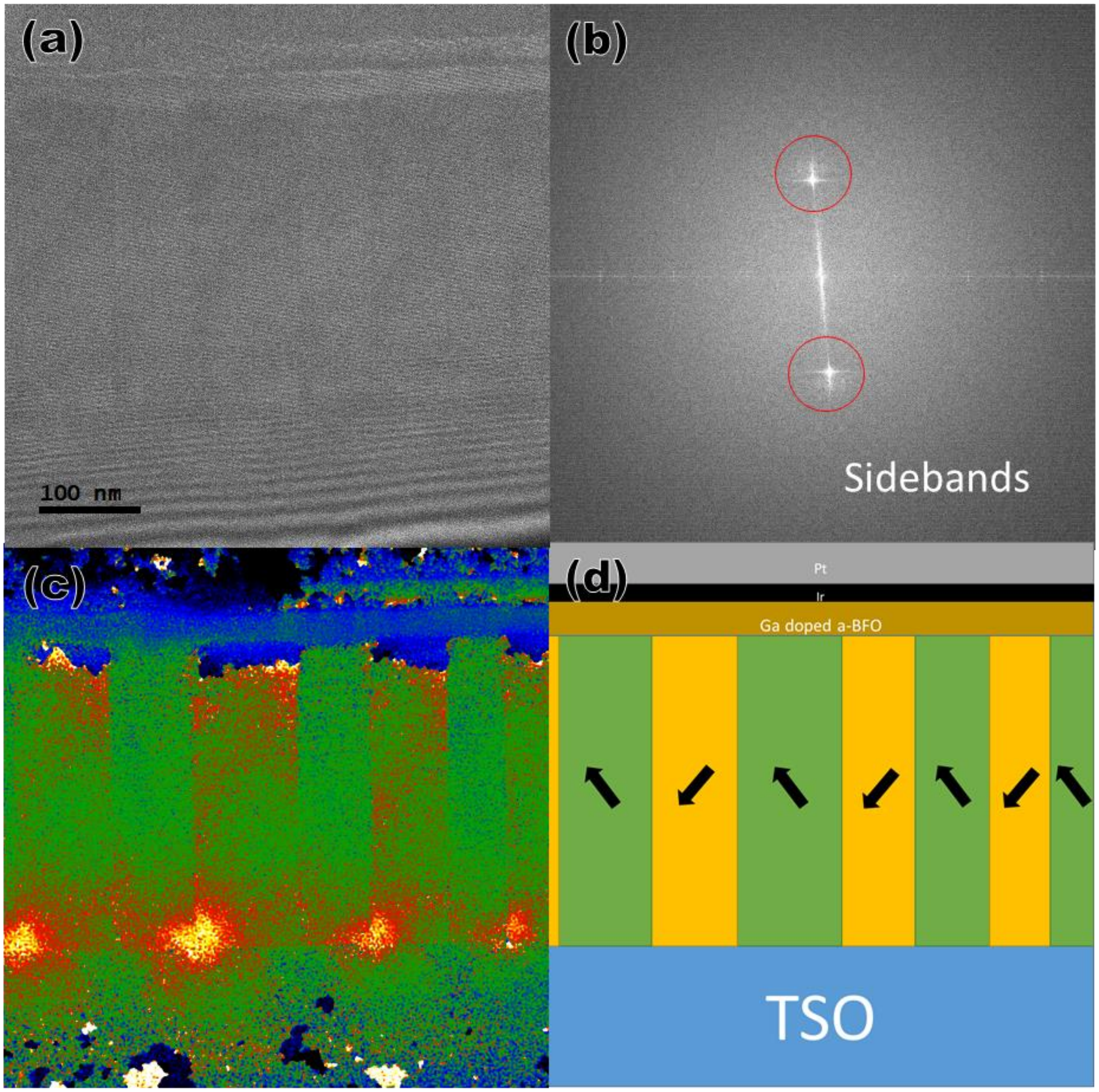

Figure 8 Extraction of phase information from holography. (a) is a holography of a BFO/TSO film with multi 109 domains. (b) is the FFT of the holography. (c) is the phase information after doing i-FFT of one of the side bands in (b). (d) is the schematic of the structure in (a).

2.4 Combining SPM and Raman spectroscopy

The properties of photovoltaic materials depend sensitively on microstructure and composition. However, few methods of analysis allow direct correlation between microscopic details while simultaneously acquiring spatially resolved chemical data. The recent development of instruments combining scanning probe microscopy with chemically sensitive spectroscopies such as Raman provides a novel way to access such information. We have developed methods for coupled scanning probe measurements, such as atomic force microscopy (AFM), conductive AFM, Kelvin probe microscopy, photocurrent mapping etc., for structural and electronic property measurements with simultaneous spatially-resolved Raman mapping to capture chemical information.

Scanning probe technology has matured considerably over the last few years and offers many mechanisms for analyzing the properties of surfaces. For photovoltaic materials, it is possible to map a localized photocurrent under illumination, allowing surface or cross-sectional structures to be correlated with local photocurrent generation. Such measurements give insight into structure versus electronic properties, but cannot give any information about local chemistry, which has important effects on efficiency. The combination of scanning probe with Raman spectroscopy would allow chemistry and property measurements to be correlated at the same scale.

Raman spectroscopy is a powerful method to study small structural and compositional differences of material under ambient condition. Particularly, it is very sensitive to variation of the lattice parameter and crystal symmetry caused by doping and/or defects.

In Raman spectroscopy, a high intensity monochromatic light source, typically a laser, is used to illuminate a material, and the scattered photons that interact inelastically with the phonons of the material are detected. The energy shift from the incident wavelength carries information on the low-frequency phonon modes in a system[90]. For crystalline materials, this energy shift is very sensitive to bonding, and so gives direct chemical information that can be used to determine crystal structure and compositions as well as small changes in the crystal lattice due to phase transitions, impurities, doping, or strain.

Using high-precision piezo scanners, a sample can be scanned in raster fashion to produce a spectral map of the surface. If such a scanning system is coupled with an AFM, simultaneous surface, electronic, optoelectronic, and spectroscopic measurements can be gathered.

Scanning probe microscopies are generally capable of sub-nanometer resolutions. However, the spatial resolution of optical spectroscopy is generally diffraction limited, on the order of the wavelength of visible light. While the laser illumination itself is helpful, allowing nanoscale photocurrent measurements under the laser, spatial resolution is on the order of a few hundred nanometers. In some cases, the resolution can be improved using plasmon resonances in metal nanoparticles, as in surface-enhanced Raman (SERS), or in combination with an SPM, spatial resolution on the order of ~30 nm have been achieved using tip-enhanced Raman spectroscopy (TERS). Coupled with correlated SPM measurements, this allows chemistry (bonding) and microstructure to be mapped at comparable length scales.

2.5 In-situ TEM characterization on solar cells

There has been interest in real time observation of physics phenomena under microscopic scale since the development of electron microscopy. because these in-situ experiments usually provide information that is directly related to the true nature of a physics event. In the transmission electron microscope, such phenomenon can be examined on the scale of atomic level. Over the years, many in-situ experimental setup has been developed to allow variables, such as gas environment, temperature, electrical biasing, and mechanical force, to be introduced and controlled in real time. Most in-situ specimen holders are built with singular functionality. However, the demand to push to incorporate multiple functions into a single holder has grown recently, for that most events are affected by multiple variables. It is also worth noticing that most of the conventionally available holders only have single-tilt capability, meaning that the ability to achieve high resolution imaging on these holders are limited.

There are several approaches for the in-situ experiment that involves electrical measurement. The easiest and most common way is to deposit electrodes on the samples and wire them to the electrical feeds before putting the specimen holder into the TEM. This enables capacity typed of electrical field input and is suitable for experiments that needs uniform electrical field. However, as they are usually being deposited by FIB or sputtering, these electrodes usually cover a large area that loses the ability to control local electrical biasing/measurement. However, as the electrical measurement component consists only a few wires, other input such as optical illumination can be easily integrated on to the holder and enable multi-functionality[88]. Another method is to perform the biasing/measurement using a probe that can be manipulated to make contact with a specific point on the sample. Many commercially available holders use this concept, including Hummingbird Nano-Manipulator Holder[91], Hysitron PI 95 TEM PicoIndenter[92], and NanoFactory holder[93]. As the manipulation system takes a significant amount of the space, these holders usually only have singular functionality and single-tilt feature. The third approach is to use chip-based Microelectromechanical systems (MEMS). These designs miniaturize the electrical components and integrate them on to a single-use silicon based chip that has an electron transparent SiN window for observation. The advantages about these design is that different combinations of the functionalities can be customized for the experiments as long as they are compatible with the electrical contact layout of the holder. For example, Hummingbird Scientific provides more than 60 varieties of MEMS chips to support a wide range of applications, such as combination of electrochemistry or multiple contacts biasing. However, such systems are limited by the type of the samples that can be used. It is very difficult to mount a thin film sample for that the SiN window is preferable for the loading of powder and 2-D materials. Additionally, while the MEMS chips provide compact multifunctionality, it limits the ability for dynamic methods such as manipulation of probes and illumination. As a result, these MEMS holders are not suitable for thin film characterizations.

For in-situ characterization of solar cell devices in TEM, one needs a in-situ holder that allows the combination of photovoltaic measurement and high resolution imaging. This means that the specimen holder needs to have a nano-manipulation system for probing, an optical system for photo illumination and spectroscopy, and a double-tilt system for the optimal resolution. In addition, the holder should be compatible with the Φ3 TEM grid/half grid for the conventional hand polished samples and FIB samples. The combination of probing and optical input will enable not only photovoltaic experiments but also in-situ characterization of photocatalysis, Cathodoluminescence of semiconductors, and in-situ holography measurement for LED, Solar cells and other light sensitive measurements. For these reasons, our design of customized holder uses a manipulation system instead of a MEMS system to realize electrical measurements. The first challenges for such approach is to fit a complete manipulation component, a fiber optic component, and a double tilting component into a single specimen rod, while the front part can still fit in the polepiece gap of the TEM. The actual polepiece geometry is proprietary information, but generally, the point-to-point resolution decreases as the polepiece gap increases. For ultra-high-resolution polepiece, the gap is too small for most in-situ holder to fit in. However, with the introduction of aberration corrector, ultra-high resolution such as 0.1nm point-to-point in TEM and 82pm in STEM HAADF can be achieved with even the wider analytical polepiece in JEOL JEM-ARM300F Grand ARM TEM. Given such advantage on the spacious polepiece gap, we can integrate the three components that we need into a single holder.

The second challenge is the insulation between the electrical component and the TEM rod. In in-situ TEM experiments, the sample must be float with respect to rod because the potential between the rod and the goniometer is used to determine whether the rod is fully inserted in place. In the same time, the sample stage must be conductive so that the localized charging effect from the electron beam is minimized. Conventional in-situ holders usually use a metal cladded insulator, such as a silver printed circuit ceramic board for NanoFactory holder or a metal cladded ceramic board for Hummingbird nano-manipulator holder. And these boards are clamped by an insulation fixture such as PEEK or epoxy. As for the electrical connection, NanoFactory soldered the wires on the circuit board while Hummingbird use six metal screws as both electrical contacts and mechanical fasteners. The NanoFactory design has a lower resistivity because of the direct soldering, however the electron beam induced current (EBIC) onto the entire board will be collected and thus the noise level is high. In the Hummingbird design the noise from the EBIC is minimized by connect the sample to the back plate and drain the front plate, however the contact resistance is too high for low signal measurements. In our design, we need to make sure that the sample is well insulated with respect to the holder while still maintain double tilt function and high sensitivity.

The third challenge is the vacuum sealing of the three components. For JEOL microscopes, the column pressure is usually less that 2*10^-5 Pa for best performance. Any leak during the in-situ experiment can cause the gun valve to be shut down to protect the gun chamber. In the NanoFacoty holder, they used a special vibrational mode for the coarse motion thus the holder is sealed with no moving part inside the holder. For the Hummingbird holder a bellow is used to allow the manipulation component to move in x, y and z direction while still maintains the sealing against the environment. For the NanoFactory holder, although the sealing mechanism is straight forward, the special coarse motion is somewhat unpredictable and the contact resistance between the tip holder and the piezo tube is large. For the Hummingbird holder, the bellow is robust enough to seal the holder, however the high spring constant will cause the tip to drift after the tip is displaced by the piezo tube, and the tip range of motion is limited too. In our design, we need to make sure that the three components are well sealed and the holder provides enough space for the manipulation system to move freely.

Before this, we have used a customized Nanofactory single tilt holder to do the probing and electrical measurement. Figure 9c shows the design of the stick-slip motion. The cylinder labeled 3 is the piezo tube; The part 3a is the ceramic ball mounted on the piezo tube; part 4 is the probe holder and 4’ are six fingers that grabs on the ceramic ball. By mounting a pair of LEDs on the sample cartridge of the holder, we have done some preliminary data showing the capability of doing photovoltaic measurement(Figure 9b). However, the current Nanofactory holder has a few limitations: First, the tilting mechanism is not available because the sample cartridge is a cladded circuit board. Without the double tilt function, the holder is unable to do high resolution TEM for the zone axis can’t be adjusted; The mounting of the sample is also not designed for the Φ3 TEM grid because it only has a metal tubing for inserting a probe. We must mount a copper rod onto the Φ3 grid in order to use the holder; last but not the least, the two LEDs are not strong enough for the illumination on the sample, yet it generate localized heat to cause serious thermal drifting because the sample cartridge is made of a ceramic circuit board; The Nanofactory used a vibrational stick-slip motion for the probe to move in coarse motion mode, and despite the idea of enabling both coarse and fine motion modes using the same component, the friction between the probe holder and the piezo motor must be precisely controlled to ensure a stable motion. This requires that the six fingers on the probe holder that grab on the conductively coated ceramic ball, which is mounted on the piezo motor, being bent in a way that each finger has the exact amount of force that is applied to the ceramic ball. Failure of doing that will result in the probe moving in unpredictable direction, being affected by the gravity, or not moving at all. Un fortunately, the fingers are easily bent, damaged, and even broken, during the loading and unloading of the probe because one must take the entire probe holder assembly on and off the ceramic ball to exchange probes. As the Nanofactory went out of business a few years ago, there is no more supply for not only the probe holder, but the entire setting for the in-situ experiment. And since the finger on the probe holder is only .006” in diameter and require special cold work, we need to develop a holder with not the same functionality but more. And that is the origin of this project. The schematic of our approach to develop a holder with double-tilting, probing and illumination is shown in Figure 10. In this design, the electron beam is able to project a high resolution imaging for that the sample zone axis can be aligned by the double-tilting stage; a probe can approach to the area of interest and apply a bias; the fiber optic can illuminate the sample so that the photovoltaic measurement can be performed. Such design gives a unique combination of methods to characterize nanoscale defects such as small phase segregation inside the solar cell and the grain boundaries for polycrystalline thin films.

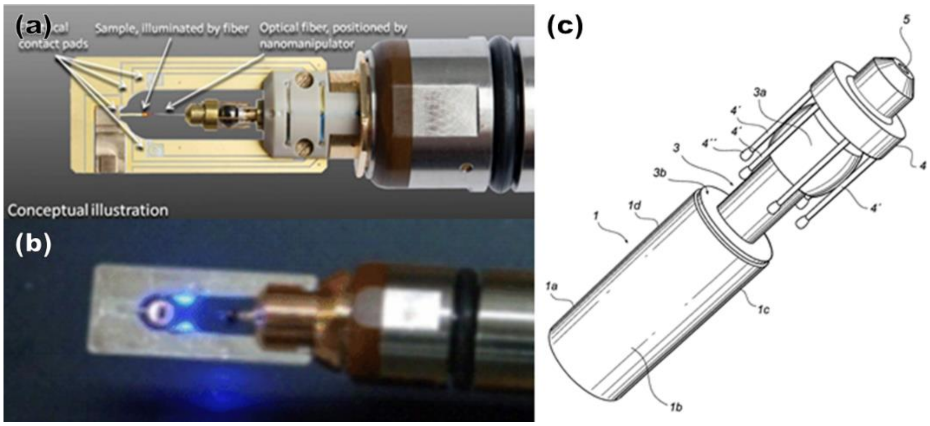

Figure 9 Nanofactory holder design (a) is a conceptual illustration of the Nanofactory single tilt holder. (b) is the modified Nanofactory single tilt holder with integrated LEDs and a standard Φ3 TEM grid mounted on the sample cartridge. (c) is an illustration of the detailed design for the stick-slip motion[94].

In the new design, we added a double tilt function to the sample stage so that the HRTEM and atomic resolution STEM can be done on the thin film samples; we also replaced the stick-slip motion with a “wobble stick” component where the coarse motion is controlled by the linear stage that is mounted on the back of the holder; last but not the least, we replaced the LEDs with a focusable Φ=1mm fiber optics so that the fiber optics can be coupled with lasers of various wavelength and energy depending on the experiment. However, by introducing the new mechanism, there is now three components: double tilt stage, wobble stick, and fiber optics, that need to be individually sealed while still maintain free motion. This has been proven to be a huge challenge in the past 3 years of development. Thus, we have chosen to break the holder into two: one is the double tilt holder with the fiber optics, and the other is the double tilt holder with the STM probing mechanism. So far, we have developed and tested the functionality of both holders. Using the optical holder, we can both do the Cathodoluminescence(CL) spectroscopy measurement as well as electron holography with illumination; For the STM holder we can perform STM mapping, conductivity measurement and indentation. Both holder demonstrate excellent sealing and stability. The next step will be combining the two holders into one.

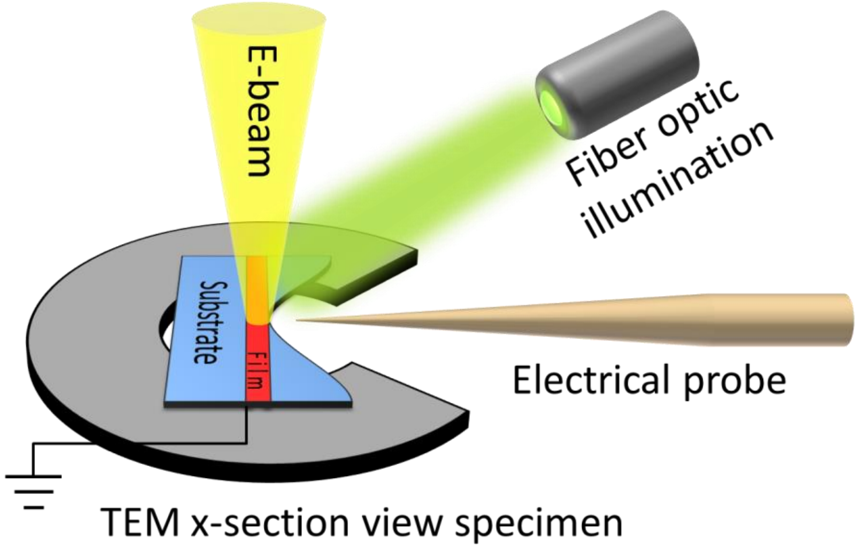

Figure 10 A schematic showing the study of electrical/optical properties of a cross-sectional TEM specimen using an in situ electrical/optical holder.

Chapter 3

Fabrication of high performance CZTSe solar cell devices

3.1 Precursor Film synthesized by Liquid-Phase Pulsed Laser Ablation (LP-PLA) and Electrophoretic Deposition (EPD)

The pulsed laser ablation at the solid-liquid interface was developed in 1987 where metastable iron oxide phases were synthesized by ablating a Fe target in water by a pulsed laser[95]. This method is known as Liquid-Phase Pulsed Laser Ablation (LP-PLA). The laser that we use here is a high-energy femtosecond pulsed laser with 1040 nm wavelength, 600 fs pulse duration, 10 μJ pulse energy, and 500 kHz pulse repetition rate. The laser beam is directed via an automated mirror scanner, and focused through a 170 mm focal lens on the surface of an alloy target submerged at approximately 5 mm beneath acetone. During the LP-PLA, a high-density plasma plume generates from the target when a laser pulse irradiates the interface between the solid target and the confining liquid through the liquid. The laser induced plasma will then be quenched by the liquid medium and forms nanoparticles (NPs). This process of laser interaction with the target is similar for both laser ablation in a vacuum, such as pulsed laser deposition (PLD), and ablation at the solid-liquid interface. Both processes produce plasma that enables high efficient electron-ion recombination. In the first case the plasma expands freely into the vacuum, while in the second case it is confined by liquid. Such environment enables the formation of novel and stable material by creating a localized high pressure and temperature for the plasma. Figure 11 shows a schematic of formation of Cu-Zn-Sn colloid by LP-PLA and TEM images of the precursor CZT nanoparticles.

During the EPD Process, the charged CZT nanoparticles are migrated toward the electrode (substrate) under the applied electric field. The kinetics of the EPD process is first explained by Hamaker[96]:

$$w = \int_{t_1}^{t_2} \mu \cdot E \cdot A \cdot C \cdot dt$$

Where the deposit yield (w) is related to the electric field strength (E), the electrophoretic mobility (μ), the surface area of the electrode (A), and the particle mass concentration in the suspension (C).

This equation is improved that the deposition weight(w), the weight of charged particles deposited per unit area of electrode in the initial period, is described by the following equation[97, 98]:

$$w = \frac{2}{3} C \cdot \varepsilon_0 \cdot \varepsilon_r \cdot \zeta \cdot \left(\frac{1}{\eta}\right) \cdot \left(\frac{E}{L}\right) \cdot t$$

Where C is the concentration of the particle, ε_0 is the permittivity of vacuum, ε_r is the relative permittivity of the solvent, ζ is the zeta potential of the particles, η is the viscosity of the solvent, E is the applied field, E is the distance between the electrodes, and t is the deposition time. The above equation is called Hamaker's law. For a fixed particle-solvent system, the factor that can be adjusted for optimum condition would be the electric field E/L and time t.

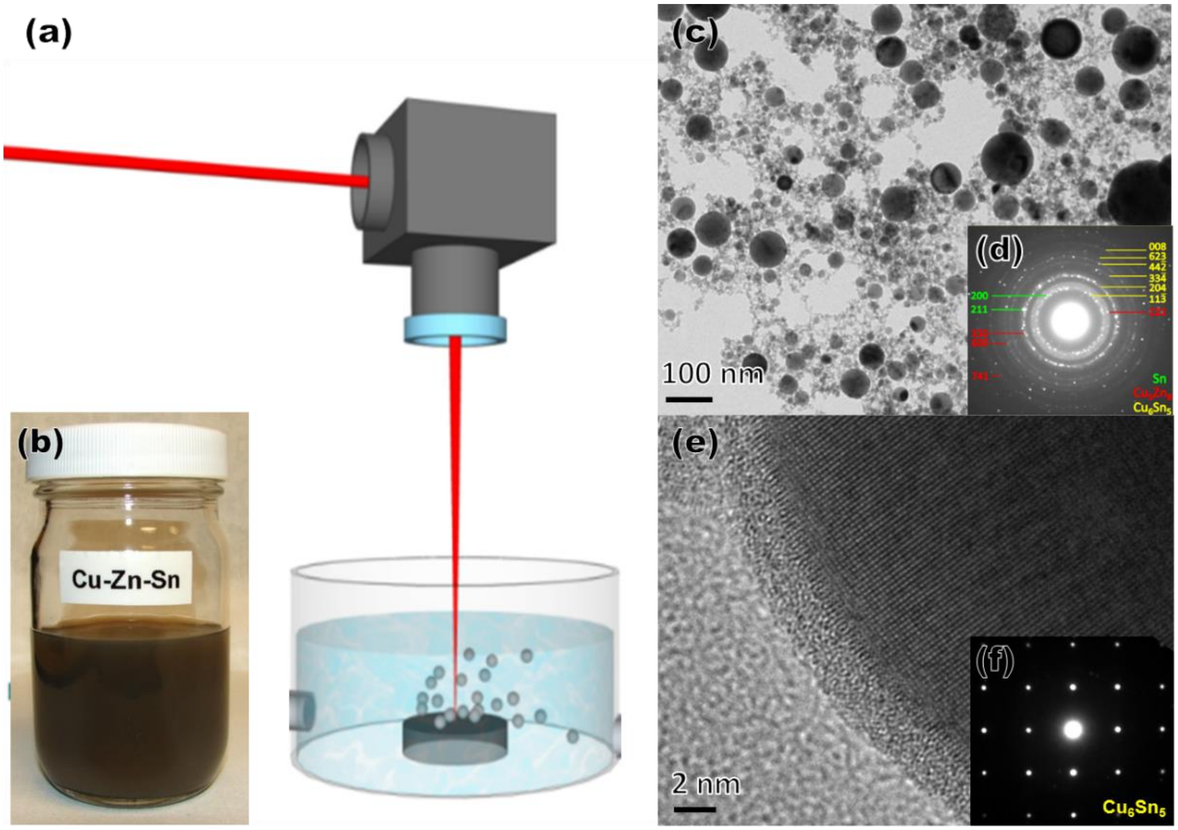

Figure 11 Cu-Zn-Sn colloid precursor (a) A schematic of formation of Cu-Zn-Sn colloid by LP-PLA. (b) A photo of the as-ablated Colloid. (c) A TEM imaging of the precursor nanoparticles and (d) its SAED ring pattern. (e) A HRTEM imaging of a Cu_6Sn_5 nanoparticle and (f) its SAED pattern.

For the best result, the applied electric field at the surface of the substrate should overcome the repulsive forces between the nanoparticles so that the deposition process can occur; The nanoparticles should also have enough kinetic energy to effectively migrate to the electrode from the solvent; more importantly, the deposition should take place at the negative electrode (cathodic EPD) to prevent oxidation at the anode. However, the Zeta potential for CZT particle is negative, thus needs to be reversed to enable cathodic EPD. In the previous study of CIGS films, we found that a low concentration of the nitrate salts with trivalent cations such as In^{3+} or Ga^{3+} can effectively reverse the Zeta potential. Such alteration of surface charge is caused by the physical adsorption of the high valence heavy cations on the surface of the nanoparticle. This process has been proved to be also effective on switching the Zeta potential of the CZT colloid to enable the cathodic EPD. In the EPD process for the CZT particles, an electric field of 150 V/cm is applied on the 20 mm×30 mm Mo and Pt electrodes at 10 mm apart. The deposition rate is around 1.5 μm/min. 10 μM of $In(NO_3)_3$ is added to the colloid before deposition to reverse the ζ. Figure 12 shows the schematic of the EPD process and the SEM imaging of the as-grown precursor film.

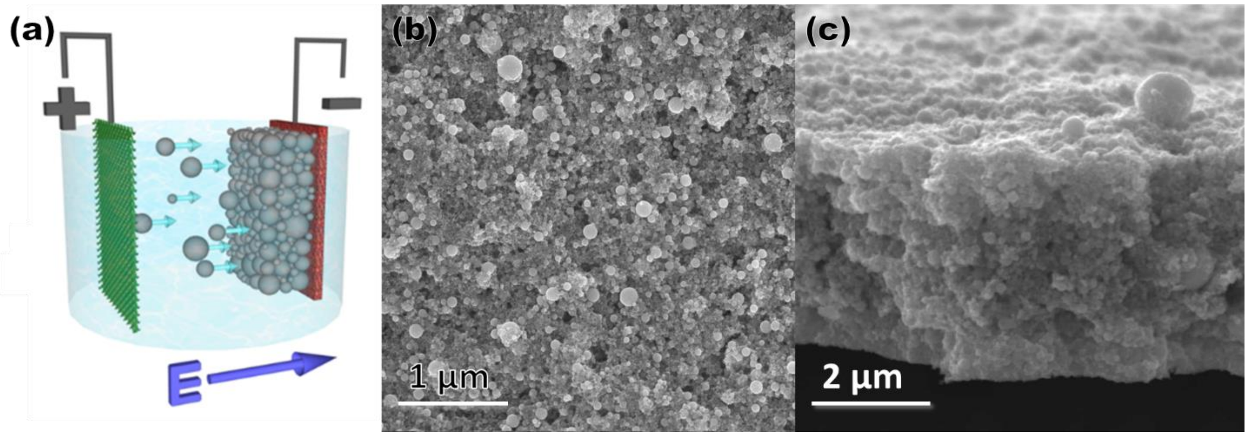

Figure 12 Precursor film fabricated using EPD(a) A schematic of forming the precursor film by EPD (b) and (c) are SEM images of a top view and gross-sectional view of a precursor film.

After the EPD process, the precursor film consists of densely packed nanoparticles with diverse sizes (Fig. 1a). This structure allows the Se vapor to penetrate the precursor film through the interstitials of the nanoparticles stack, which contributes to the fast and uniform annealing process. However, it can also cause problems such as inhomogeneity and pin holes. The cause of inhomogeneity can be linked to the CZT alloy target composition and the selenization process of CZT nanoparticles. The final composition will be different from precursor depending on the synthesis method and other factors. For example, the target used for LP-PLA consists of Cu_5Zn_8, Cu_6Sn_5 and Sn to achieve the Cu/(Zn+Sn) ratio of 0.9 and Zn/Sn ratio of 1.2 at a macroscopic level, which most high efficiency CZTS cells have in common. The EDS data indicated that the actual Cu/(Zn+Sn) ratio of the target is 0.82 and the Zn/Sn ratio is 1.2. Surface roughness of the alloy target may affect the ablation speed of different metal phases resulting in composition variation of colloidal suspension. SAED ring pattern indicated that these nanoparticles have the same phases as the target (Figure 11c, d). But the SAED pattern of an individual particle shows that it only consists one of the three phases (Figure 11e, f). Hence it is likely for a large precursor particle to create a local composition variation and lead to a non-uniform precursor film. The different deposition speed of each alloy nanoparticle may also contribute to the composition variation with respect the depth of the film. Due to the rapid annealing and the instability of the CZTSe phase, it is difficult for the selenization process to homogenize the film before the formation of secondary phases start to take place. The formation of highly volatile SnSe may also cause the composition to change.

3.2 Forming CZTSe polycrystalline thin film using selenization process

After the precursor film is formed by EPD, they are then placed in a graphite box (Figure 13Figure 2b) along with the Se shots. The graphite box consists of three parts: Top and bottom enclosures, and an intermediate layer. The Se are placed on the intermediate layer while the precursor films are placed on the bottom enclosure. During the selenization process, the graphite box assembly is placed in a sealed quartz furnace tube (Figure 13a). The tube will be vacuumed and purged by argon several times to remove any residue oxygen. 1 atm of argon will be introduced to the tube and the tube will undergo a fast annealing in 540 °C for 10 minutes. This process is called the selenization process. During this process, the Se shots will be vaporized, pass through the intermediate graphite layer and react with the precursor film. The final product will be polycrystalline CZTSe film and a layer of MoSe2 between the CZTSe and the Mo substrate. Figure 13c and d show the cross-sectional SEM imaging of a film before and after selenization. Note that the CZTSe film in Figure 13d has been lift out and the layer beneath the CZTSe grains is MoSe2. Molybdenum (Mo) has been widely used as the back contact for CIGS solar cells. It is stable at high process temperature and doesn’t alloy with Cu and other metals under high temperature, strong bonding with soda lime glass (SLG) supporting substrate and CIGS film, and low-resistance ohmic contact with CIGS[99-106]. However, during the selenization process, an intermediate layer of MoSe2 can be formed between CZTSe and Mo substrate. In CIGS, a thin layer of MoSe2 can be beneficial because of it has low bandgap and is in ohmic contact with CIGS and Mo[106-108]. The best performing cell of 12.6 efficiency has a 85 nm ± 30 nm thick MoSe2 layer[40]. However, for the case of CZTS, the high Se vapor pressure and the instability of CZTS film under high temperature will cause the rapid growth of the MoSe2 layer. At the interface between CZTSe and Mo under the selenization temperature of 540 °C, the decomposition of CZTSe follows the reaction: [109, 110]

$$2Cu_2ZnSnSe_4 \leftrightarrow 2Cu_2Se + 2ZnSe + 2SnSe + 2Se(g)$$

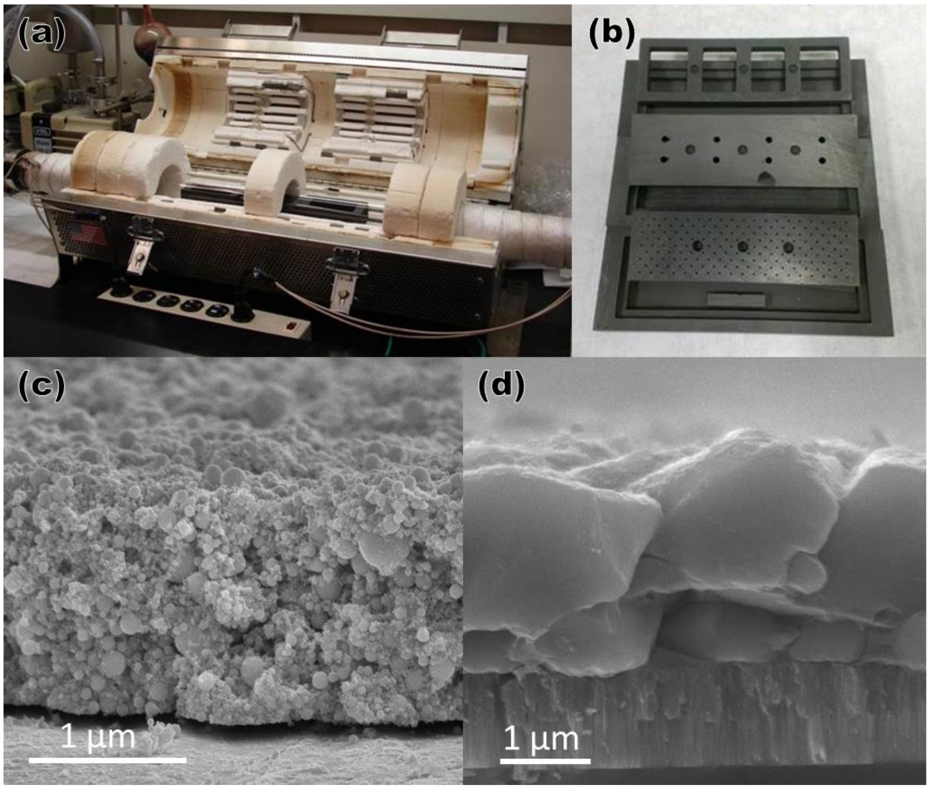

Figure 13 CZTSe film after selenization (a) A furnace with precursor film sealed inside a quartz tube. (b) a graphite box with 3 types of intermediate layers to control the reaction with Se vapor and the film. (c) A cross sectional SEM imaging of a precursor CZT film and (d) a CZTSe film after selenization.

At the CZTSe/Mo interface, Mo reacts with Se to generate MoSe2 according to the following reaction:

$$Mo + 2Se \rightarrow MoSe_2$$

Combining above reactions, we have the reaction that describes the formation of MoSe2 at the CZTSe/Mo interface during annealing/selenization:

$$2Cu_2ZnSnSe_4 + Mo \rightarrow 2Cu_2Se + 2ZnSe + 2SnSe + MoSe_2$$

The free energy change of above reaction is -100 kJ at 550 °C, which indicate that the formation of MoSe2 and the decomposition of CZTSe is thermodynamically favorable at the interface. This explains that for the final product of CZTSe film, there is usually a second layer of finer CZTSe grains between the layer of coarser CZTSe grain and MoSe2. After the decomposition of CZTSe, the volatile SnSe will likely to escape from the film and move the equilibrium to the right. Hence excessive Se and SnSe that are introduced in the environment is expected to suppress the decomposition of CZTSe. However in reality, when we investigate the cross sectional CZTSe samples that are annealed in different Se partial pressure, we found that the excessive Se mostly increased the thickness of the MoSe2 layer instead of stabilizing the CZTSe. As can be seen from the Figure 14, the thickness of the MoSe2 was studied for samples that are selenized with standard amount of Se (1.5 Se pellets per sample), 4 times the amount of Se (6 Se pellets per sample), and 8 times the amount of Se (12 Se pellets per sample). The plot in Figure 14 indicates that the thickness of the MoSe2 in proportional to logarithm of the Se concentration. Such result agrees with that, kinetically, the formation reaction rate of MoSe2 is much faster than that of selenization of CZT precursor film. Given the short annealing time of 10 minutes under 540 °C, the Se source that is required to complete the selenization process is consumed by the reaction of forming the MoSe2. Hence the double layer structure is inevitable regardless of the concentration of Se. The formation of a thick layer of MoSe2 can potentially reduce Voc, Jsc and FF in the CZTSe devices, the poor adhesion of CZTSe/MoSe2 and MoSe2/Mo interfaces also impair the structural stability of the device and thus reduce the efficiencies.

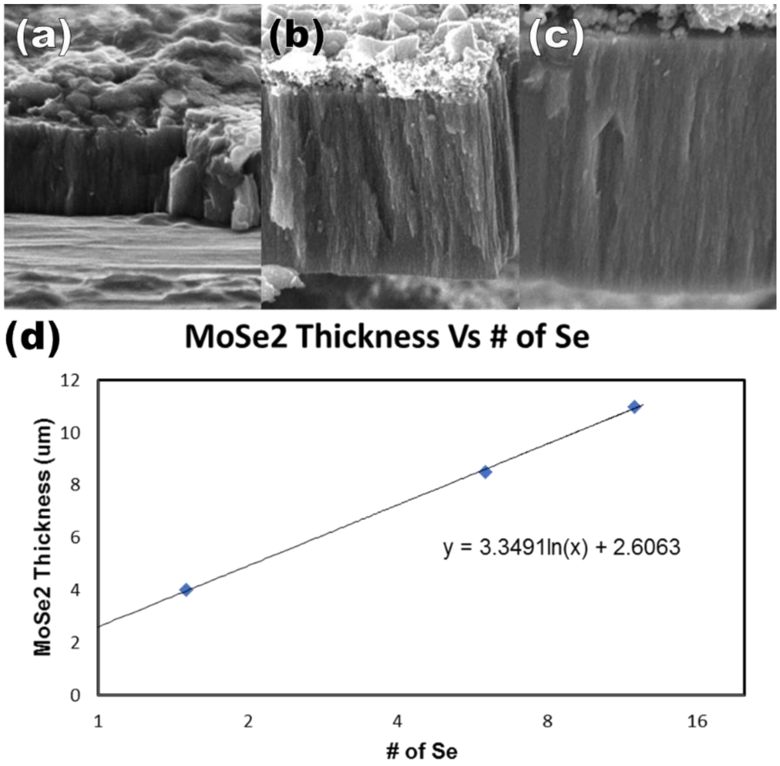

Figure 14 Cross sectional SEM imaging of CZTSe film after selenization with (a) 1.5 Se shots per film, (b) 6 shots per film, and (c) 12 shots per film. (d) is the plot of the MoSe2 thickness versus the Se concentration.

3.3 Non-homogeneity in CZTSe thin film and device characterization

So far, we have achieved a maximum of 4.77% energy conversion efficiency on a CZTSe cell with a total area of 0.085 cm2, and 4.20% on a cell with the area of 0.177 cm2. The first cell comes from a 3mm by 3mm CZTSe cell array and the top electrode is colloidal Ag. The second cell comes from a 3mm by 6mm CZTSe cell array and the top electrode is thermal evaporated Au. The sample of the two cell arrays are indicated in Figure 15. Although the best efficiency found on the two types of cell configuration are close, the high efficiency (>3%) cells are much rarer in the 3mm by 6mm cells. This suggested that the inhomogeneity in the CZTSe cells that we fabricated is quite pronounce. Figure 16 shows the distribution of cell efficiency of a typical 3mm by 3mm cell arrays. The mean efficiency for this cell is 2.15% and the standard deviation is 1.17%. As can be seen from the efficiency mapping in Figure 16b, the variation of the efficiency is not completely random. Instead, the highest efficient cells are found at the bottom left region and the efficiency gradually decreases as the cell is further away from it. And the lowest efficient ones are found at the top right corner, which are the furthest from the best efficient ones. Clearly, the efficiency is related to the local structure variation during the fabrication process where the microstructure in the bottom left corner is different than that in the top right corner.

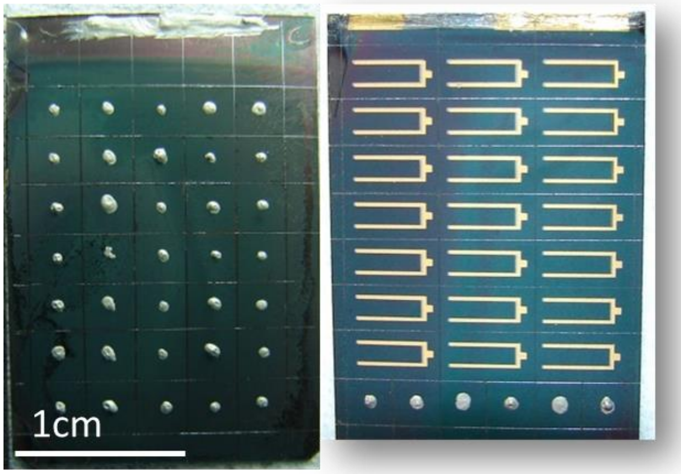

Figure 15 Best performance CZTSe cells: To the left is a CZTSe solar cell array with Ag top electrodes and average cell area of 0.09 cm^2. To the right is a CZTSe solar cell array with thermal evaporated Au electrodes and the average cell area is 0.18 cm^2.

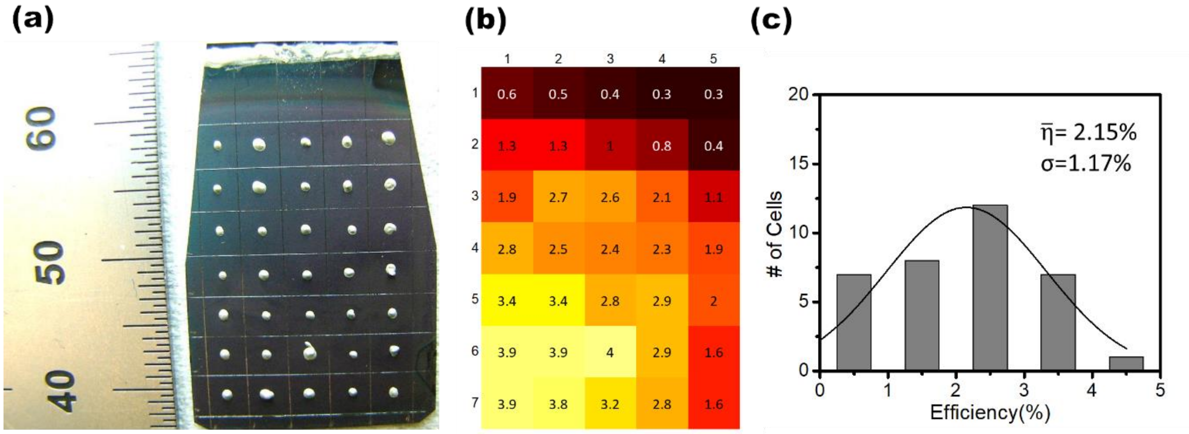

	1	2	3	4	5
1	0.6	0.5	0.4	0.3	0.3
2	1.3	1.3	1	0.8	0.4
3	1.9	2.7	2.6	2.1	1.1
4	2.8	2.5	2.4	2.3	1.9
5	3.4	3.4	2.8	2.9	2
6	3.9	3.9	4	2.9	1.6
7	3.9	3.8	3.2	2.8	1.6

Figure 16 Efficiency distribution within a cell array (a) is a 5 by 7 CZTSe cell array with Mo sheet substrate. (b) is the map of measured efficiencies of the cell array in (a). (c) is the histogram of (b).

Furthermore, as we chose different design of graphite box during the selenization, we found that this variation may be due to the gradient of Se vapor concentration. Figure 13b shows three different design for the intermediate layer of the graphite box. The three pits on each intermediate layer are for holding the Se pellets, and the patterned holes surrounding them are the preferred path for the Se vapor to reach the sample sitting beneath the intermediate layers. The sample in Figure 15 is selenized in the top design in Figure 13b. we noticed that the closer the cell is to the Se source, the higher the efficiency will be. Figure 17 is a sample that has been selenized in the second design of graphite box, where the square holes are replaced by an array of round holes with Φ=1/8”. This time we can see the pattern of the holes on the graphite box being reflected on the sample. And the result shows that the efficiency near these patterns are usually higher than that inside or far from the pattern. The SEM imaging confirms that the region with high efficiencies has much larger grains and less gaps between them. Figure 18 is another sample that is selenized using the third design, where the holes are replaced with an array of smaller sized ones. And the result in consistent with the previous design.

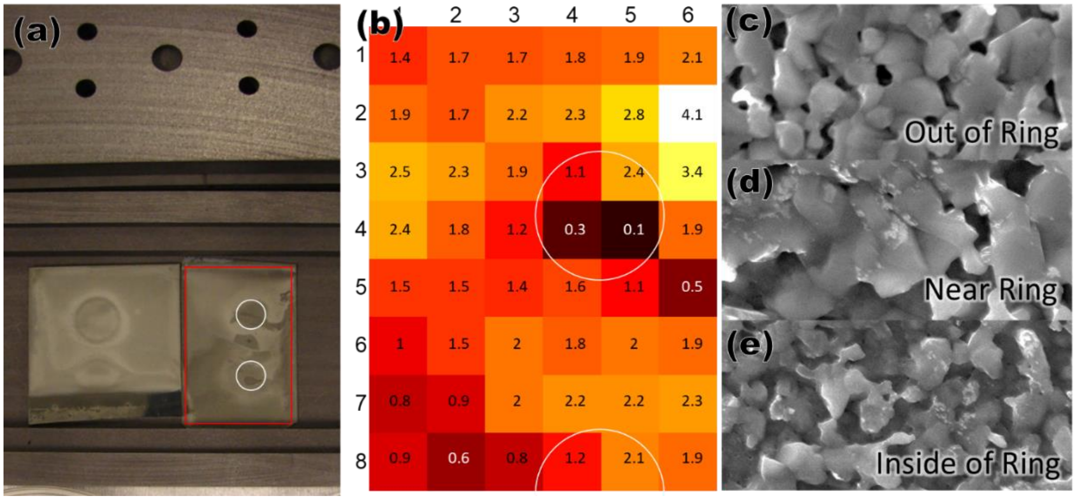

Figure 17 Efficiency influenced by geometry of the graphite box. (a) is two CZTSe films sit inside the graphite box after selenization. (b) is the efficiency mapping of the device made from the right film in (a), which is highlighted in red box. (c), (d), and (e) are top visual SEM imaging of the region out of, near, and inside of the ring pattern marked in white circles in (a) and (b).

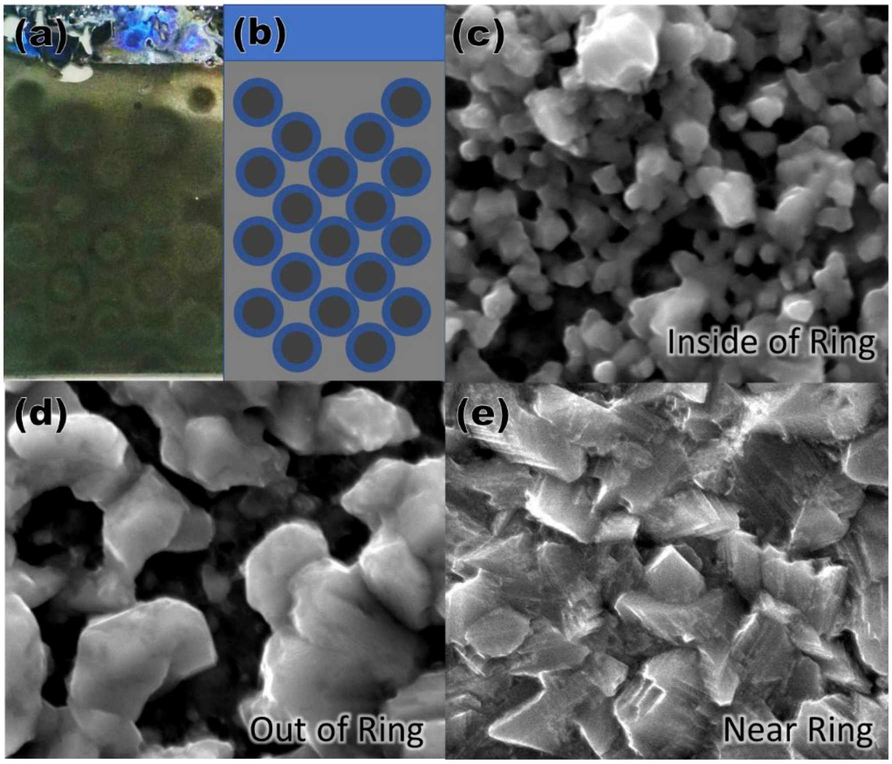

Figure 18 CZTSe grain size influenced by geometry of the graphite box. (a) is a CZTSe film that is selenized using the graphite box design of a different graphite box design. (b) is the schematics of the ring pattern in (a). (c), (d) and (e) are top visual imaging of the region that inside of, out of, and near rings.

During the selenization process, the region that is too close to the source may be affected by the liquid form of the Se vapor in the heating process, when the selenization temperature hasn't fully reached. In this case, the excessive amount of Se liquid/vapor at low temperature can result in a complete selenization but the liquid Se can hinder the process of grain growth as it fills the gap between the grains. This is the reason why directly beneath the hole patterns the grain size is usually small. When the temperature of 540 ℃ is reached, a Se vapor partial pressure gradient is formed where right below the hole patterns the concentration of Se is the most because these holes act as nozzles for the Se vapor to pass. The region right next to them will have higher Se concentrations, and hence improve the selenization process. The region that is far from the Se source will have much lower concentration and thus will undergo an incomplete selenization. As a result, the region that has more complete selenization will have a larger and denser CZTSe grains, and thus will have better efficiency; the region that has less complete selenization will have either smaller grain sizes or more gaps, and will have less efficiency.

To study the origin for such variation of the performance of the CZTSe solar cells fabricated using LP-PLA and EPD, we studied the microstructures and the electrical properties of the CZTSe devices with different efficiencies. Figure 19 shows planner SEM and cross sectional TEM imaging for 2 different efficiencies. Sample 1 has an average grain size of 1μm and an efficiency of 4.77% while sample 2 has an average grain size of 300 nm and an efficiency of 2.20%. According to the J-V curves (Figure 19e), sample 1 and 2 have similar V_{OC} values (0.315V and 0.325V). They also have similar long wavelength "absorption" edges (Figure 19f). Such similar behaviors indicate that the bandgaps of the two samples are close to each other. They also have similar but low values of R_{Sh} (463Ω and 424Ω). Such low shunting resistances are determined by the defective device structure. The quality of the EPD grown precursor film under non-vacuum condition can cause pinholes to form near the back interface during the selenization process, which leads to loose adhesion and creates shunting paths that can result in reduced shunting resistances for both samples. However, unlike V_{OC} and R_{Sh}, the differences of J_{SC} and R_S between the two samples are more pronounced. Sample 1 has a J_{SC} value of 34.7 mA/cm^2 and a R_S value of 41Ω, while for sample 2 these values are 21.0 mA/cm^2 and 118Ω. The EQE data (Figure 19f) also shows an overall reduction of quantum efficiency for sample 2, especially at the long wavelength region. The loss of photocurrent in sample 2, which has a smaller average grain size, can be explained by the effect of horizontal GBs. Generally, the GBs are full of defects and dangling bonds that can be modeled as thin amorphous layers that have a larger bandgap than crystalline CZTSe. The Fermi level is thus pinned near the midgap at GBs and forms a barrier to prevent carriers from traversing GBs.[111] The density of such barriers is higher if the grain size of the polycrystalline CZTSe films is smaller, such as in sample 2. This results in an increased value of serial resistance and a reduction of photo current density, which agrees with our experimental results. Therefore, for the CZTSe system, a device with grain sizes that are too small will have a significant number of GBs spreading across the film (horizontal GB), creating more barriers against the transportation of the carriers. This double-layer property can also be seen in the CIGS device fabricated using the same method. Figure 20 shows the STEM cross-sectional images of CZTSe and CIGS device fabricated by the nanoparticle selenization method. To study the origin of such inhomogeneity on grain size, we first acquired EDS spectra of two CZTSe films with distinct average grain sizes(Figure 21). The result shows that the O concentration is significantly higher for the film having smaller grain compared to the one with larger grains. The excessive oxygen is likely to be introduced before or during the selenization process. It will be difficult for CZTSe to grow if the precursor nanoparticle is partially oxidized since the O is much more electronegative than Se. In Figure 22, we found that the oxygen Kα peak (0.525 keV) is observed at the edge of a CZT precursor nanoparticle. In Figure 23 we found that for the same batch of precursors, the thickness of oxide layers is similar regardless of particle sizes. This means that for smaller particles the ratio of oxide shell is higher than larger particles. During the EPD process, smaller particles usually has higher mobility and are more likely to be found at the bottom of the film, which result in a higher oxygen concentration near the substrate. During the selenization process the formation of MoSe2 can also consume a large amount of Se so that the Se vapor pressure is significantly lower at the interface than the surface. As a result, the precursor film will not fully transform into large CZTSe near the interface. Instead, they will form a layer of fine grains (Figure 24), increase Rs and reduce the cell efficiency. Since the LP-PLA uses acetone as solvent, the oxygen must have been introduced when the precursor film is transferred to the furnace. A better way to solve this problem is to place the precursor film in an inert environment during the transfer such as a glovebox. By reducing the exposure to air, the precursor nanoparticles will have much thinner oxide layer and will be much easier for Se vapor to selenize.

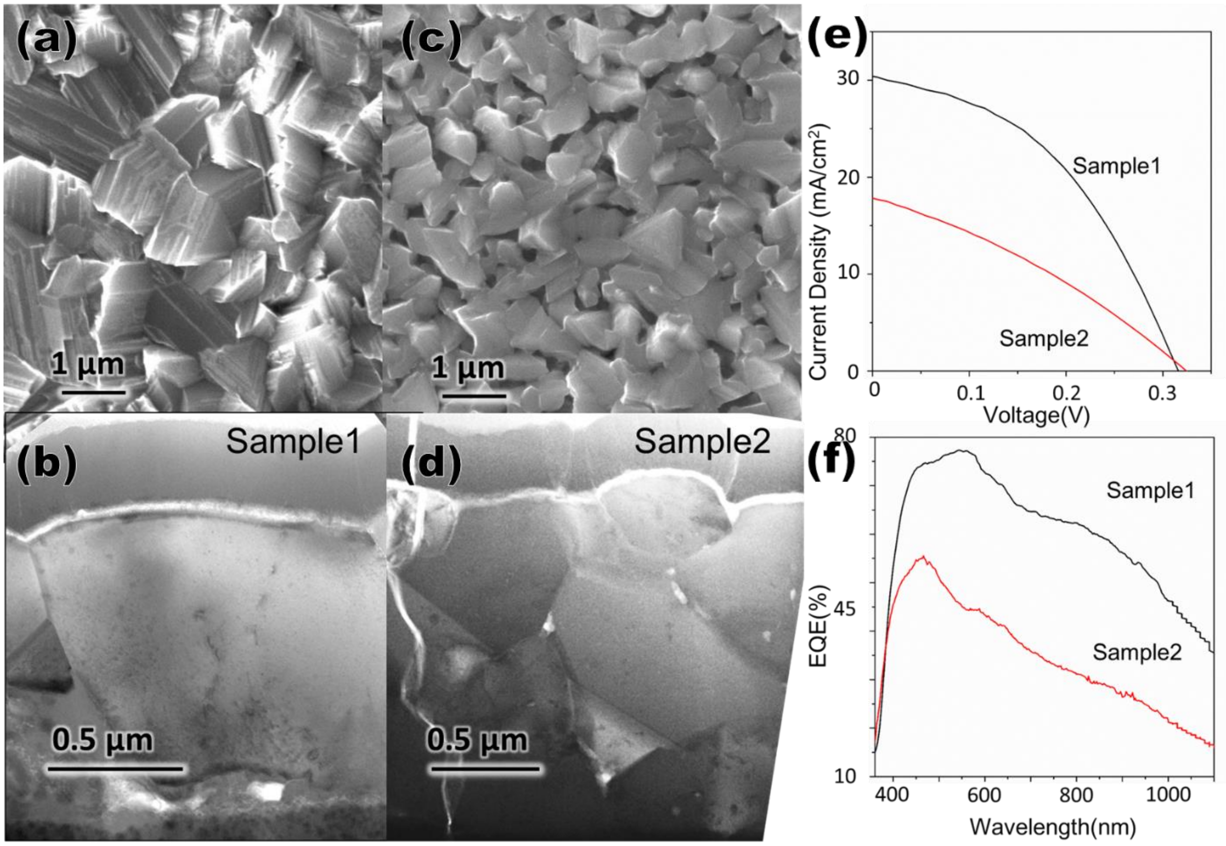

Figure 19 Efficiency influenced by grain size (a)(c) Planer SEM images and (b)(d) cross-sectional STEM ABF images of CZTSe sample 1 and 2, respectively, as well as (e) their J-V curves and (f) EQE spectra.

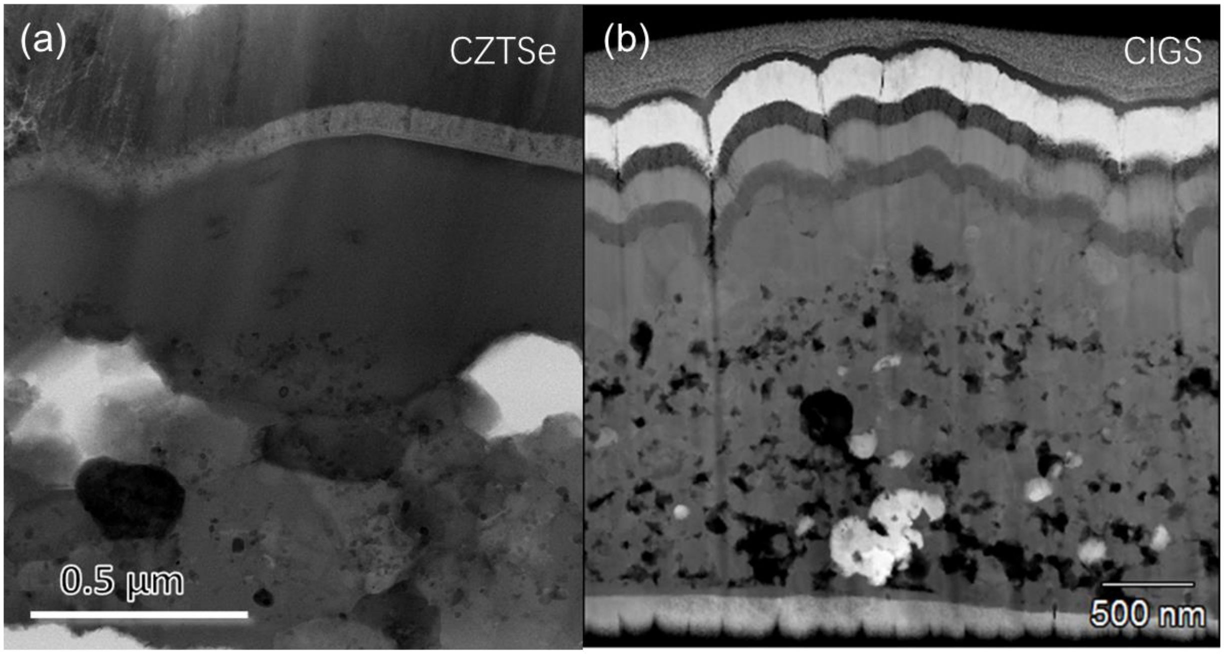

Figure 20 Double layer structures in CZTSe and CIGS. (a) and (b) are the TEM cross-sectional imaging of CZTSe and CIGS devices fabricated using the LP-PLA and EPD process.

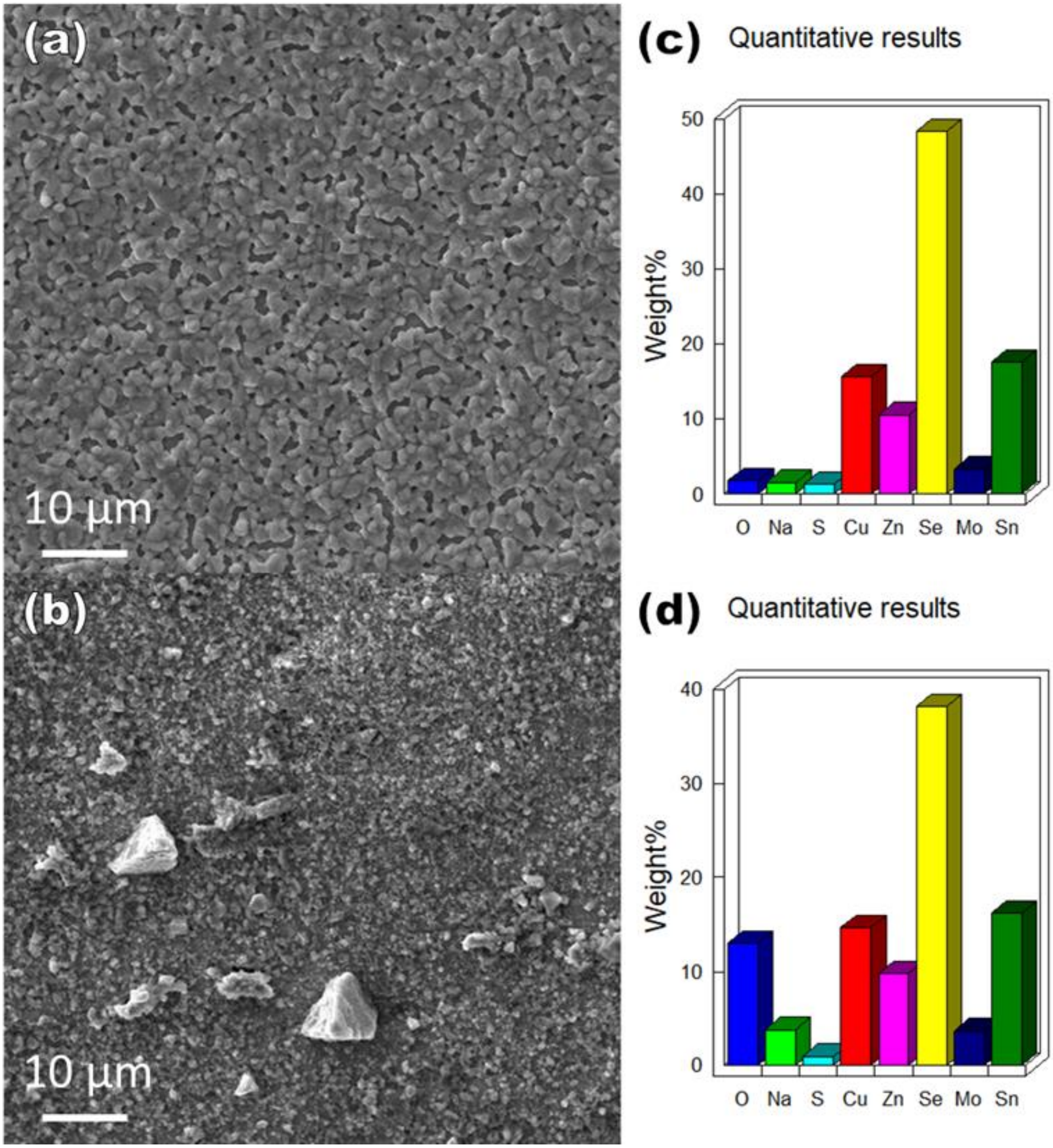

Figure 21 SEM-EDS spectroscopy of CZTSe with different average grain sizes. (a) and (b) are SEM SEI images of CZTSe with large and small average grain sizes. (c) and (d) are EDS elemental weight distribution of different elements.

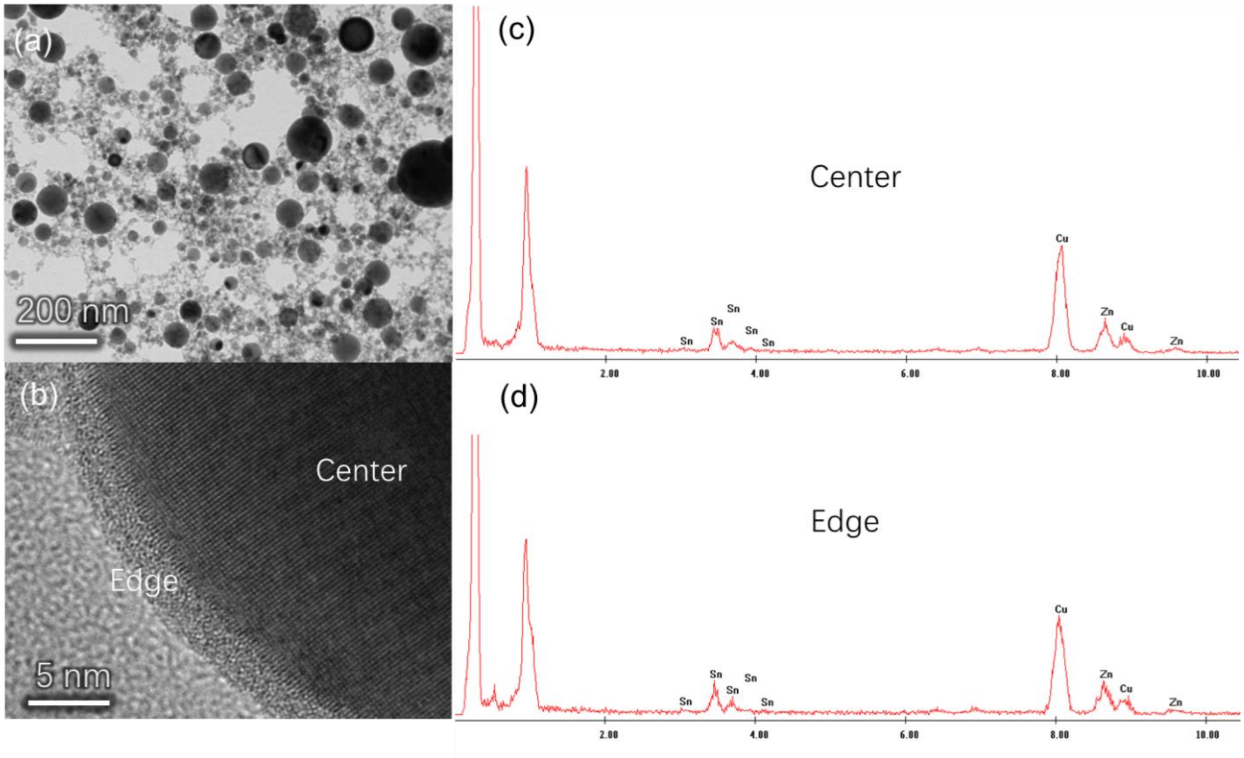

Figure 22 EDS point spectra on a precursor nanoparticle. (a) and (b) are TEM BF imaging of the precursor nanoparticles. (c) and (d) are EDS spectra of the center and edge region of the particle in (b)

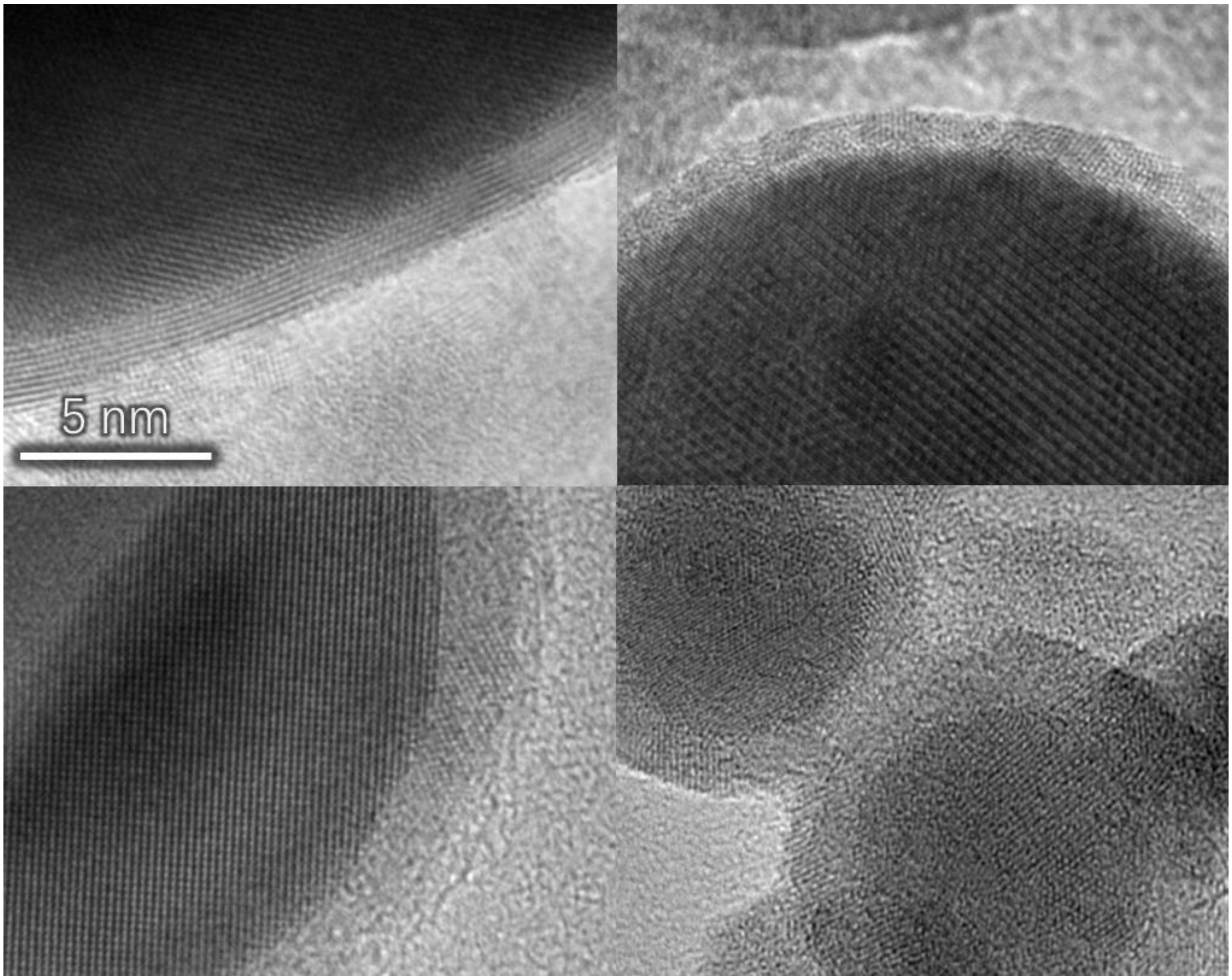

Figure 23 TEM BF images of partially oxidized precursor nanoparticles of different sizes.

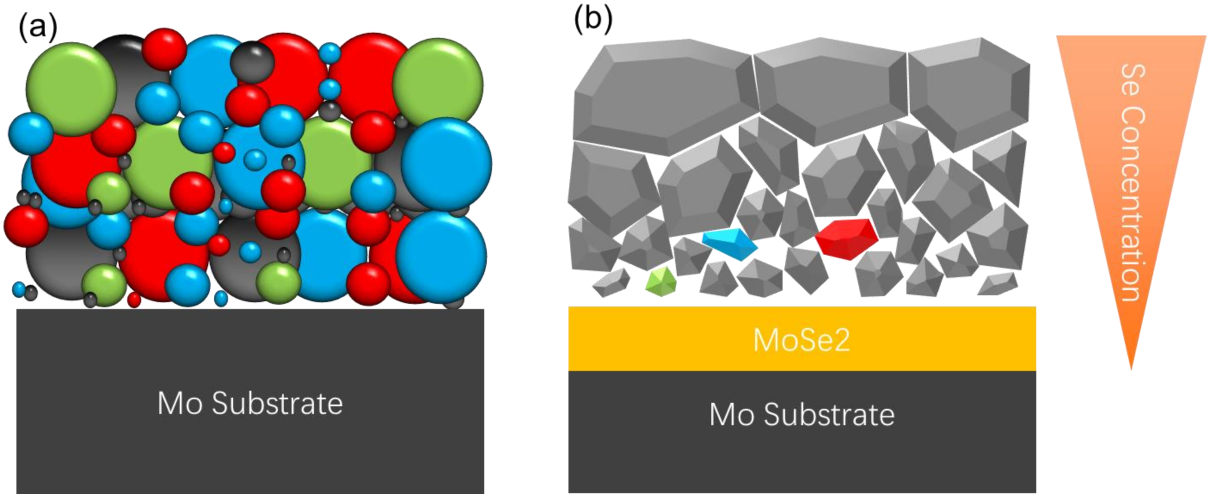

Figure 24 Schematic of the selenization process. (a) is before selenization. Different colored spheres represent precursor nanoparticles with different phases. (b) is after selenization. Colored crystals are secondary phases.

Chapter 4

Impurity Phases in CZTSe thin film solar cells

4.1 Non-stoichiometry and point defect in CZTSe

Figure 5(a) shows a HAADF image of a CZTSe single crystal with zone axis of [100]. As can be seen from the HAADF image and the simulation in Figure 5, we can confirm that the final phase is the kesterite CZTSe. In this image, the brightest atom is Sn, which has an atomic number of Z=50. The four less bright atoms around the Sn are Se, which has an atomic number of Z=34. The eight dimmest atoms are Cu and Zn, and their atomic numbers are 29 and 30. Since the Z of Cu and Zn are so close so that they can't be distinguished by the Z-contrast image. However, certain population of point defects are expected to be responsible for the non-stoichiometry of the CZTSe.

Most high efficiency CZTS cells have compositions around Cu/(Zn+Sn) = 0.9 and Zn/Sn = 1.25, which are Cu-poor and Zn-rich. First principles calculations show that the intrinsic point defects in Cu-poor CIS thin films are copper vacancies (V_{Cu}^{-}), which can electrically passivate the primary donor antisites of In_{Cu}^{2+} by forming stable neutral defect complexes of ($In_{Cu}^{2+} + 2V_{Cu}^{-}$), leaving no deep-gap levels in the electronic structure. Therefore, despite the large population (~1 at.%) of intrinsic point defects in Cu-poor CIS films, the films perform satisfactorily for photovoltaic applications[112, 113]. The addition of Ga is beneficial, increasing the band gap by about 0.2 eV in $Cu(In_{1-x}Ga_x)Se_2$ (CIGS) films with x≤0.3. Higher Ga concentrations introduce deep level point defects of Ga_{Cu}^{2+} and reduce the stability of the passive defect complexes.[114, 115]

Theoretical studies have also suggested non-classical benign effects of extended defects, especially grain boundaries in polycrystalline CIGS. Although still under debate, first principles modeling suggests that grain boundaries in polycrystalline CIGS may act as hole barriers (and electron sinks) under Na doping to prevent electron-hole recombination,[116] or they may act as charge-neutral defects, electrically inactive for carrier transport.[116-119] Such benign grain boundary behavior is contrary to classic grain boundary theory, but it is supported by experimental observations in CIGS films using scanning Kelvin probe microscopy,[118, 120-123] Auger electron spectroscopy,[124] and current imaging tunneling spectroscopy.[125] This grain boundary behavior provides a reasonable explanation for the high performance of fine-grained polycrystalline CIGS solar cells.[126] Even so, a few reports studying grain boundary-dependence of solar cell output parameters point out that the influence of grain boundaries can still be destructive to device performance when neutral grain boundaries are located within the depletion region and are parallel to the junction direction.[127, 128]

Compared to CIGS, CZTS has not received as extensive research regarding its defect formation mechanisms and structure-property relationships. Notably, the quaternary compound nature of CZTS allows for more possible permutations of point defect complexes than the ternary nature of CIGS (where Ga is isoelectric to In). A theoretical study by Raulot et al.[71] suggests that the deeper-level acceptor antisite Cu_{Zn}^{-} in CZTS has lower formation energy than V_{Cu}^{-}. In the past few years, there have been controversial reports on whether V_{Cu}^{-} or Cu_{Zn}^{-} is the dominant intrinsic defect in CZTS under Cu-poor and Zn-rich conditions.[15, 68, 69, 73] Despite the uncertainty in identifying dominant defects, it is generally agreed that the point defects in CZTS are at deeper levels (near mid gap) than in CIGS. Therefore, it is suggested that the increased disorder in CZTS results in increased non-radiative recombination at grain boundaries that harm device performance.[15, 67]

The point defects and the non-stoichiometry of the CZTSe may also result in a change of the CZTSe crystal structure. In general, it is widely accepted that the I_2-II-IV-VI_4 compounds are most stable in kesterite structure, however, some found that stannite structure can also be detected for monocrystalline CZTSe[31]. Nateprove et al. determined using X-ray diffraction that the most stable structure of CZTSe should be in the space group of $I\bar{4}2m$, which means that it is evolved from either structure with copper and zinc atoms statistically occupy the same position with the equal probability[129]. This work is confirmed by Schorr et al. that partial disorder of Zn and Cu in kesterite structure is observed through neutron scattering[130]. Such disorder of Cu and Zn will transform the symmetry of kesterite from $I\bar{4}$ to a disordered $I\bar{4}2m$ which is the same space group as stannite structure. There are still debating on whether the CZTSe exhibits kesterite structure, stannite structure, or a mixture of both.

Recent studies have observed a change of symmetry in the CZTS system from ordered kesterite ($I\bar{4}$) to disordered stannite ($I\bar{4}2m$) if the material is Cu-poor. In Raman spectroscopy, this appears as a peak shift from 337cm^{-1} for the $I\bar{4}$ symmetery to 331cm^{-1} for the $I\bar{4}2m$ structure [131]. Figure 25 shows a CZTSe main peak position mapping of a 50 by 50 μm top area. The blue region (region 1) has peak position around 192 cm^{-1}, which represents the disordered $I\bar{4}2m$ structure, while the red region (region 2) has peak position around 198 cm^{-1}, which corresponds to ordered $I\bar{4}$ symmetery. Because in the Cu-poor condition the high population of V_{Cu}^- and Zn_{Cu}^+ can generate a slight widening of the peak. Hence in our CZTSe samples, there is a coexistence of ordered kesterite structure and disordered kesterite/stannite structure. And such variation may be caused by the local Cu concentration variation. The inhomogeneity in composition can cause the Cu content to vary throughout the film. In general, a Cu-poor environment is preferred for the formation of $[V_{Cu}^- + Zn_{Cu}^+]$.[72] The Cu-rich environment can reduce the hole barrier so that the enhanced collection of carriers near GBs will be overcome by recombination. These Cu-rich GBs can reduce the V_{OC}[132] and may be the main cause of low cell efficiency. Raman mapping can be used to study the variation of the Cu content along the film.

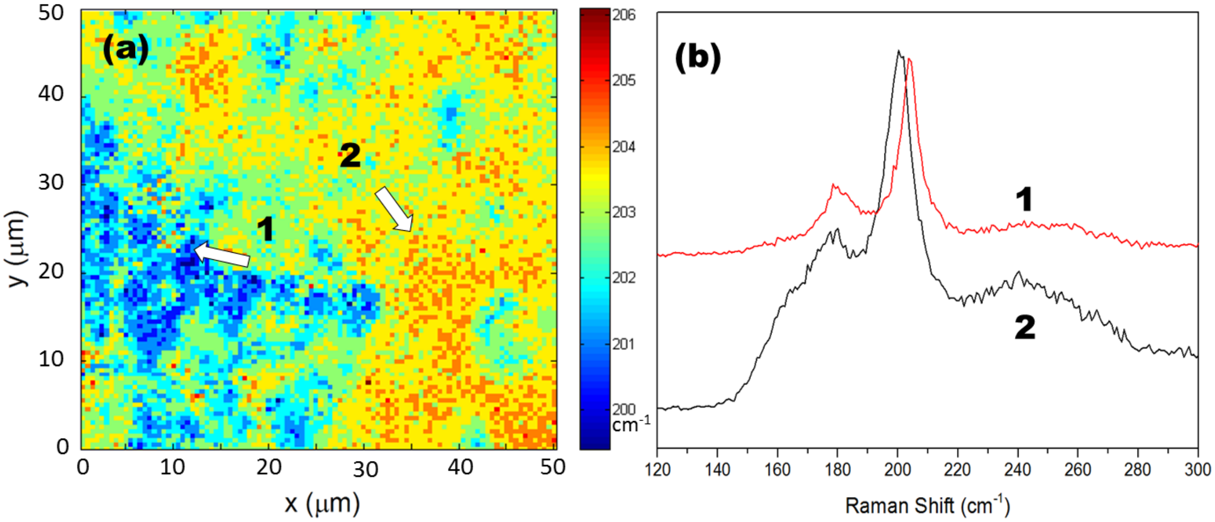

Figure 25 Symmetry mapping by Raman spectroscopy. (a) A map of the CZTSe primary peak position over a region of 50 by 50 μm. The red area shows a shift to the left corresponding to Cu-rich kesterite with the $I\bar{4}$ structure. The blue region indicated the Cu-poor $I\bar{4}2m$

4.2 Phase segregation in CZTSe

The more the elements are in a compound, the more degrees of freedom of chemical composition and structure it will have. It is much more complicated to synthesize the quaternary CZTSe solar cell absorber than binary compound such as CdTe, or ternary compound such as CIS. It is extremely important to control the composition of the elements during the synthesizing process to avoid the generation of binary or ternary secondary phases. In CZTSe system, there are four elements that can be combined to form a lot of secondary phases such as CuSe, Cu2Se, ZnSe, SnSe, and Cu2SnSe3. As can be seen from the phase diagram, the window is quite narrow to form the stoichiometric CZTSe, and any change of the composition or growth environment can lead to the shift of the equilibrium state and the formation of these secondary phases. In practice, it is found to be extremely difficult to synthesize single-phase CZTSe, and they only exist in small quantities. The tolerability of component deviation is 1-2% for stannite CZTSe below 550 °C, and that range of chalcopyrite is around 4%[133, 134].

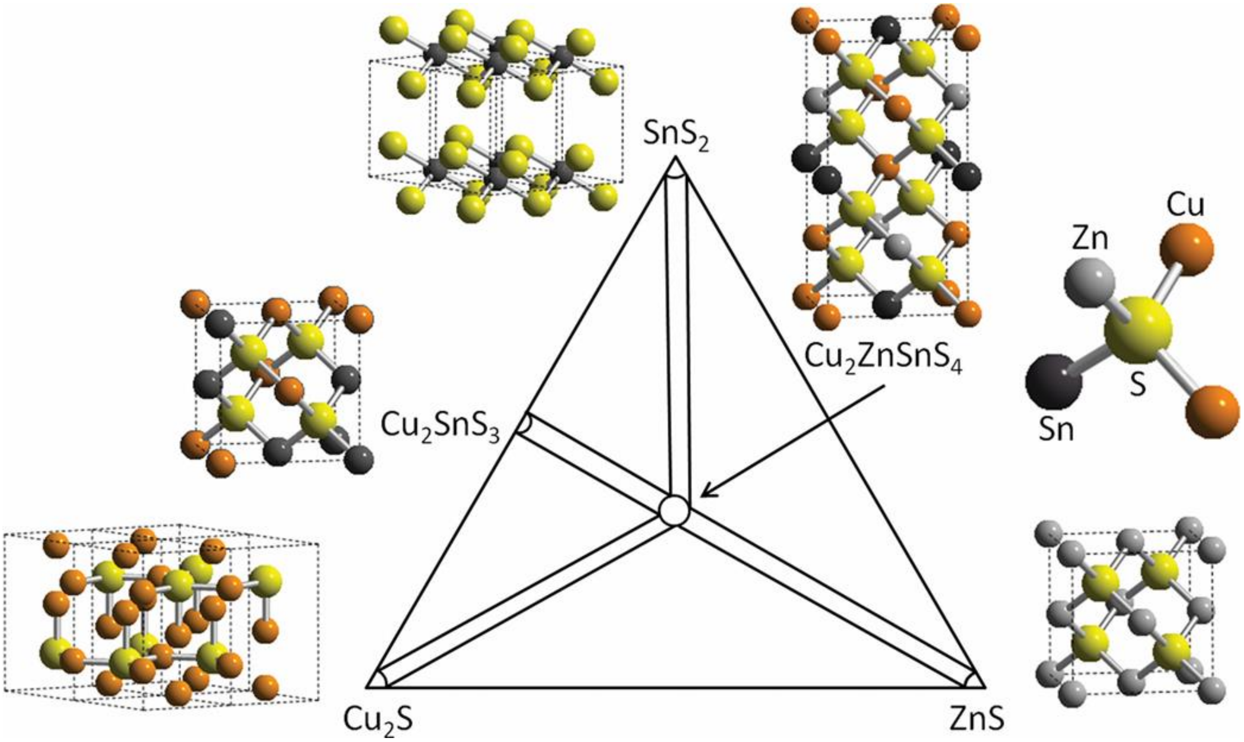

Figure 26 Schematic of the thin film Cu_2S-ZnS-SnS_2 ternary phase diagram at 325 °C deposition temperature. The crystal structures of CZTS and the observed secondary phases are also presented, with unit cells represented by dashed lines. In the schematic of Cu_2SnS_3, the cation sublattice is randomized with respect to Cu and Sn occupancy[135].

It is worth noticing that, most of the CZTS(Se) cells that exhibit maximum efficiencies are obtained in Cu-poor and Zn-rich condition, where Cu/(Zn+Sn) = 0.8 and Zn/Sn = 1.22, while the cells that have the composition deviated from these two values tends to have lower efficiencies[136]. For a Cu-poor and Zn-rich condition, first-principles studies has confirmed that the stable regions of

CZTSe in the chemical potential phase diagram are even smaller than that of Cu-rich scenario, and secondary phases such as ZnSe is likely to form in a Cu-poor condition[136]. The formation of ZnSe secondary phase in CZTSe has been observed commonly[137, 138]. They have a bandgap around 2.7 eV and is usually non-conductive and does not affect the shunting resistance, however forming a large layer of ZnSe inside the CZTSe may lead to in increment of series resistance[137, 139]. Other impurities such as SnSe, CuSe, or Cu2SnSe3 are more effective reducing the shunting resistance and the open-circuit voltage, leading to a low efficient device[34]. Figure 26 shows the ternary phase diagram of SnS2-Cu2S-ZnS and the atomic structure of different secondary phases. And Table 2 shows bandgaps of most common secondary phases in CZTS(e) system.

Table 2 Most common secondary phases in the Cu- Zn-Sn-S/Se system[34, 140]

Compound	**Bandgap (eV)**	**References**	**Compound**	**Bandgap (eV)**	**References**
Cu_2ZnSnS_4	1.5	[34]	$Cu_2ZnSnSe_4$	1.0	[34]
Cu_2SnS_3	0.9	[141]	Cu_2SnSe_3	0.8	[142]
ZnS	3.7	[143]	ZnSe	2.7	[143]
SnS_2	~ 2.5	[144]	$SnSe_2$	1.0–1.6	[145]
SnS	1.0 indirect, 1.3 direct	[146, 147]	SnSe	1.3	[148]
Cu_2S	1.2	[149]	Cu_2Se	1.2	[150]

To spatially resolve the secondary phases that may form after the selenization process, we performed Raman spectra mapping on our top view samples. Figure 27 shows the Raman mapping study of two different secondary phases on the same 10μm by 20μm area of a top view CZTSe sample. Figure 27a and b are the mappings of the relative intensity of a ZnSe 250 cm^{-1} peak and a CuSe 263 cm^{-1} peak. In these two mappings, brighter regions have higher peak values. Hence, the two highlighted spots (marked as 1 and 2) indicate that ZnSe and CuSe precipitates are present in these regions. The three Raman spectra in Figure 27c represent three different points of the film. Among these spectra, the two peaks at 172 and 195 cm^{-1} belong to CZTSe, and they can be observed throughout the entire region of the film. The second spectrum, taken at point 1 in Figure 27a, shows an additional peak at 263 cm^{-1}. This peak belongs to CuSe, a degenerate semiconductor, one of the major secondary phases that can hinder cell performance. CuSe can be observed both on top and bottom surfaces of the film, indicating that the formation of CuSe during selenization can not only occur at the top surface but also at the interface between the CZTSe film and the Mo substrate. Unlike material forming on the top surface, which can be etched away using KCN, CuSe at the bottom surface will remain inside the film even after the etching process. These regions can form shunting paths that reduce the fill factor of the cell. They can also increase recombination at rear surface and thus lower the EQE at long wavelength. The third spectrum has a peak at 250 cm^{-1}. It belongs to ZnSe and can also be found inside the film. Due to the large bandgap of ZnSe compared to CZTSe, it will create an inactive region that doesn't respond to illumination from the solar spectrum, leading to a reduction of the total effective area of the device.

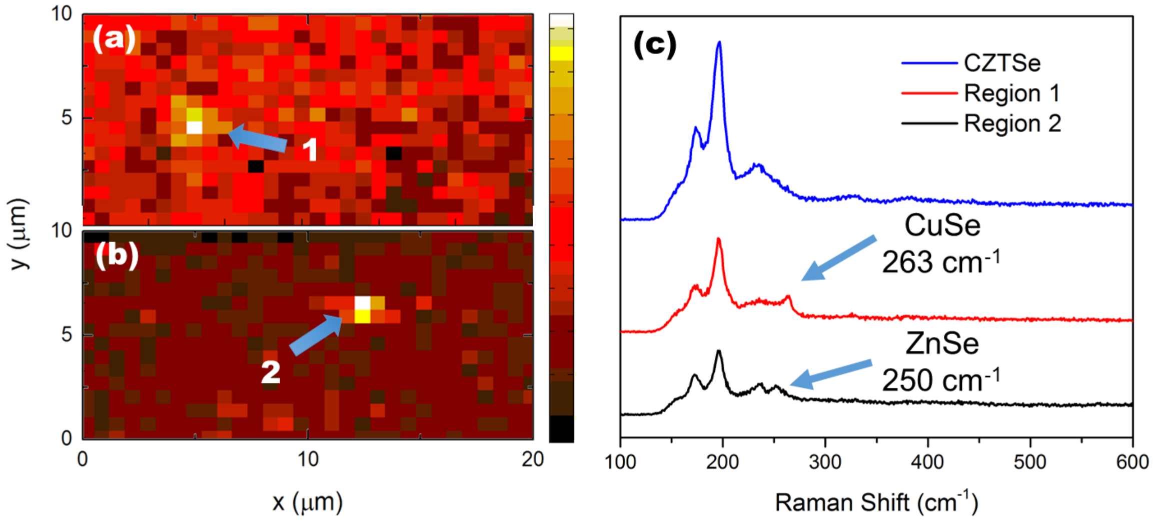

Figure 27 Secondary phases detected by Raman spectroscopy. Raman spectra mapping of the (a) CuSe (263 cm-1) peak and (b) ZnSe (250 cm-1) peak from the same region. (c) Raman spectra of a pure CZTSe phase region and 2 spots with secondary phases located in (a) and (b).

During the selenization process, the volatile SnSe phase will escape from the film, leaving the excessive Cu and Zn to form CuSe and ZnSe. Once the CuSe has formed, the saturated Se vapor will then react with CuSe to form Cu2Se, whose melting temperature is close to the annealing temperature. These Cu2Se will be extracted to the surface and form large liquid droplets at the surface of the CZTSe, resulting a gradient of Cu concentration across the film. These Cu2Se precipitates that form on the top surface of the CZTSe can be etched away by KCN solution, thus will have little impact on the cell efficiency. Figure 28 shows that the CuSe2 (small particles on the surface of CZTSe grains) has been removed after being submerged in a KCN solution for one minute. However, with the Cu being driven to the surface, a concentration gradient has formed. The deeper inside the film the lower the Cu concentration will be. And such deficiency of Cu leads to a formation of ZnSe inside the CZTSe grain. Since ZnSe has very similar crystal structure to that of CZTSe and the lattice constant is closely matched, the mobility of the ZnSe precipitate are much lower that of the Cu2Se. Once the ZnSe forms a contentious layer inside the CZTSe film, it will settle down and block the penetration of Se vapor and result in a layer of incomplete selenized CZTSe beneath the ZnSe layer. Figure 29 shows a typical structure of a CZTSe device with double layer configuration. Most of the cells with such configuration leads to very low efficiencies (<1%) because the ZnSe layer act as a barrier to the hole collection, and the bottom layer is not completed transformed into CZTSe.

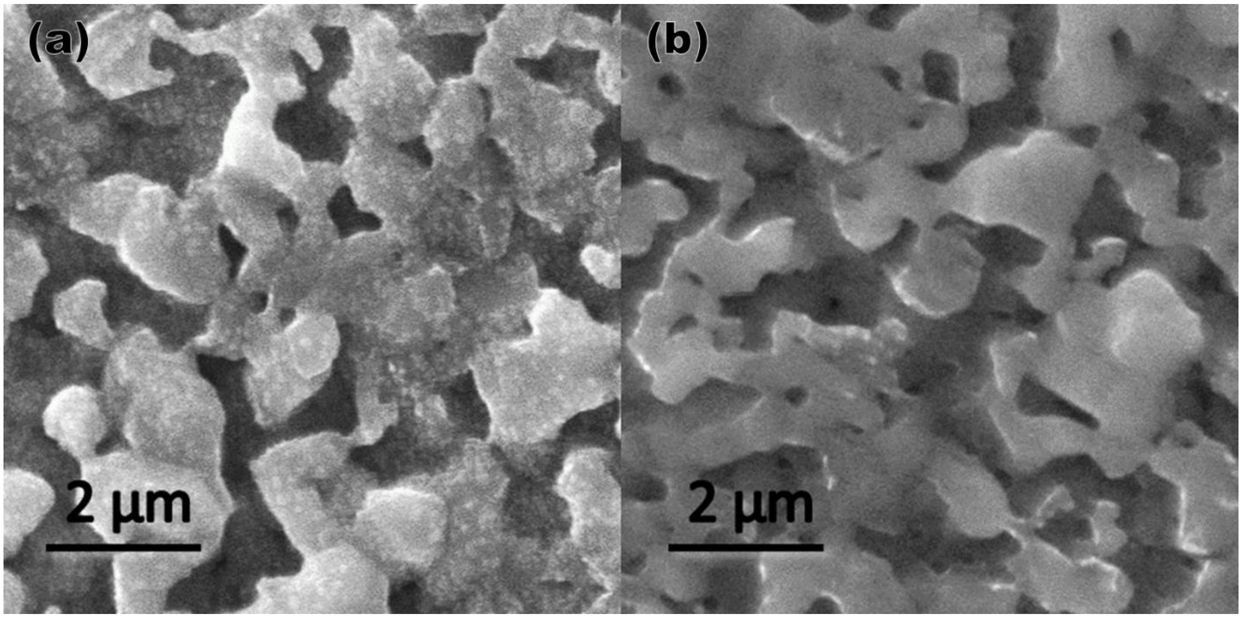

Figure 28 Removal of CuSe by KCN etching. SEM top view imaging of a CZTSe film (a) before and (b) after being etched by KCN.

Furthermore, the band mismatch at the interface of the CZTSe and the isolated ZnSe particles that forms within them can also trap electrons towards their interface. Figure 30shows the mean inner potential(MIP) mapping and the EDS mapping of a CZTSe/CdS/ZnO/ITO device. The region within ZnSe precipitates has a reduced inner potential, indicating a high conductive band offset to the surrounding CZTSe. At the interface, The CZTSe also shows increased potential, which corresponding a band distortion at the interface where the electrons are trapped. Since the ZnSe has similar structures to CZTSe, these precipitates usually form inside the CZTSe. These precipitates provide a generous amount of ZnSe/CZTSe interface to trap the electrons and thus are responsible for the total reduction of the efficiency of the CZTSe solar cell systems. When under illumination, additional electron-hole pair is created and is separated by the depletion field at the junction. For a ZnSe imbedded in the CZTSe, the electrons will be driven towards the interface and being trapped in the triangle well while the holes will move freely into the CZTSe matrix. As a result, the Fermi energy level near the interface will be shifted and the built-in potential will be reduced by the localized free electrons. When this region is illuminated for a period of time that is long enough for the triangle well to be filled up by the free electrons, the newly created electrons will then be able to escape from the interface of ZnSe and CZTSe and move into the CZTSe matrix. However, as the presence of recombination sites caused by the defects at the interface, a generous amount of free electron carriers is consumed here thus the total efficiency of the solar cell will be hindered. This effect can be observed by the electron holography since the conductive band structure is related to the electron potential mapping. Figure 31 shows the potential mapping of a ZnSe precipitates that is embedded inside the CZTSe matrix with and without illumination. As can be seen from the mapping, there is a potential barrier at the interface that represents a triangle potential well. This barrier is reduced as the area undergoes illumination, which means that this region is being filled by the free electrons. The reason that this barrier is not completed overcome is due to the recombination that takes place simultaneously.

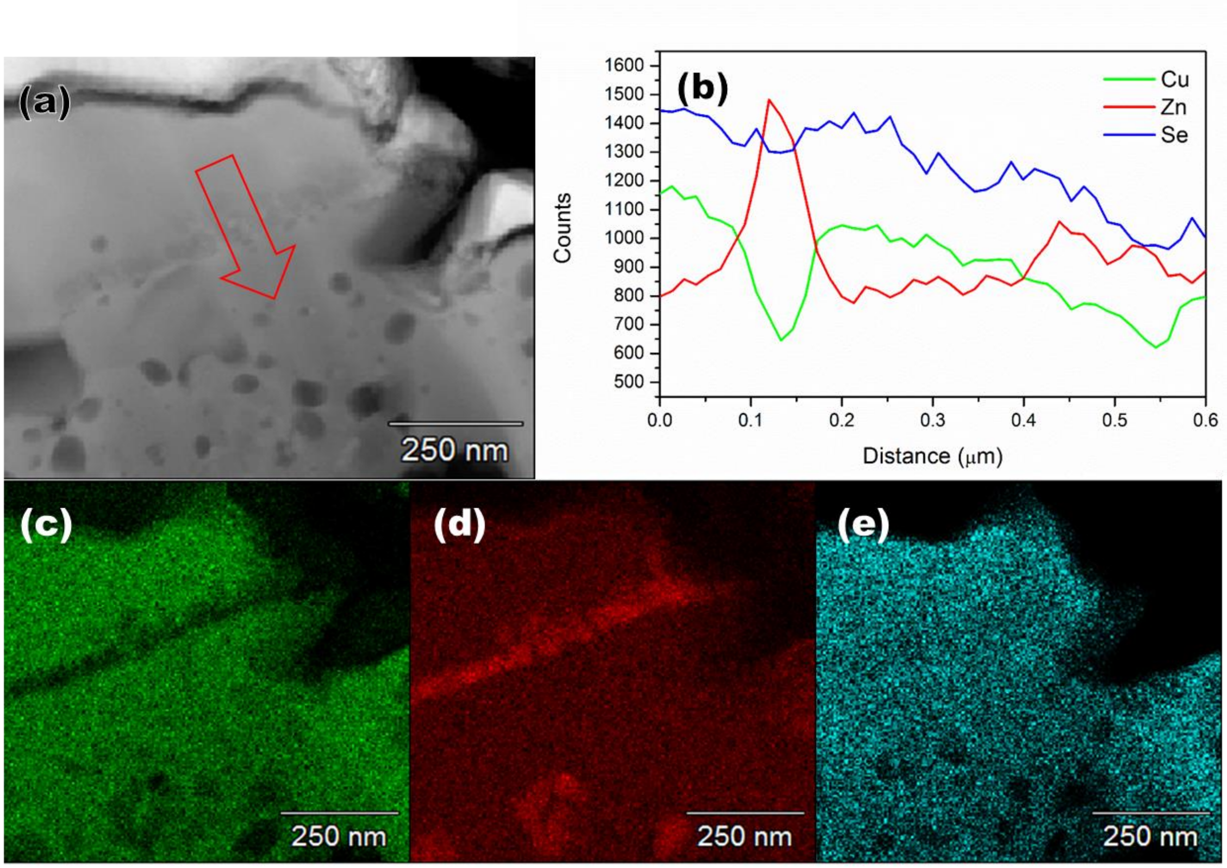

Figure 29 EDS mapping of CZTSe that exhibit double-layer structure. (a) A STEM HAADF imaging of a CZTSe device that shows double layer structure. (b) is the EDS line profile marked by the arrow in (a). (c)-(e) are the Cu, Zn and Se mapping of a same region in (a).

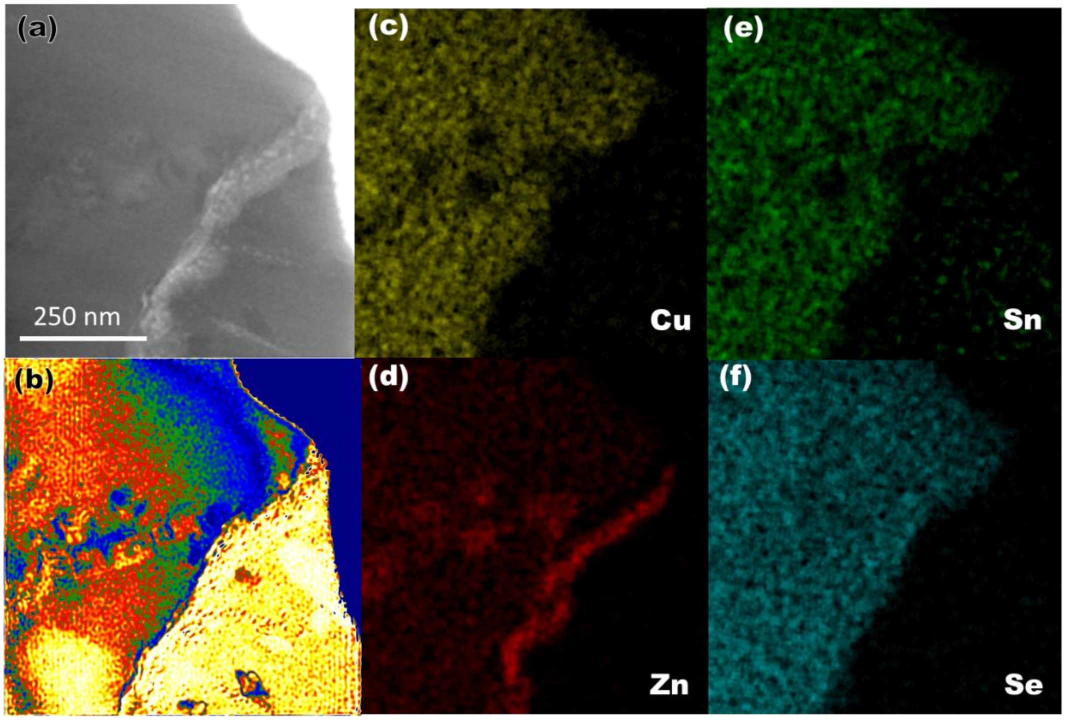

Figure 30 Combined EDS and holography on a CZTSe film with ZnSe impurity phase. (a) A STEM ABF imaging of a CZTSe device prepared by FIB. (b) is calculated inner potential mapping (CIP) of (a). (c)-(f) are EDS element mapping of Cu, Zn, Sn, and Se in (a).

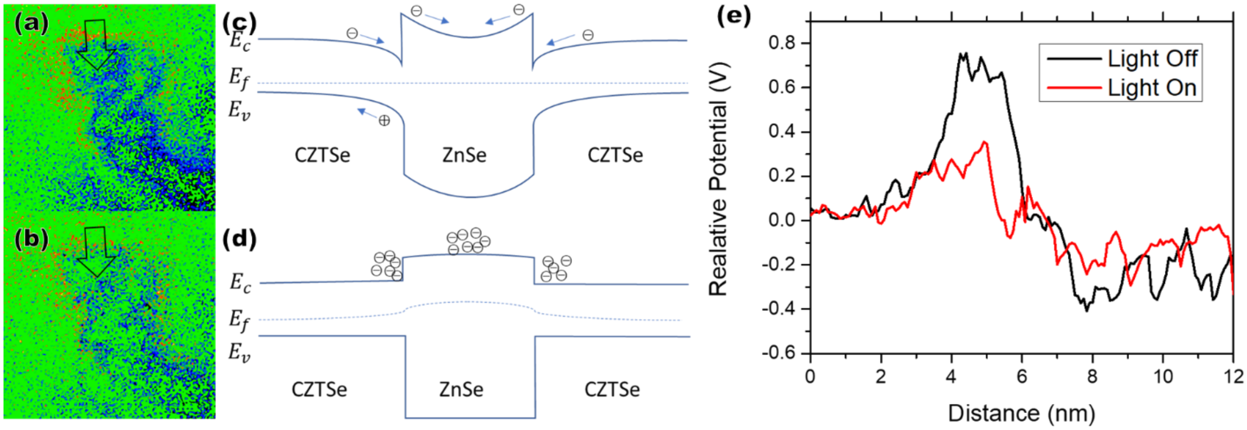

Figure 31 in-situ holography mapping with optical illumination on a ZnSe imbedded in CZTSe. (a) and (b) are the potential mapping around a ZnSe precipitate imbedded in a CZTSe matrix with illumination off and on. (c) and (d) are the band diagram of the corresponding situation in (a) and (b). (e) is the potential line profile across the arrow marked in (a) and (b). The CZTSe matrix is used as a zero-potential reference.

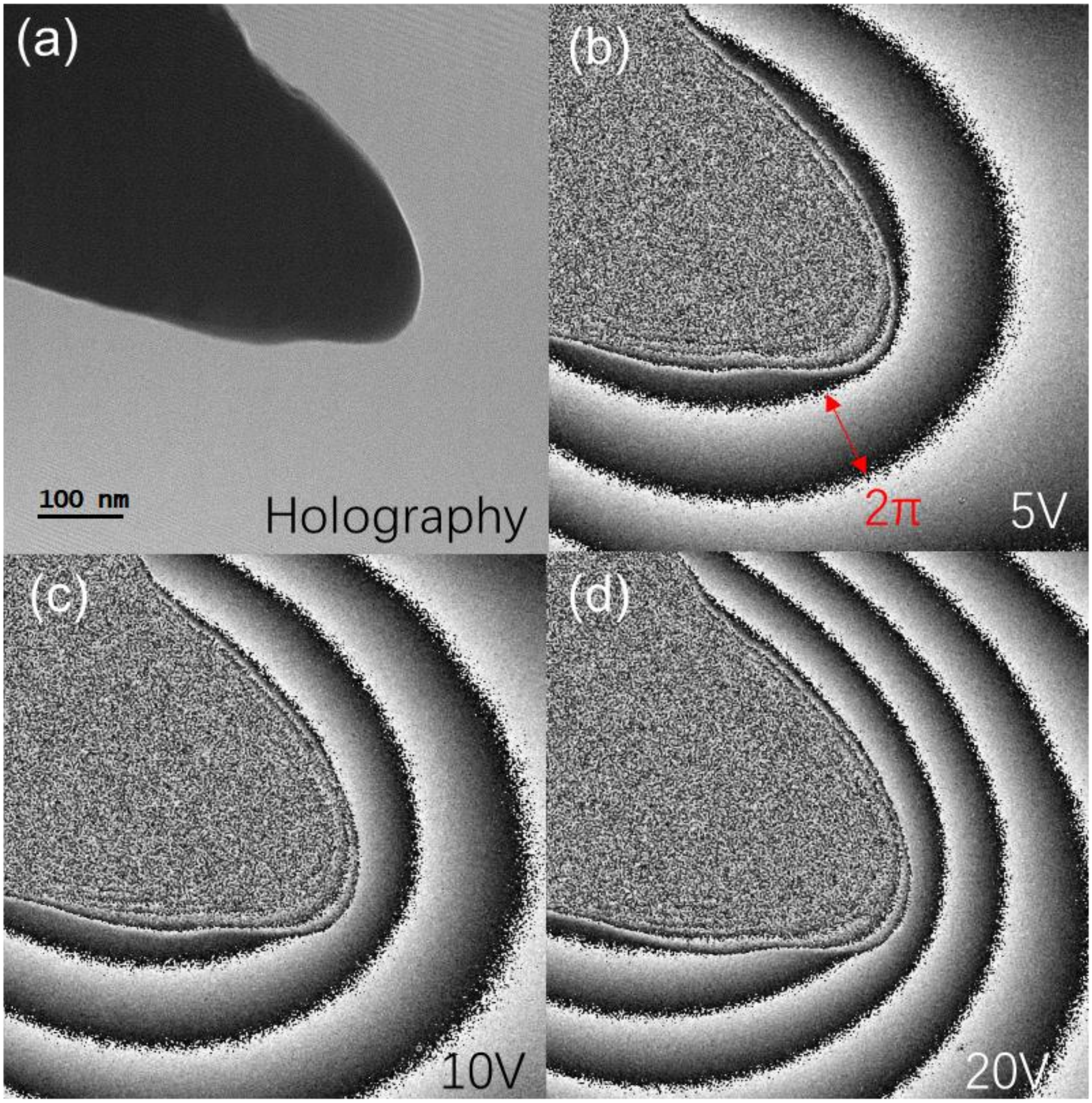

Figure 32 phase mapping around a biased W tip (a) a hologramof a W tip in the vacuum. (b) to (d) are phase mapping of the tip under 5, 10 and 20 V biasing.

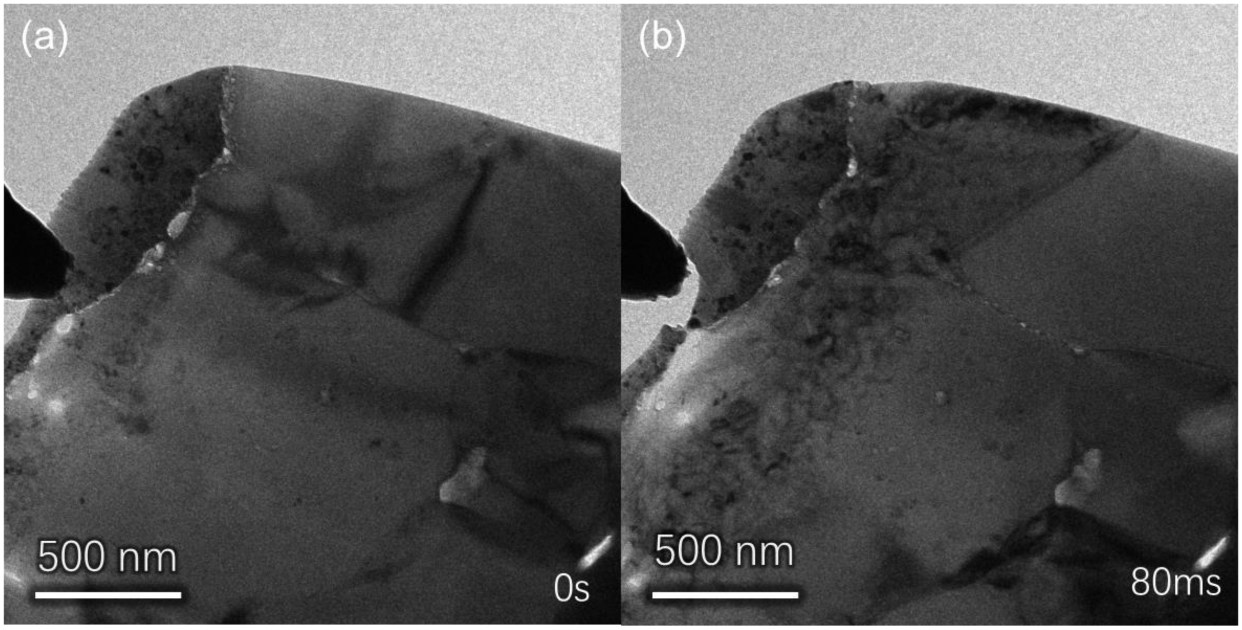

Figure 33 in-situ Joule heating of the CZTSe sample under 5V biasing. (a) is the TEM image before re-solidification and (b) is the TEM image after the re-solidification

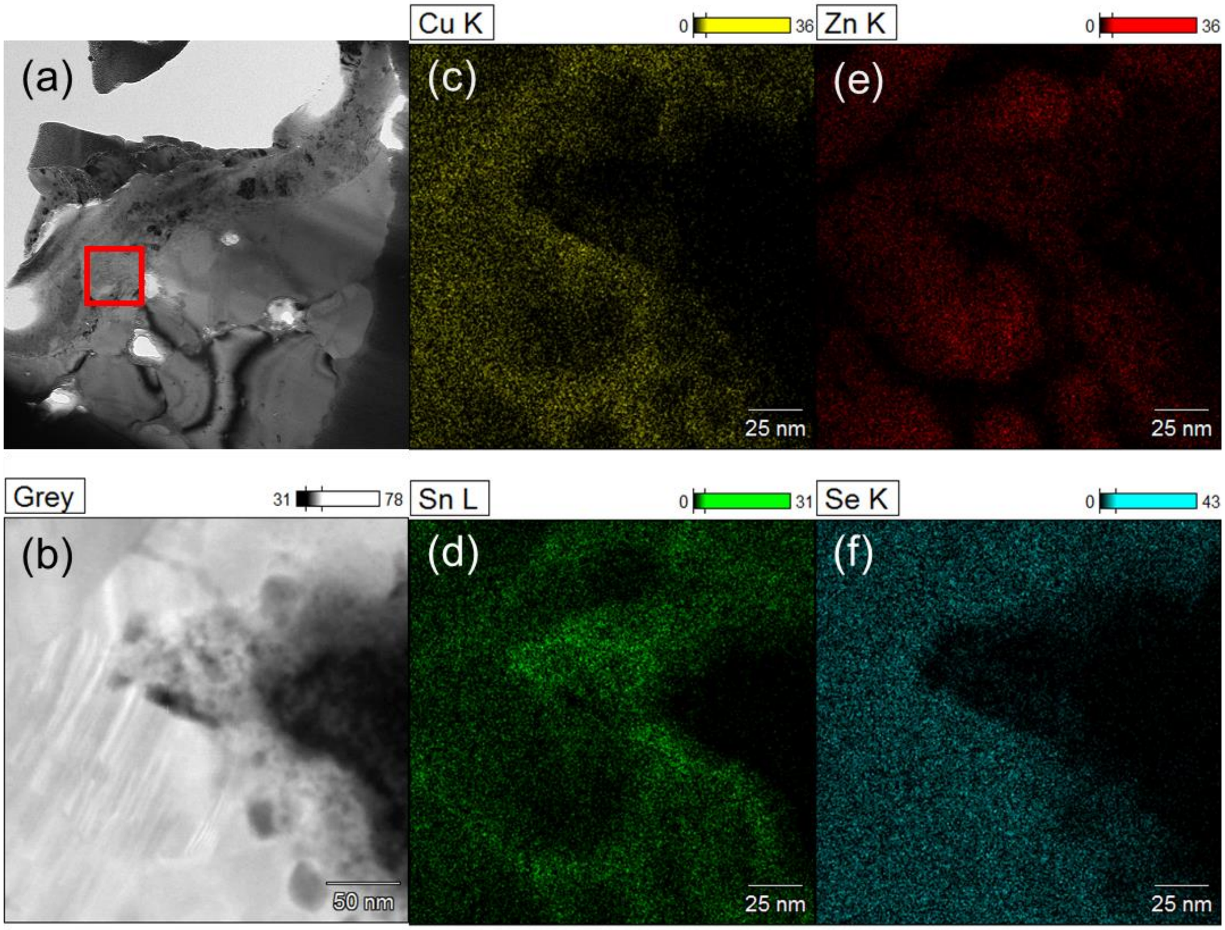

Figure 34 EDS mapping of re-solidified CZTSe crystals. (a) is the TEM BF imaging of a CZTSe device that is partially re-solidified. (b) is the HAADF imaging of the region highlighted in (a). (c) to (f) are EDS elemental mapping of the region in (b).

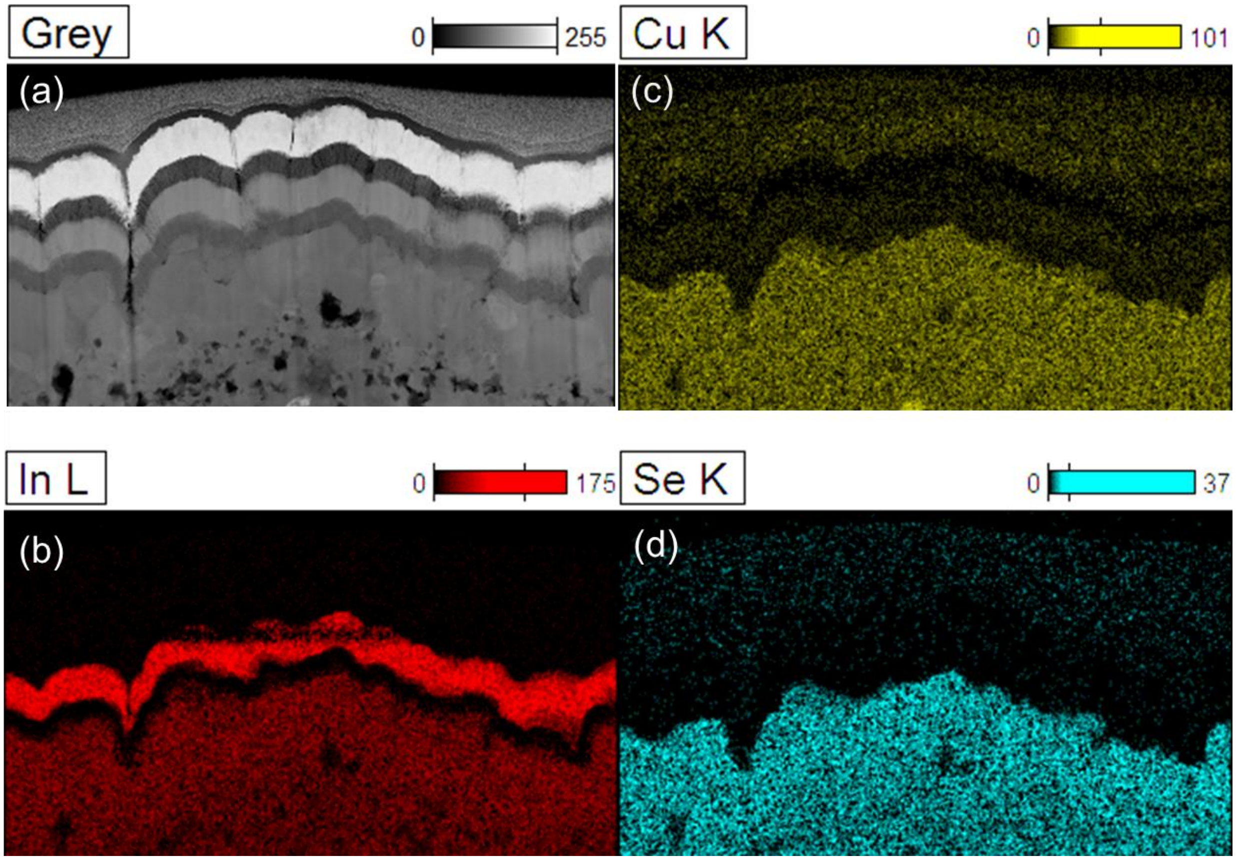

Figure 35 EDS mapping of CIGS. (a) is a HAADF imaging of CIGS device prepared in FIB. (b) to (d) are EDS elemental mapping of Cu, In and Se of the region in (a).

4.3 Other impurities in CZTSe

In addition to the phase segregation inside the CZTSe film, we also observed carbon residues that tapped inside of the CZTSe grain. Figure 36 shows the HAADF imaging and the EDS mapping of a carbon particle found inside a CZTSe grain. The carbon particles are likely being introduced during the LP-PLA process while the target is submerged in acetone. After the EPD process, most of the acetone are evaporated and escapes from the precursor film. However, there are still some residues being trapped between the precursor nanoparticles, which later form carbon clusters during the selenization process. These carbon impurities are commonly found inside the CZTSe grains, and they can form electrically “dead” zone since they don’t produce any free carriers. Figure 36g shows a 3d plotting of potential mapping near a carbon particle. As can be seen from the mapping, there is no significant potential change on neither side at the interface, suggesting a pure ohmic contact between CZTSe and C. However, the residual carbon particles can potentially contribute to the large population of defects within the CZTSe grains. As can be seen from the Figure 36b, the carbon particle forms a shell that coats the surface of the CZTSe. The empty core of the carbon precipitate is likely to be caused by the decomposition of acetone when the precursor nanoparticles are selenized. These voids create a generous amount of free CZTSe surfaces, which are responsible for not only the point defects such as vacancies and anti-sites, but perhaps also extensive ones such as dislocations, twin boundaries, and stacking faults. Figure 37 shows the region in CZTSe where dislocations, twin boundaries and stacking faults are found in the region with densely populated carbon precipitations. These extensive defects can act as recombination center and hence hinder the performance of the CZTSe solar cells.

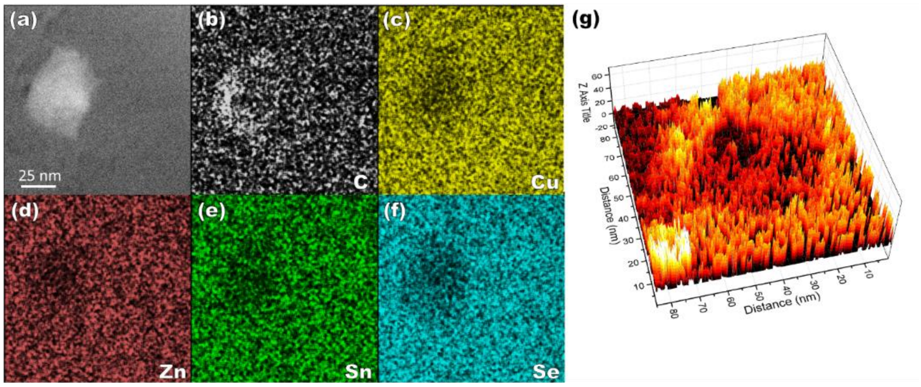

Figure 36 Combined EDS and holography on a carbon impurity phase in CZTSe. (a) STEM bright field imaging of a carbon particle imbedded in the CZTSe. (b) to (f) are elemental EDS mapping of C, Cu, Zn, Sn, Se of the region in (a). (g) is a 3D plot of potential mapping near the same particle in (a).

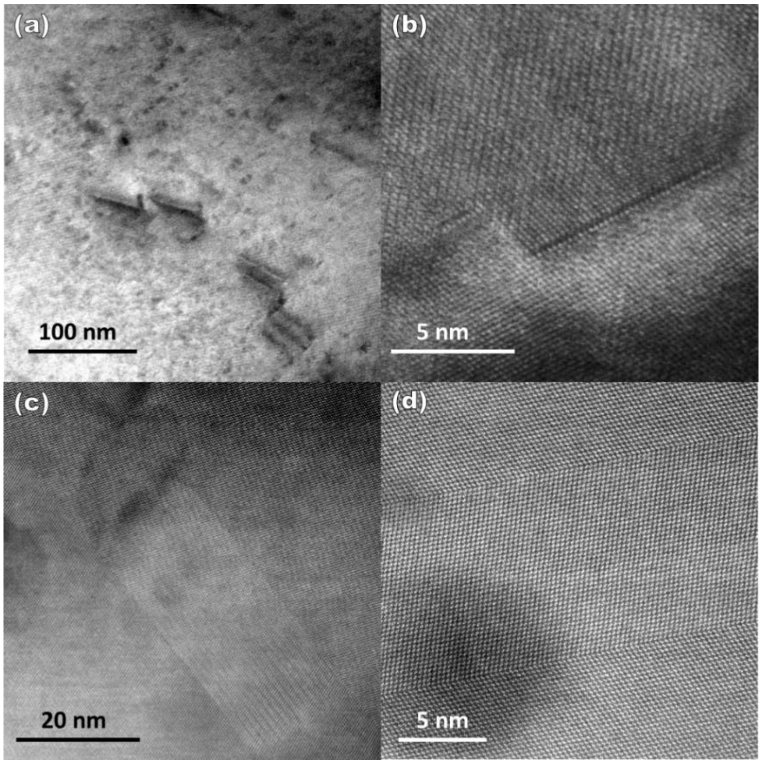

Figure 37 Defects found near carbon impurities in CZTSe. (a) is a TEM bright field imaging of a CZTSe grain. (b) is an HRTEM image of a dislocation found in (a). (c) and (d) are HAADF imaging of precipitates that are found at the twin boundaries and stacking faults.

Besides the carbon impurities, we found that the oxidation of the CZT precursor may also affect the final product of CZTSe. As can be observed from Figure 14, Figure 17, Figure 18,Figure 19 and Figure 29, most of the CZTSe films exhibit a double-layer structure: a layer of fine grains of CZTSe mixed with precursor nanoparticles and secondary phases are found in between the large CZTSe grains and the substrate. Figure 6 and Figure 38 are EDS elemental mappings of two clusters of fine grains that are scraped from the substrate and dispensed on the carbon film. Both regions exhibit high oxygen signal covering the surface of the particles. In addition, the highlighted region in Figure 38 shows four spherical particles that has strong Cu and O signals, and lack of Zn, Sn, or Se signals. The formation of such layer can be explained by the irreversible reaction to form MoSe2 hat take place at the interface of CZTSe and Mo. The precursor film is exposed to the atmosphere for a short period of time before entering the selenization process. Such exposure will result the nanoparticles being oxidized, and the smaller the particle is, the higher the volumetric ratio of the oxide shell will be. Before these precursor nanoparticles become selenized, they undergo a reversible reaction where oxygen is substituted by selenium:

$$2MO + 2Se \leftrightarrow 2MSe + O_2 \qquad M{:}\, Cu, Zn, Sn$$

This product on the right-hand side is extremely difficult to produce because the electronegativity of O (3.44) is much larger than that of Se (2.55). Hence high temperature and excessive Se environment is important for the formation of O_2. However, at the interface of precursor film and Mo substrate, the majority of Se vapor is consumed by Mo and form irreversible product of MoSe2. Hence the oxide layer of the precursor particles will be maintained and the core will be slowly selenized as the Se diffuses and reacts with the metal inside the precursor particles. The final product will be a selenide-oxide core-shell structure that will not sinter and form larger CZTSe grains.

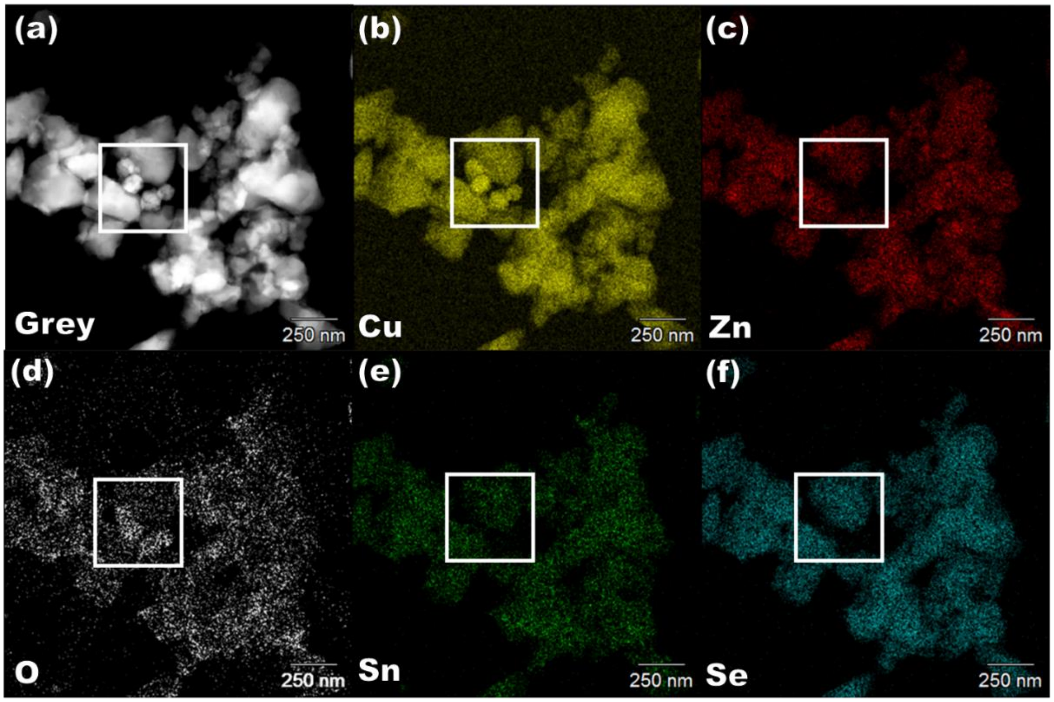

Figure 38 EDS mapping of CZTSe fine particles. (a) An HAADF imaging of a cluster of CZTSe crystals that is scrapped from the device. (b) to (f) are elemental EDS mapping of Cu, Zn, O, Sn and Se. The highlighted region are four un selenized Cu nanoparticles.

Figure 21 shows the EDS mapping of the CZTSe films with two distinct grain sizes. It is apparent that the region with smaller grain sizes exhibit higher oxygen content. Similarly, the precursor particles will also stop growing when additional oxygen is introduced into the furnace. This usually occurs then the furnace tube is not properly sealed or the graphite box has been left in the ambient environment for too long. The oxygen in the selenization process will compete with the selenium vapor so that the precursor particles will be oxidized instead of selenized and form large crystals.

One way to avoid this is to keep the furnace tube pressurized with argon so that the oxygen can’t flow in through the leaking point. In addition, the graphite box should also be stored in a vacuum chamber for the oxygen to be degassed.

Chapter 5

Grain Boundaries in CZTSe

5.1 Electrical benign grain boundaries in CZTSe and CIGS

Local variation of Cu content can result in different electrical properties of the GBs. Figure 39 is a dark current mapping of a 10 by 10 μm region on a top CZTSe film on Mo substrate. With a positive sample bias voltage of 1 V, a brighter area in the spreading resistance image represents a higher conductivity. From Figure 39b, despite the uniform conductivity within the GBs, higher conductivity regions are found mostly near the GBs. This indicates that the carrier concentrations are increased near these GBs. Figure 40 shows an optoelectrical analysis of a CZTSe device using C-AFM mapping. A defocused 532 nm continuous wave laser with total power of 1 mW was used as illumination surrounding the conductive diamond coated AFM tip to excite photocurrent. In Figure 6b, the zero current regions are replaced by the grey scale topography. Under zero bias, a photocurrent of as high as 350 pA can be detected near some of the GBs. This result clearly indicates that for CZTSe devices, the carrier collection is enhanced at these GBs. However, for the rest of the GBs, no photocurrent is collected near them, suggesting recombination-dominant behavior of these GBs. The classic Seto model[151] of polycrystalline Si and simulations[128] of CIS and CGS solar cell systems predict a down shift of both valance and conduction band energy for columnar GBs. In the CGS system, a reduced VBM of as high as 0.55V can occur under Cu poor conditions[152]. The electrons are attracted towards the reconstructed GB cores and start accumulating near them to form depletion regions. These depletion regions, or even inverted regions, are responsible of high carrier concentration and high conductivity near the GBs. The origin of this phenomenon is that the polarization at the cation-terminated (112) surface can cause Cu-vacancy surface reconstruction, reduce the p-d repulsion and lower the VBM.[116, 152] This will drive the Cu ion at GBs towards the grain interiors (GIs) so that the GBs are occupied by V_{Cu}^-, and the less the symmetry at the GBs, the larger the offset will be.[153]

Such enhanced carrier collection near these GBs is reported to be the major cause of the benign effect of GBs for CIGS.[124, 154, 155] It is therefore likely for the CZTSe system, belonging to the same chalcopyrite family as CIGS, to have a similar effect of enhanced carrier collection near those GBs.

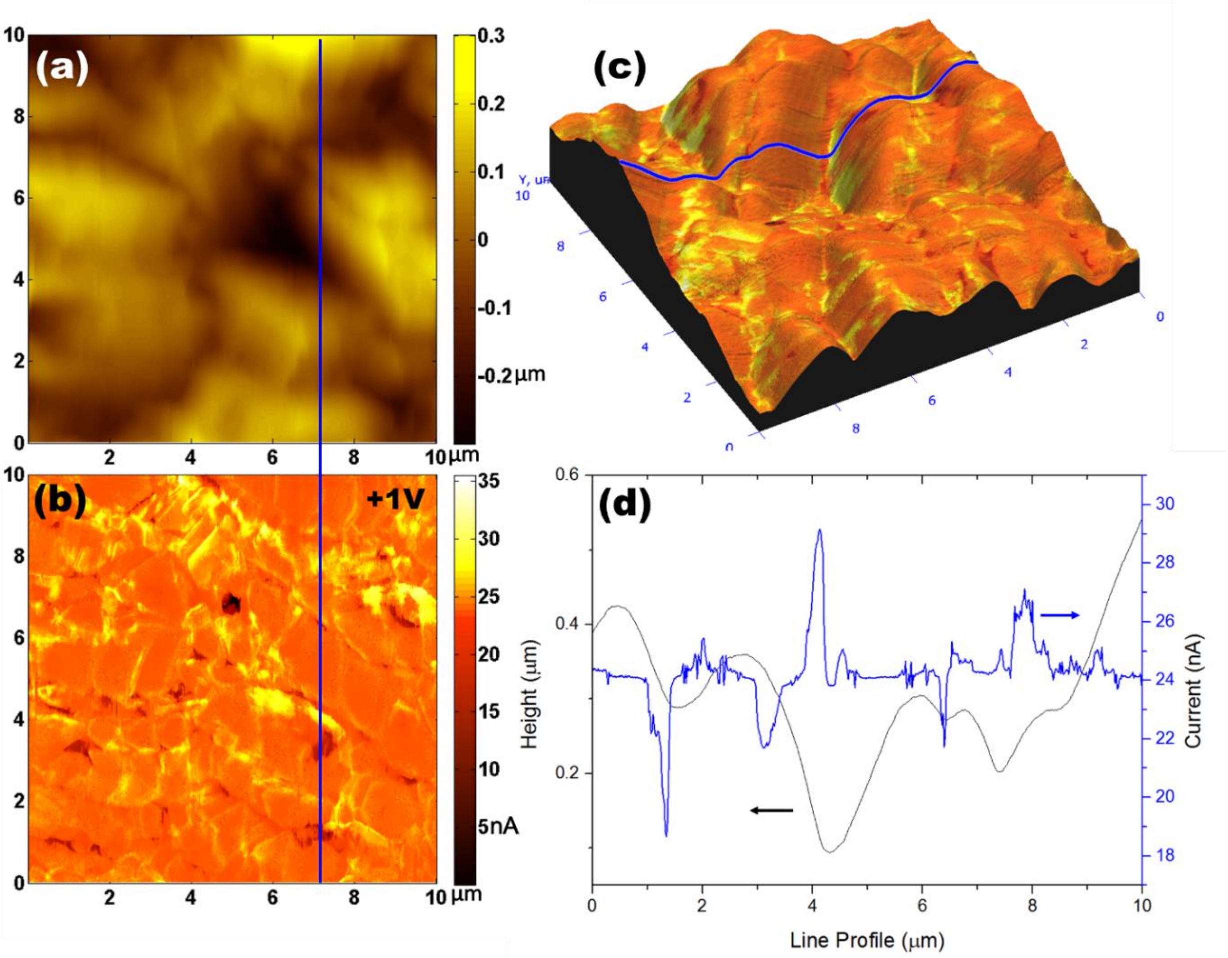

Figure 39 C-AFM mapping on a CZTSe film with 1V bias. a) An AFM surface topography of a polycrystalline CZTSe film in contact mode. b) The current mapping of the same region under +1 V bias. c) The 3d model of the superimposed mapping of a) and b). d) The line profile of the height-current relationship in the region marked in blue line in a), b) and c).

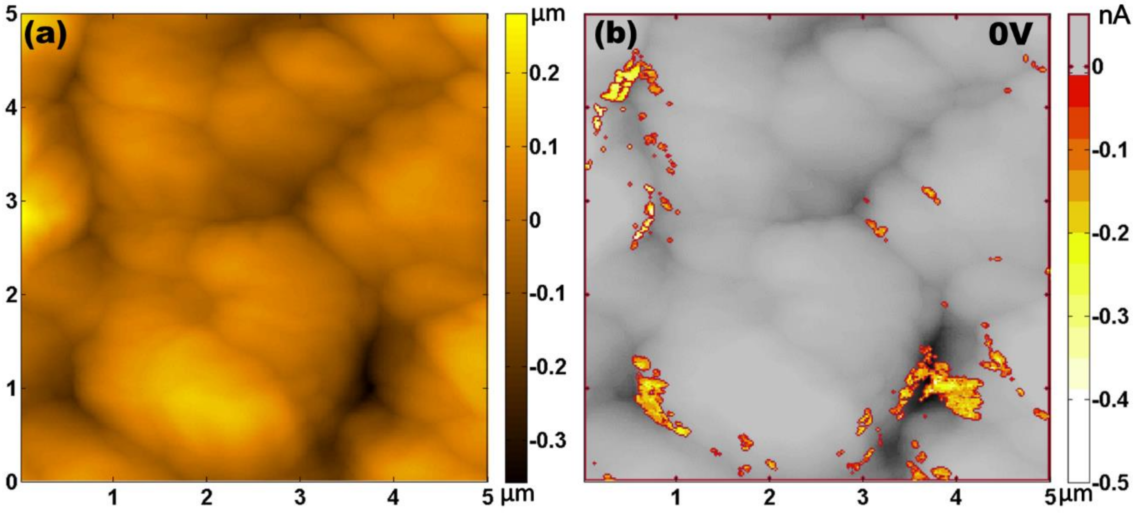

Figure 40 C-AFM mapping on a CZTSe device with illumination and zero bias(a) AFM topography of the top surface of a CZTSe device. (b) Zero biased photocurrent mapping, under illumination of a defocused 532 nm contentious wave laser with total power of 1mW. The photocurrent mapping is superimposed on the topography in (a) to illustrate the correlation between the position of the photo current and that of the GBs.

5.2 Asymmetrical Grain Boundary behavior of CZTSe crystals

However, the electrical benign GB model of CIGS may not complete agree with that of CZTS system because the best lab cell efficiency of CZTSSe is only about 60% of that of CIGS. As we measured the electrical conductivity near the GBs of the CZTSe thin films using c-AFM, we noticed that the conductivity of the region near one side of a GB is always significantly higher than the other (Figure 39). In another word, only one side of the GB agrees with the electrical benign model of CIGS, while the other side has much less conductivity to contribute to the minority carrier collection. Such asymmetrical behavior near the boundary is very common in the CZTSe system thus can be the reason why CZTSSe shows a lower energy conversion efficiency compared to the CIGS system. Such asymmetrical behavior does not only occur near the grain boundaries, but can also be found in a much broader scope. Figure 41 shows c-AFM mapping of 2 different surfaces of the CZTSe film. Figure 41a shows a region with highly ordered crystal facets. The results indicate that the high conductive regions no longer occur at the grain boundaries, but can be found at the entire surface of certain facets. Although extremely rare are these regions, they are mainly found in cells with high efficiencies. These surfaces are most likely to be the cation terminated (112) surfaces and such phenomenon agrees well with the band model of the CZTSe system. Figure 41c, which shows a region with less perfect facet configuration, doesn’t have as pronounced facet dependent conductivity change as region a, and the more conductive region occurs mostly at the GBs. These regions are more commonly found in our CZTSe films. To study this facet dependent asymmetrical electrical properties of CZTSe, we mapped the inner potential of some of the twin boundaries using the off-axis electron holography. Figure 42 shows a holography across one asymmetrical GB in CZTSe. As can be seen from Figure 42c, the potential of one side is significantly higher than the other side, meaning the conduction band minimum (CBM) across the GB is also asymmetrical. The higher the potential is, the lower the CBM will be, thus the carrier concentration and conductivity are also higher. Figure 43 shows in-situ biasing through the CZTSe device that generates joule heating that degenerates the CZTSe crystals. As the GBs are more conductive, the current density the went through these GBs will be much higher thus they start degenerating first (Figure 43b, e). The grain interior will be heated up and degenerate in a later stage (Figure 43c, f). during the investigation of these GBs we found that they also exhibit asymmetrical Cu concentration (Figure 44).

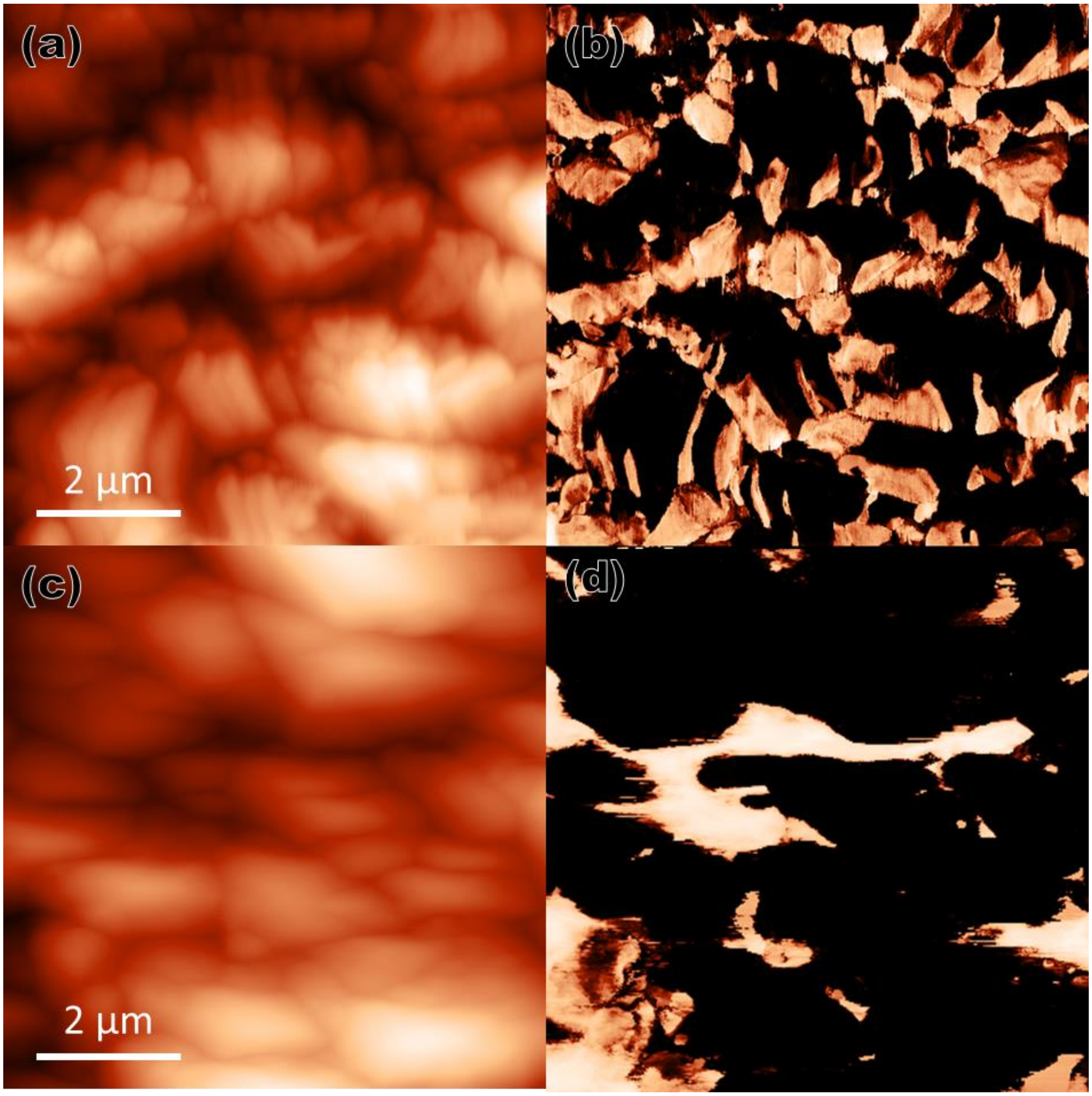

Figure 41 Two region in CZTSe that exhibit different electrical behaviors. (a) AFM topography of a CZTSe film region with ordered facet configuration. (b) is the c-AFM mapping of the region in (a). (c) AFM topography of a CZTSe film region without ordered facet configuration (d) c-AFM of the region in (c).

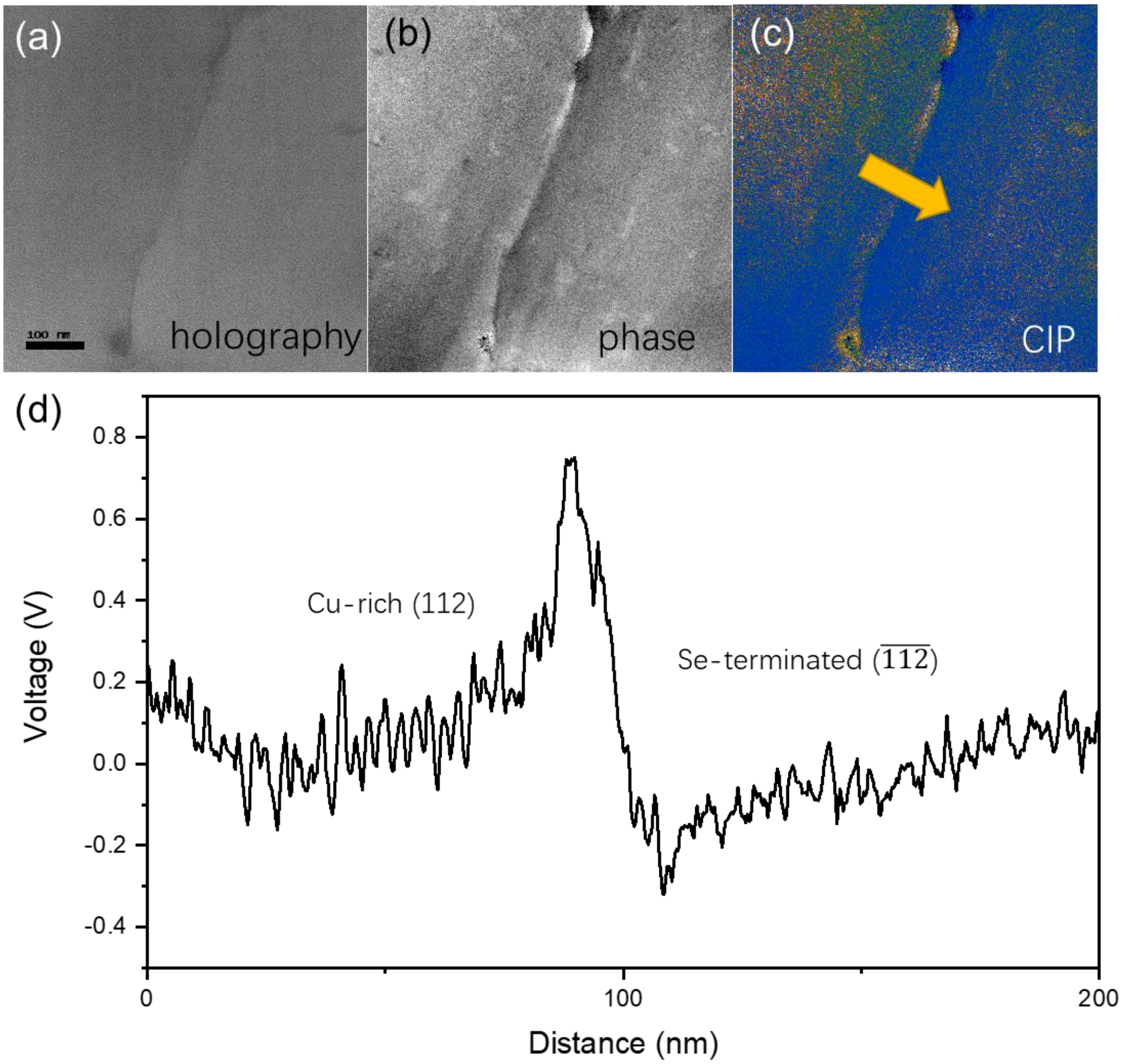

Figure 42 Off-axis holography of an asymmetrical GB in CZTSe. (a) to (c) are holography, phase and CIP mapping of the same GB. (d) is the CIP line profile of the highlighted region in (c).

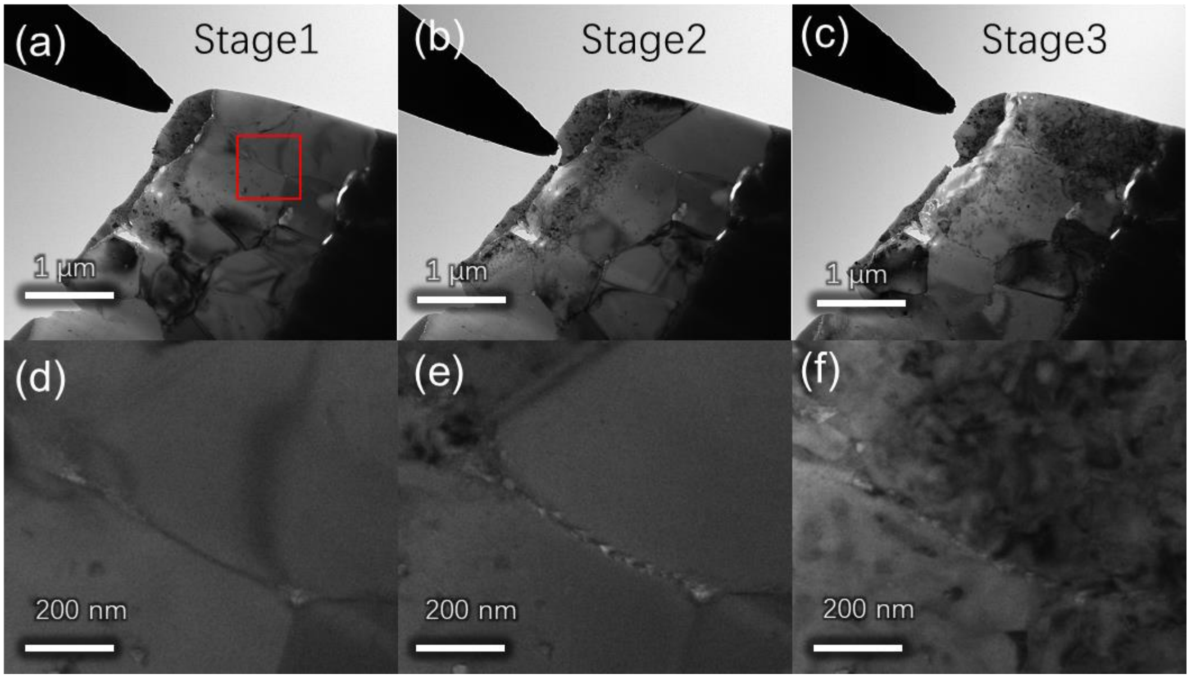

Figure 43 in-situ biasing of CZTSe device. (a) to (c) are TEM BF images of different stages during the in-situ biasing of CZTSe. (d) to (f) are enlarged TEM BF images of the highlighted region in (a).

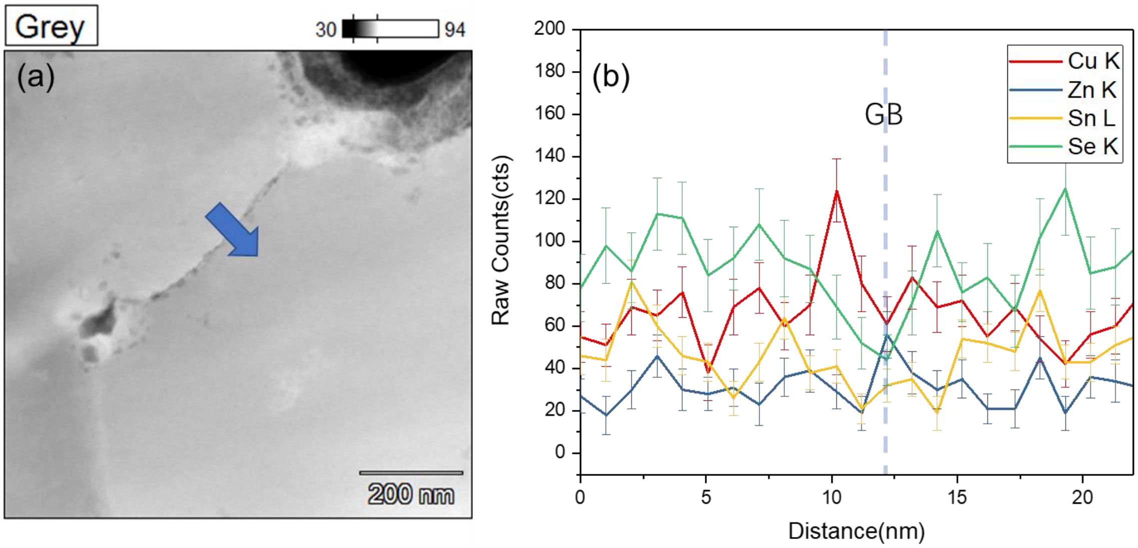

Figure 44 EDS line scanning of an asymmetrical GB in CZTSe. (a) is the STEM HAADF imaging of a GB in CZTSe. (b) is the EDS line profile of Cu, Zn, Sn and Se across the GB indicated in (a).

Figure 45 shows the cross-sectional CIP imaging of the CZTSe/CdS/ZnO/ITO device prepared by FIB. The CIP mapping located 2 parallel GBs at the top left region, which was then indexed by

HRTEM and FFT pattern. Note that both GBs are twin boundaries, and due to the orientation of this 3 grains, the HRTEM of region I and II are taken from different zone axis to review the change of crystal orientation across the GB. From the CIP mapping one can see that the overall CIP of grain 1 is about 4 V higher than the CIP of grain 2, and this value between grain 2 and 3 is about 1 V. For the interface between grain 2 and grain 3 (Region II), one can also observe a potential change near the GB. In region I the potential change of the two grain interior agrees with the c-AFM data in figure X where one side of the grain surface is significantly more conductive than the other side. In region II, there is a potential barrier located at the GB, and the potential of grain 3 gradually increases as it reaches the GB. This case agrees with the c-AFM data in figure X that most of the conductive region are found near GBs and one side of GB is always more conductive than the other side.

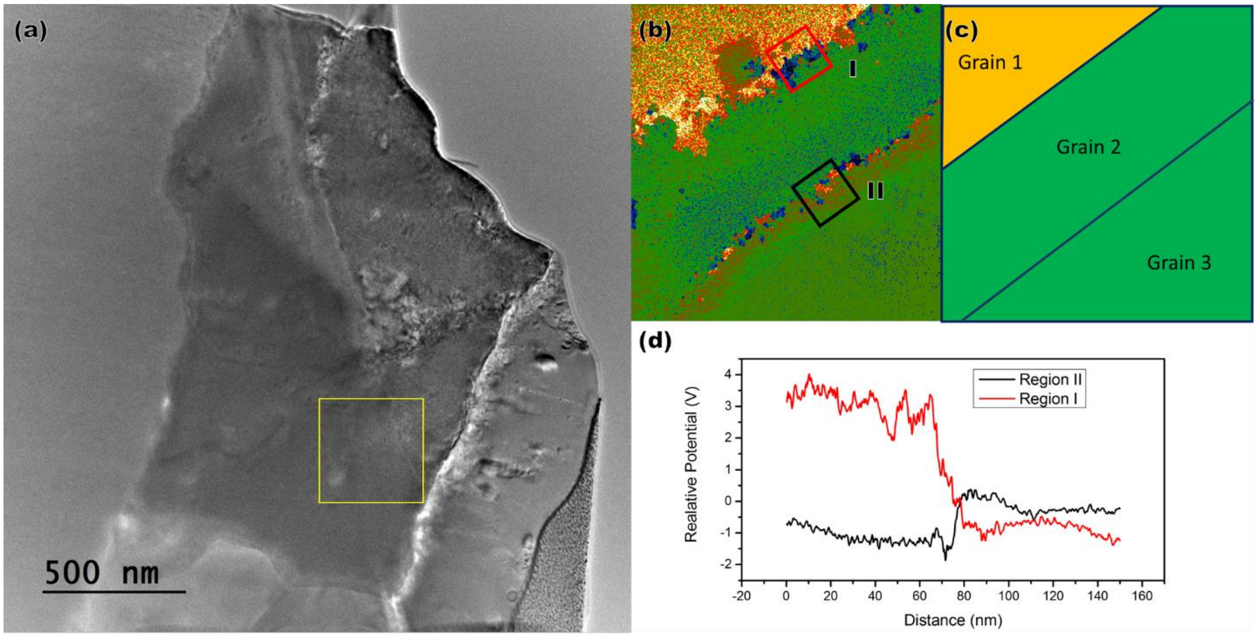

Figure 45 Potential mapping across two twin boundaries. (a) TEM imaging of a cross-sectional CZTSe device prepared by FIB. (b) is the CIP mapping of the region marked in (a), (c) is the schematics of the structure in (b). (d) is the potential line profile of Region I and II across the GBs. The grain 3 is used as a reference for zero potential.

5.3 Cation terminated (112) planes in CZTSe and their contribution to band distortion near GBs

Such different potential profiles can also be explained by the electrical benign (112) surface of CZTSe. When taking electron holography of a CZTSe TEM sample with grain surfaces perpendicular to the beam direction belonging to different plane families, the entire grain may have different potentials. Figure 46 shows the crystal orientation of the 3 grains in the same region of Figure 45. Grain 1 has a (112) plane that is perpendicular to the beam direction, while for grain 2 and grain 3 these are both (100) planes. Since only grain 1 has a (112) plan that is perpendicular to the beam direction, we observed a potential increment for the entire grain. On the other hand, since the planes that are perpendicular to the beam direction are from the same family, we observed that grain 2 and 3 have the same potential at the grain interiors, and the potential offset only occur at the GB.

For the cation terminated (112) surfaces, the conduction band minimum will shift downward if the surface is Cu-rich. It helps attracting electrons but creates recombination center at the same time. The valance band maximum will shift downward for (112) surface if it's Cu-poor, and GBs that contain such Cu-poor (112) surface is preferred because it repulses holes[156]. For the anion terminated $(\overline{112})$ surfaces, the VBM and CBM offset can be neglectable and therefore these surfaces make little contribution to the carrier collection. When the (112) plane forms at the surface of the CZTSe crystal, the entire facet will be conductive; When the (112) plane forms at the GB, the GB will become conductive at the side that contains the (112) plane. In the first case, only when the (112) plane that forms at the interface of CZTSe/CdS can electrons be collected. When the (112) plane forms at the bottom electrode, the trapped electrons will recombine with the nearby holes. In the second case, only vertical GBs that connect to the CdS can contribute to the collection of electron; when horizontal GBs are formed, the electrons that are attracted to them will never reach the CdS before recombination. This asymmetrical behavior doesn't only apply to the twin boundaries. In the case of random GBs, the phenomenon is the same. Figure 47 is a potential mapping across a random boundary. As can be seen from the line profile, the potential change of the two grains is also 5 V, which agrees with the case I in Figure 45. Figure 48 shows the potential mapping of random GBs between 4 grains. From the potential mapping, we can see clearly the co-existence of the 2 types of GBs. Grain 1 has a (112) facing to Grain 2; Grain 4 has a (112) facing to the vacuum; Grain 3 and 4 don't have significant change of potential, hence their (112) plane should be orthogonal to the beam direction. The nature of such asymmetrical behave might due to the preferential growth of the (112) planes. In kesterite systems, the selenium terminated ($\overline{112}$) surface has the lowest surface free energy because each Se atom only have one dangling bond that is orthogonal to the surface. When exposed in air, these bonds can easily bind with H^+ in the atmosphere and become stable; for the cation terminated (112) surface, the surface free energy is much higher because in order to bind with O^{2-}, certain surface reconstruction is needed. On the other hand, cation terminated (001) surface may also be stable because oxygen can bind with the two adjacent cations alone [1-10] direction with minimal bond distortion. Such energy variation of the bond distortion for different facets may result in variation of the electrical properties for CZTSe solar cells. However, the details about the surface reconstruction and its relation to the electrical properties are beyond the scope of this article. Further study is needed.

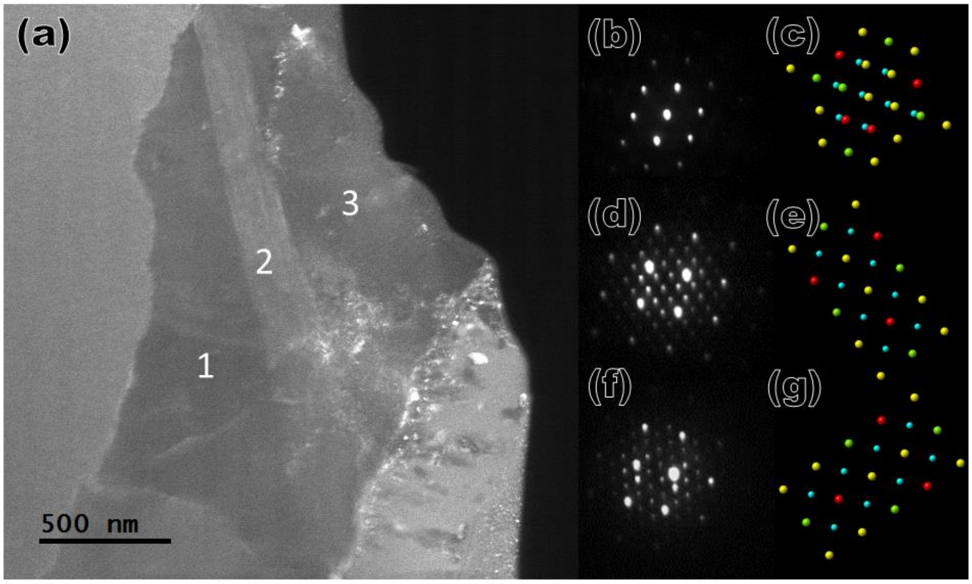

Figure 46 Crystal orientation relationship of a CZTSe grain that has two twin boundaries (a) A TEM image of a cross-sectional CZTSe device prepared by FIB. (b) is a dark field image that highlighted grain 2 and 3; the model and the diffraction pattern of grain 1 is shown to the right. (c) is a dark field image that highlighted grain 2; the model and the diffraction pattern of grain 2 is shown to the right. (d) is a dark field image that highlighted grain 1 and 2; the model and the diffraction pattern of grain 3 is shown to the right. The Cu, Zn, Sn and Se atoms are colored in yellow, red, green and blue.

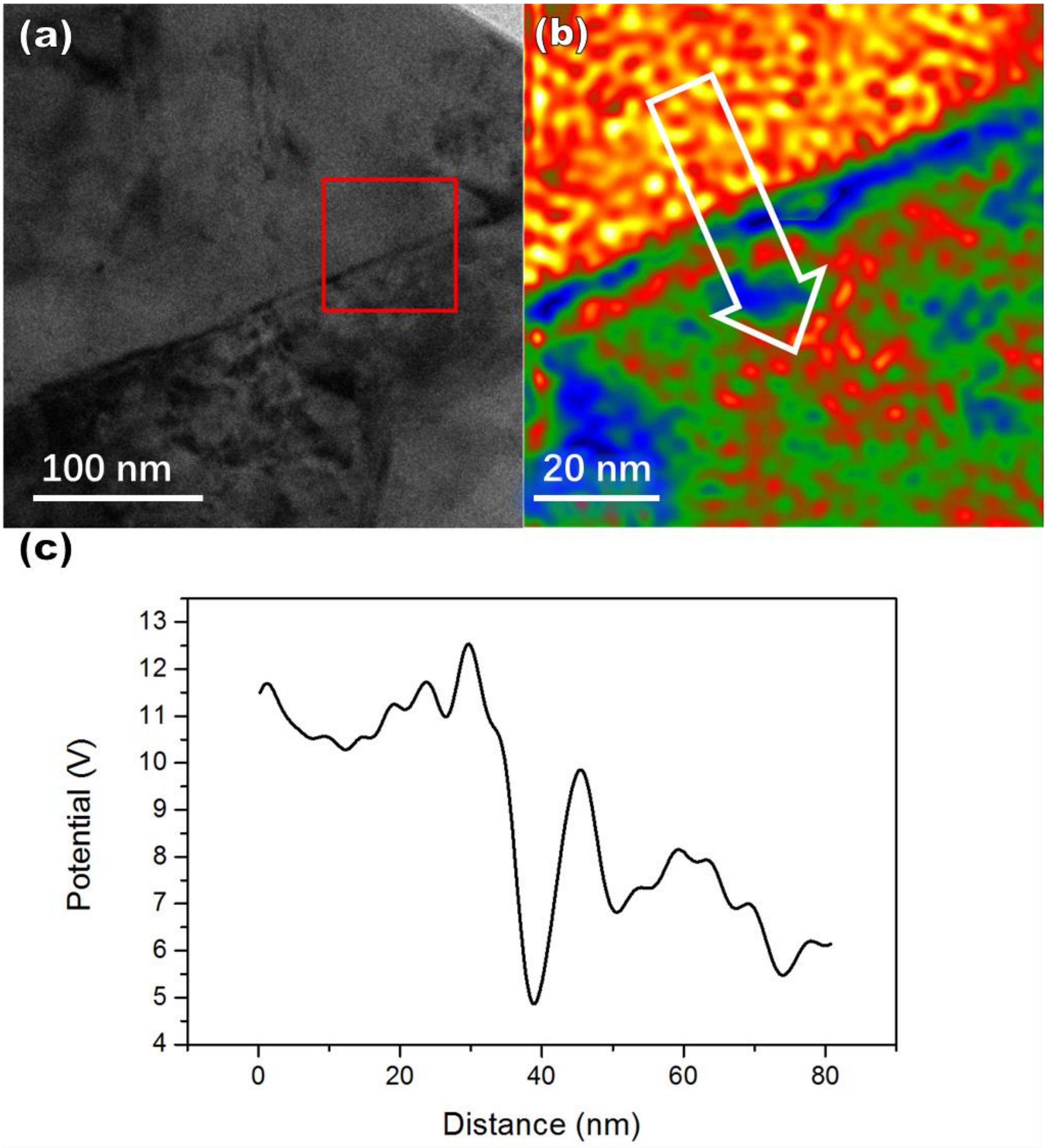

Figure 47 Potential mapping across a random boundary. (a) a TEM bright field imaging of a cross sectional CZTSe film prepared by FIB. (b) is a Potential mapping of the highlighted region in (a). (c) is a potential line profile that is highlighted in (b).

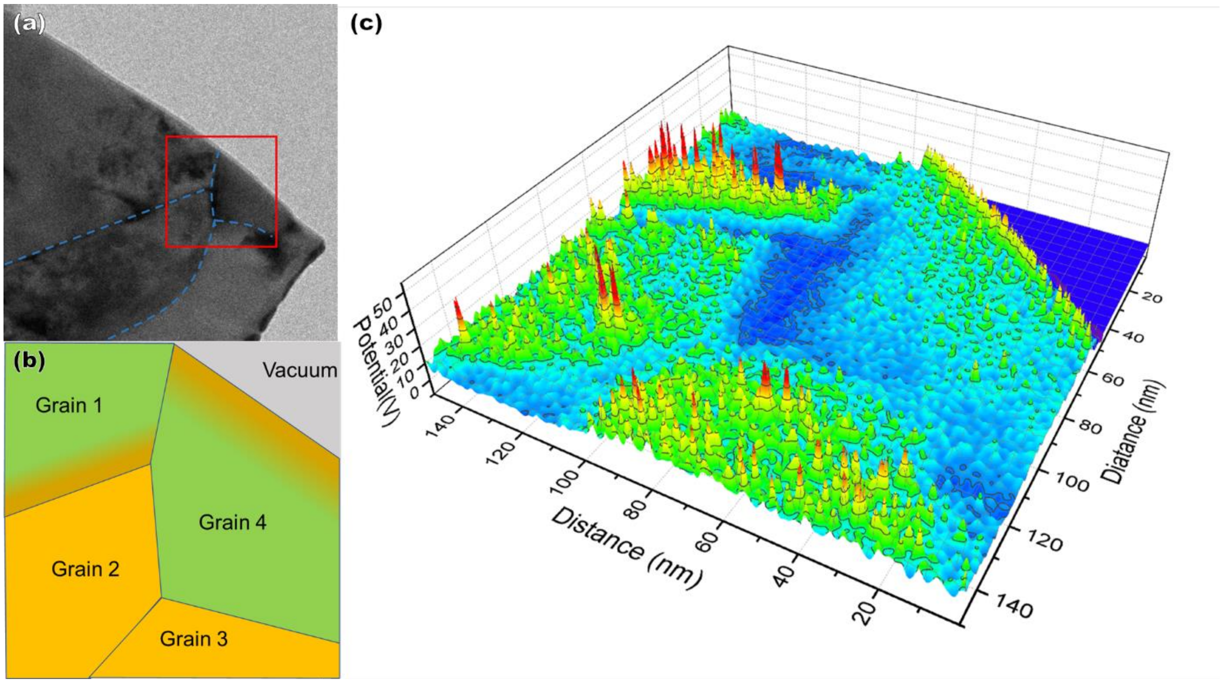

Figure 48 Potential mapping at a junction of four grains. (a) is a TEM bright field imaging of a different region from a FIB prepared CZTSe. (b) is a schematic of the highlighted region in (a). The yellow region indicates the presence of (112) surfaces. (c) is a 3D plot of the potential mapping in the same region.

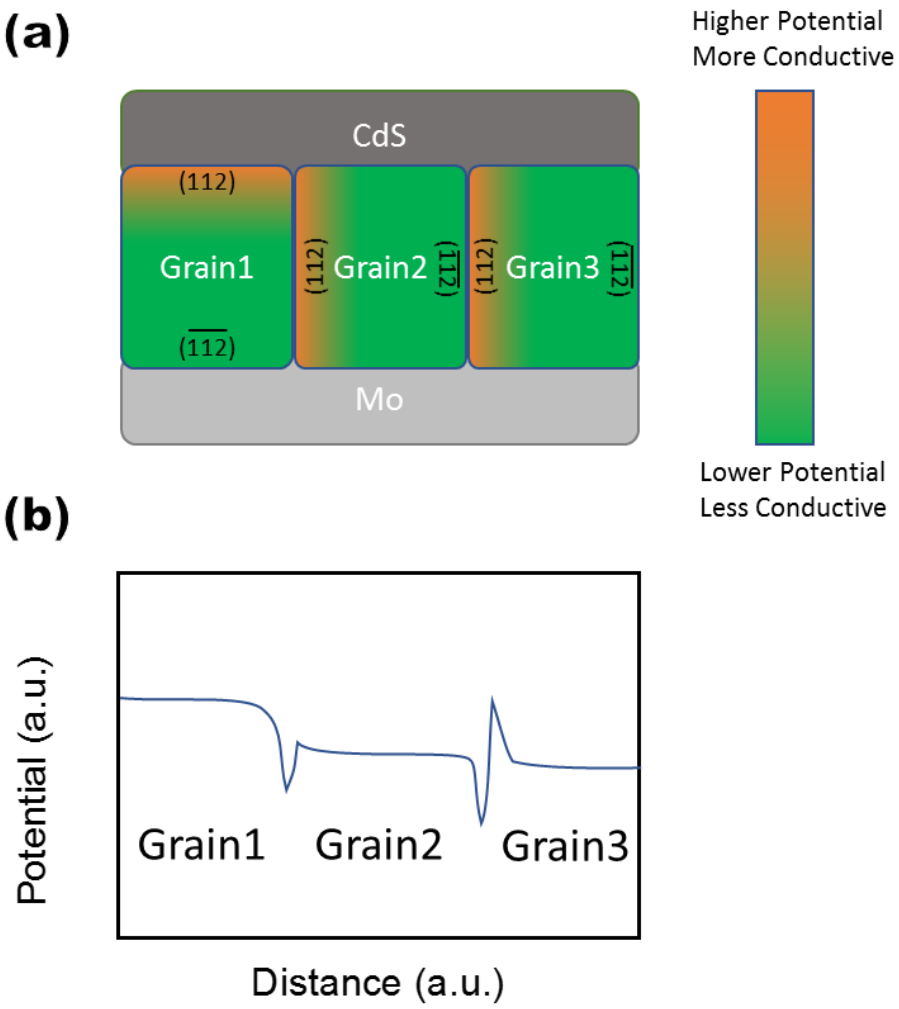

Figure 49 Schematics of the electrical model of CZTSe. (a) A schematic of a cross-sectional CZTSe device with 3 grains. Grain 1 has a (112) facet facing to CdS layer; Grain 2 and 3 have their (112) facet facing toward Grain 1. (b) is the potential change across the 3 grains.

5.4 Comparison between the GBs in CIGS and CZTSe

At the grain boundary core, these is a potential well between both CIGS and CZTSe. Compared to the simulation that has been done by Schmid[84], the potential well depth for a Σ 3 twin grain boundary, a Σ9 grain boundary and a random boundary is -0.2V, -0.68V and -2.3V. Compared to this result, the measured potential well at the GB between grain 2 and 3 in Figure 45 is about -0.6V; The potential well at the random GB in Figure 47 is about -2.5V. Both experimental results agree well with the case in CIGS, meaning that the grain boundary that exhibits lower symmetry involves a more distinct change in composition than that with a higher symmetry. The free energy of a Σ3 GB should be close to that of the perfect lattice because only the rotation of the bond between cations and selenium ion is present. While for the Σ9 GBs, at least some bonds across the GB must be distorted so that the free energy is increased. This is hence the driving force for the local change in composition at the GBs, and such effect will be maximized for a random boundary. In addition to the elemental reconstruction at the random GB core, the discontinuity of the GB may also contribute to the high potential barrier. Figure 50 shows a random boundary across two CZTSe grains. There is clearly a intergranular gap around 5 nm between the two grains, while general GB is around 5 Å. Hence for such types of grain boundaries, the potential barriers are mainly caused by the physical discontinuity across the grain. This intergranular boundary between the two grains can also introduce artifacts in the electron holography when it is on edge: The density of this gap is so low that the potential will drop down to close to vacuum across it. When the gap is inclined, such barrier will be insignificant because the low-density region will be overcome by the thickness of the specimen along the beam-direction (usually more than 100nm). The cause of this gap is likely due to the selenization process, where the selenization and sintering happen simultaneously. During the selenization process, the coexistence of Se vapor, Se liquid, $CuSe_2$ and the rest of the precursor nanoparticles can form a complex gas-liquid-solid reaction. At the initial stage of the growth of the CZTSe, they are imbedded within the precursor nanoparticles. As they grow larger and absorb nearby precursors, the gradually form (112) facets which has the lowest surface energies. When two of the grains make contact, they may rotate and align these boundaries if the mobilities of the grains are high. They can also grow together and form a larger grain which consists of twin boundaries and carbon impurities. When the metal precursor is depleted during the grain growth, a sintering process will then dominate the dynamic process during the selenization. During the sintering process, the grains will continue align their intergranular boundaries which is driven by the free energy at the interface. Therefore, after the selenization process, most of the random GBs are straight and show preferred orientation. When the selenization process is completed and sample is exposed to the atmosphere, the dangling bonds at these intergranular boundaries as well as the surfaces will then bond with H^+ and O^{2-} from the water and oxygen in the surrounding environment and stabilize. If there is a leaking during the selenization process, the precursor will form oxidize layer and the selenization process is interrupted because the oxygen will compete with selenium and the result will be a film with very fine CZTSe crystals. Therefore, with a significant amount of the grain boundaries being like the one in Figure 50, the electrical benign effect mainly come from the two adjacent grain interiors. Unlike CIGS that has symmetrical electrical properties at the GB, the electrical benign GBs in CZTSe usually only consists of one (112) surface which is preferred for the electron collection. The large gap at these intergranular boundaries will prevent the electrons on the other side from being collected by this region. Hence the efficiencies for these grain boundaries will be reduced by 50%. Furthermore, if the (112) surface is facing the CdS, the $(\overline{112})$ will face the bottom electrode, and the (112) surface will help separate electrons into the top electrode. On the other hand, if the (112) surface is facing the bottom electrode, these electrons will be trapped at the interface and never be collected by the top electrode. As a result, this asymmetrical surface electrical property may be the reason why the best lab cell efficiency of CZTSe is only about half of that of the CIGS solar cells.

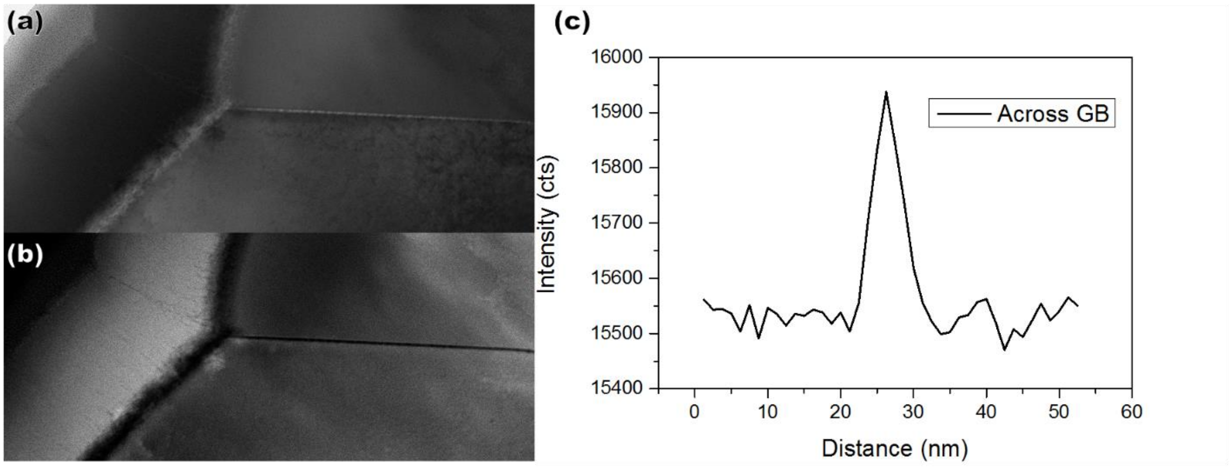

Figure 50 A intergranular boundary found between two grains. (a) STEM bright field and (b) HAADF imaging of a cross sectional CZTSe sample prepared by FIB. (c) is the line profile across the GB in (a).

Chapter 6

Development specimen holders for in-situ TEM characterizations

The design goal for these holders was to enable optical measurement and illumination in the first holder, and in-situ electrical measurement on standard TEM samples in the second holder. Additionally, since many of the materials of interest are in the form of cross-sectional single-crystal thin films, the holders must be double-tilt to allow accurate alignment of the zone axis for imaging. None of the commercially available holders match the capabilities specified for these designs.

6.1 TEM holder with optical fiber

The conventional CL holder that Gatan supplies is a single-tilt holder with two single-mode fiber optics and two mirrors to collect the optical signals. The holder has a tight space and there is no way to add electrical components. A commercial fiber-based optical holder was previously available from NanoFactory[157]. However, the probe's coarse motion is based on the concept of vibrational stick-slip motion and thus is very unpredictable.

For standard Cathodoluminescence (CL) spectroscopy, the light is emitted from the region that is irradiated by the electron beam. For simplification, it can be considered a point source. One of the biggest challenge is to collect as many of the emitted light as possible and couple them into the fiber optics. For the 1mm fiber optics that we choose for the holder, a maximum of 24.8 degree of acceptance angle can be achieved. This requires either the fiber optics being close enough to the sample, or coupled with additional optical elements. By using the lens system, the focal point can be adjusted on the sample so that the total amount of signal to be collected is maximized. The objective lens increases the acceptance angle for the fiber and helps capture the photons reflected by the mirror. The large diameter of the fiber optics can have a high acceptance angle. However, compared to using a thinner fiber, the light will be much less collimated when they enter a waveguide that has a larger cross sectional area, as they come from a much more diverted angle, resulting a loss of photon both during the transportation inside the waveguide. To avoid such type of signal loss, the total length of fiber optics should be minimized. Another factor that can impede the signal collection comes from the obstruction between the fibers, lenses, and patch cable connections. These loses of signal mainly come from the reflection when the light enters a media, which may be compensated by using optics that have anti-reflection coatings. But still, the best way to avoid such loss is to simplify the light path by reducing the total amount of the optical components or to project the collimated signal through free space. Another critical component for the CL spectroscopy is the spectrometer. There are three major categories of detectors that can be used, including photomultiplier tubes (PMTs), avalanche photodiodes (APDs), and charge-coupled devices (CCDs). APDs and PMTs are much more sensitive than CCDs, however they can only measure the intensity of all light hitting them at the same time, thus a turret of diffraction grating is needed to separate the light with different wavelength. This process increases the total form factor of the device and also significantly increases the acquisition time for a single spectrum. For CCDs, although the signal to noise ratio is smaller, the pixelated detector can acquire the entire spectrum at the same time. Hence for our application that require both portability and time resolution, an Ocean Optics QE Pro spectrometer was chosen for this application (Figure 51a).

By following the above criteria, we built an optical holder that has the following specifications.

The double-tilt stage can be adjusted by the push rod that is located on the back panel of the holder, and the material that we use to connect the push rod and the sample stage is a super elastic wire made of NiTi alloy (Nitinol). The Nitinol wire is light, passive, highly elastic, and resistive to abrasion.

The optical component is made with a 1mm fiber optics that is sealed inside a 3/32” brass tubing with Torr Seal epoxy. The front part of the tubing has a 3-80 thread for mounting additional optics such as a GRIN lens for coupling the light, an objective lens, and a mirror for better collection angle. On the back of the holder there is a knob to adjust the distance between the fiber optics and the sample stage. Such setup allows one to retract the fiber during the loading/unloading of the sample and adjust the focus of the light during the experiment to have the optimal signal strength.

Figure 51(a) shows the setup for a CL measurement. On the back of the holder we used a compact CCD spectrometer from Ocean Optics. The holder and the spectrometer are coupled with SMA connectors. We have tested Gd_2O_2S: Tb(P43), Y_2SiO_5: Ce(P47), and $Y+O_3$: Eu(P56) phosphor powder samples to test our CL signal. Figure 51(b) is the TEM image of P47 samples. Figure 10(c) shows the spectra of the three samples. The average size of these samples are around 3μm. And the acquisition time is 1s. The signal is strong enough for the powder of this size range, but is too weak for the actual TEM samples that are usually less than 100 nm. To improve the signal count, the holder should be coupled with PMT which has a better sensitivity. The acquisition time should be longer and the new design of mirror should be introduced to increase the collection angle.

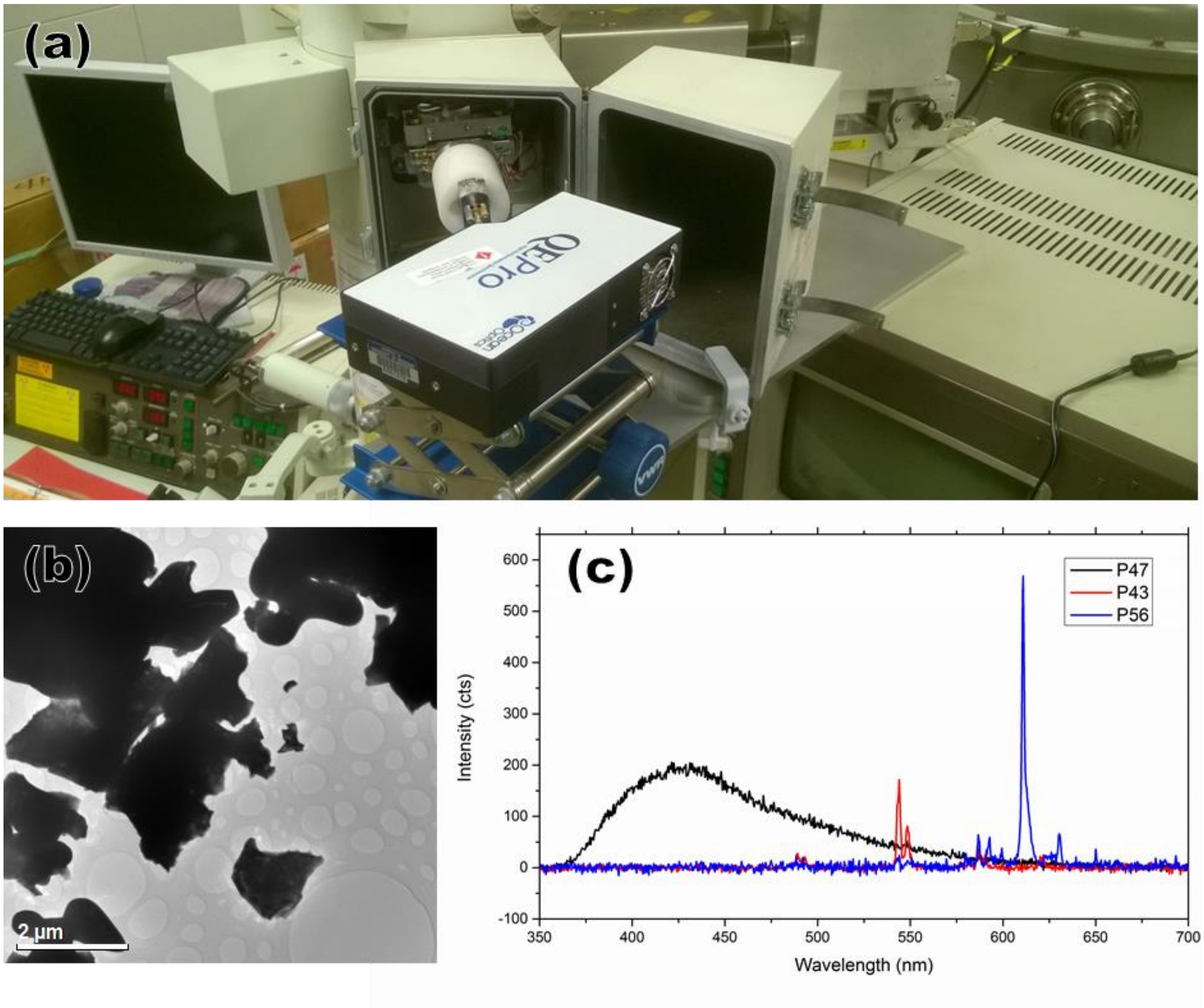

Figure 51 Setup of CL measurement using the optical holder. (a) The optical holder is connected to the JEOL JEM2010 and an ocean optics spectrometer for the cathodoluminecence measurement. (b) is the TEM image of the P47 powder. (c) is the CL spectra of P47, P43 and P46 measured by the optical holder.

In the preliminary stage of developing the holder, we have attempted to add optical illumination to the NanoFactory holder by adding two LED's on the tip of the holder (Figure 9b), which provided about 24 mcd of blue light. During the preliminary testing, we have found a few limitations of such setup: The sensitivity of electrical measurement is only at nA level, which is too low for in-situ electrical experiments for ceramic materials; the illumination intensity is too low; the wavelength of the illumination can't be adjusted; and the thermal drifting takes place when the LED heated up the local region of the holder. Hence a better design is needed to solve these problems. For the new design, the LED light source is replaced by the fiber optics. By using the fiber optics as the light source, the wavelength can be easily adjusted by coupling different light source to the holder. This enables the experiment that require measuring optical responses to different materials that have various band gap and absorption spectrum. The intensity of the light can also be adjusted by change the input power of the light source. In the case that requires strong illuminations, a high-power laser can be used. For the thermal drifting issue, the use of fiber optics removes the heat source during the generation of light from inside the holder to the outside environment so that there is no local heat source on the holder. In addition, the tip of the holder is entirely made of brass and aluminum that when compared with the metal cladded ceramic board, has much higher thermal conductivity. The heat that is caused by the localized illumination can be easily drained and the holder can become thermally stable in a short period of time. By using the fiber optics, the light can also be focused onto a specific region, which can have a more efficient illumination condition than LEDs. The use of fiber optics also provides the possibility of measuring PL/Raman signal by illuminating a laser with specific wavelength. By using a 1x2 fiber optic coupler and placing appropriate edge/notch filters between the spectrometer and the fiber, one can perfume in-situ Raman measurements, and electron-beam driven or photosensitive reactions can be characterized in real time.

The modifications to the NanoFactory holder and preliminary data can be found in Dr. Jokisaari's thesis[158]. The sample was a p-i-n GaAs solar cell and it shows a weak but notable response. And for the new design of the optical holder, we acquired the hologram around a ZnSe precipitate that is found in a CZTSe grain. The potential mapping was extracted with light on and off so that the potential change at the interface can be compared.

Figure 52 shows a setup for the illumination experiment. Instead of the spectrometer, the holder is coupled with a 50mw 405nm laser. The front side of the fiber optics is coated with a clear epoxy to diffuse the light for more uniform illumination. The sample stage is slightly tilted so that the fiber optics can illuminate the entire sample surface. Figure 31 shows the CIP mapping of a ZnSe particle imbedded inside the CZTSe. The potential change at the interface has dropped from 1.2 V to 0.6 V when the illumination is turned on, which indicates that the ZnSe/CZTSe interface has attracted the excited electron and holes and thus such defect serves as recombination sites to reduce the efficiency of the device. It is worth note that due to the incoherence of the coupling between the holder, the fiber optic patch cable, and the laser, the total energy loss is significant. A more powerful laser and better coupling is needed to increase the illumination current density. Besides the methods of increasing the source, one can also improve the illumination density by adding optics in the front in order to focus the light. The best way of doing that is to mount a gradient index (GRIN) optics. A GRIN optics is a type of optics that has a gradient refractive index alone the axial direction. The index is the highest in the center and it decreases as the radial distance increases. The ability of grin lenses to have flat surfaces drastically simplifies the design at the front of the fiber optics since it can be directly mounted on or fused to the front end of the optical fiber to produce collimated output. In the current version of our design, we used a collet to clamp a Φ=1mm GRIN lens on to the front end of the fiber optics assembly using the 3-80 thread on the exterior of the brass casing of the fiber. In combine with the front optics, the laser can be focus on different area of the sample by adjusting the knob located at the back of the holder. Such design doesn't require any adhesives or any permanent mounting methods such as fusing, so that the front optics can be taken off or swapped with other optics depending on the requirement of the illumination. For the CL spectroscopy use, the GRIN lens and its collet can be swapped with a polished aluminum mirror to increase the total collection angle of the CL signals.

In conclusion, our optical holder has several unique capabilities. The double-tilt stage is designed to fit the UHR pole-piece gap for JEOL microscopes. This allows the sample's zone axis to be aligned with the electron beam so that the atomically resolved imaging can be achieved when the in-situ experiment such as CL measurement or optical excitation is performed. In many optical holders, the fiber is placed very close to the sample so that the amount of light that is directly coupled to the fiber is maximized. Such design usually limits the double-tilt function of the holder. In our design, the optical lenses and mirror components increases the collection angle so that the fiber optics can be placed away from the double-tilt stage, the position of the fiber optic is also adjustable so that the signal can be maximized. Such design allows multiple characterization methods such as in-situ CL spectroscopy, Raman spectroscopy and holography under illumination.

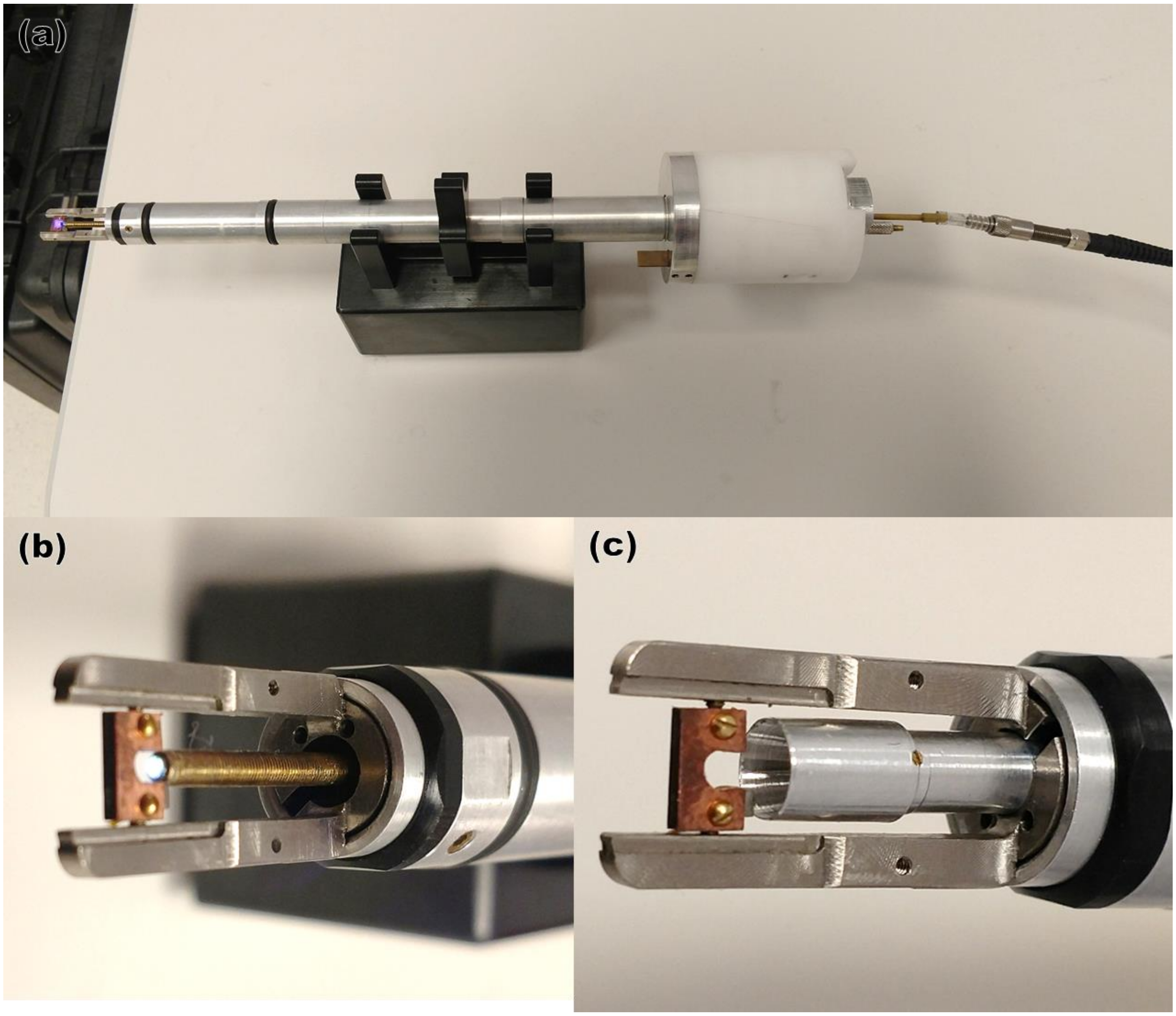

Figure 52 Optical holder with different attachments. (a) The optical holder is connected to a laser for the illumination measurement. (b) is a close look of the sample stage region with an illuminated fiber optics. (c) is a close look of the sample stage region with the fiber optics coupled with a polished aluminum mirror and an objective lens (mounted at the position with brass set screws on the mirror).

6.2 TEM holder with nanomanipulation and electrical measurement

The STM holder contains 3 separate subsystems, a mechanical coarse approach system, a piezo scanner for the fine motion/scanning, and a biasing/sensing component. The mechanical coarse motion uses a “wobble stick” design, where the entire tip assembly is assembled inside a brass tube that serves as a wobble stick. The wobble stick passes through an o-ring seal in the front part of the holder that serves as both a vacuum seal and a pivot point. The coarse tip motion is controlled by the mini linear stage that mounts on the back of the holder. When the stage moves to y+/z+ direction, the tip will be deflected towards y-/z- direction; when the stage moves along the x direction, the wobble stick will slide along the o-ring seal and move to the same direction. The differential adjuster screw allows has a 25 μm/rev resolution. When combined the reduction of the motion by having a pivot point at the o-ring seal, the coarse motion resolution can achieve 10 nm in y/z direction and 150 nm in x direction. Figure 53 shows the 3D design and the photo of the STM holder. As can be seen from Figure 53d, seven electrical wires, including five controlling the piezo tube and a twist pair of biasing/sensing cables pass through the 1/8" brass tubing, and are individually sealed at a specially designed feedthrough with vacuum epoxy. The feedthrough component is sealed by o-ring against the wobble stick so that the entire interior of the wobble stick is under vacuum when the holder is inserted into the TEM. Such back sealing mechanism ensures the best insulation across the seven wires and provide possibility of modifying and repairing the electronic components. The time required for the holder to be pumped down to 10^{-5} torr is also significantly shorter compared to the design that pumps the entire interior of the holder. However, since the wires that we used is not vacuum compatible, the holder will slowly degas if left in the ambient condition for too long. Thus we made a pump station to keep the holder in vacuum when not in use. At the current stage, the coarse motion is adjusted by the three differential screws on the linear stage.

The fine motion drive is a PZT piezo tube allowing sub-nanometer spatial resolutions for positioning and STM scanning within the TEM. The scan tube is mounted on an insulating base which connects it to the mechanical coarse motion system. The scan tube has four quartered electrodes and a center electrode, and can be driven by any available SPM scan controller. In this work, the scanner was connected to a Nanosis SPM scan control system from SPECS. This allows both fine positioning and STM scanning to be carried out. The scan tip is mounted in a copper cap, insulated from the piezo scan tube. The tip voltage and stage sense wires are carried by twisted pair shielded wire that is completely separated from the piezo drive electrics in order to prevent crosstalk between the scan and bias voltages. In order to effectively image single-crystal film specimens, a double-tilt holder is required. The tilt-stage is also actuated by a mechanical mechanism constructed in the same manner as the coarse-motion approach system. It should be noted that the majority 89 of in-situ holders are single-tilt, and therefore unsuitable or difficult to use for high resolution imaging of thin film specimens which constitute the majority of electronic materials samples. The double-tilt system is driven by a rod arrangement mounted to another spring-loaded micrometer at the rear of the specimen rod. The fine motion is controlled by a 1/8” by 1/2” PZT tube. The exterior gold contact has been divided into 4 quadrants. These quadrants correspond to bending the PZT tube to x+, x-. y+ and y- directions. The travel range of the fine motion is about 5 μm in y and z direction and 500 nm in x direction. Since the travel range of the fine motion is larger than the resolution of the coarse resolution, the tip can reach to any coordinate with the combination of the two systems. When performing the coarse motion by hands, however, some vibration is introduced to the tip through the screw. Such vibration makes the z-motion unstable because the resolution of the tip moving along x-y plane is about ten times higher than that along z-direction. One way to increase the stability of the coarse motion along z-direction is to increase the diameter of the knob. In doing so the torque that is applied to the screw is better controlled. Another way is to combine these knobs with piezo stacks. The combination of the micrometer and a piezo stack can achieve a much finer travel resolution in a larger scope. With the Thorlab PE4 adjuster, one can achieve 4mm travel of coarse motion using a 0.01” pitch leadscrew, and 15μm total travel of intermediate motion using the piezo stack. The introduction of a piezo stack fills the gap between the coarse and fine motion along the z-direction and hence makes the tip adjustment much easier.

The holder is compatible with the Nanosis SPM controller. When controlled by this controller, the holder can perform high sensitivity current measurement down to 10^{-11} A. Given such sensitivity, the holder is equipped with an automatic approaching mechanism that is controlled by the tunneling current feedback. When the tip is moved within the range of the piezo motor range, the system will expand the piezo tube when the tunneling current is low, meaning that the tip is still far from the sample; when the tunneling current exceeds a certain threshold, the piezo tube will contract to bring the current down, meaning that the tip has reached the sample.

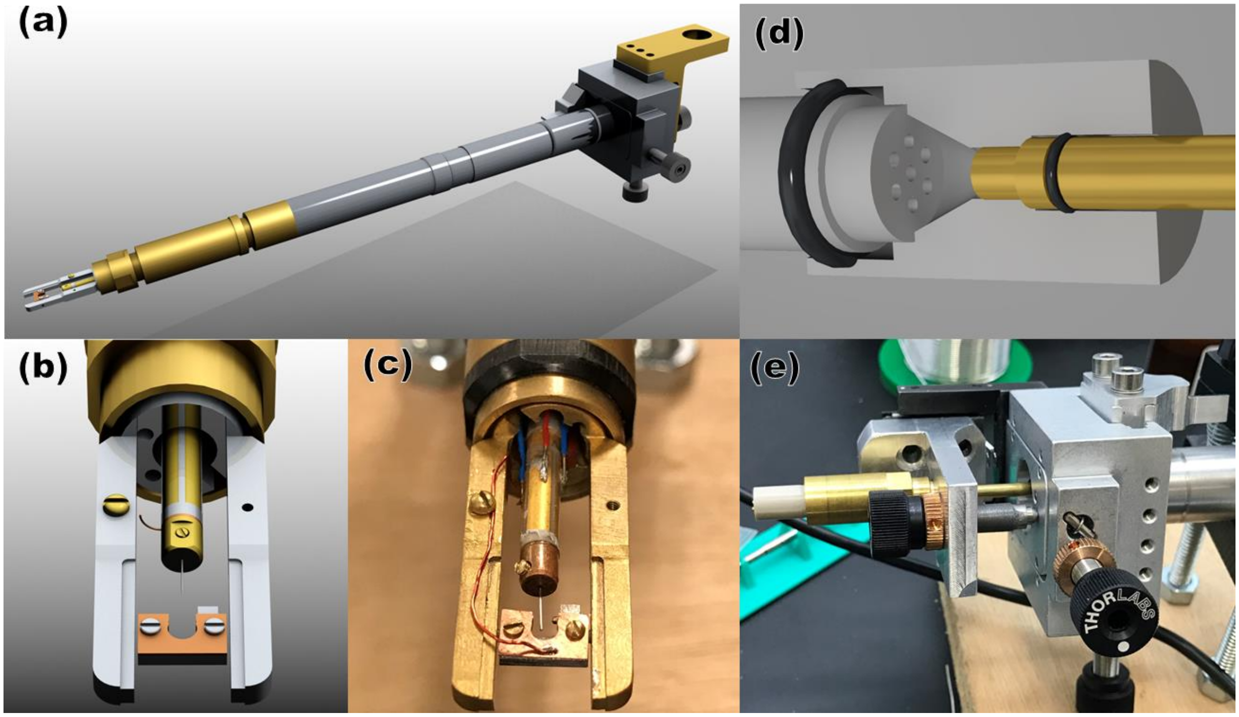

Figure 53 Design of the nano-manipulation holder. (a) The 3D modeling of the STM holder. (b) and (c) is the 3D modeling and the photo of a zoomed in sample stage region. (d) is the sealing design of the interior of the tip enclosure. (e) is the photo of the linear stage and the back of the tip enclosure.

Figure 54 shows an STM mapping over a notch on the edge of a Cu film. The topography information was calculated by recording the voltage applied to the piezo tube during the scanning process as the tip maintains the tunneling current of 100 nA. Using such technique, one can measure the film thickness by scanning the tip in the z direction, approach to the area of interest without the risk of touching/damaging the film, and perform current mapping on a smooth region by turning the feedback off.

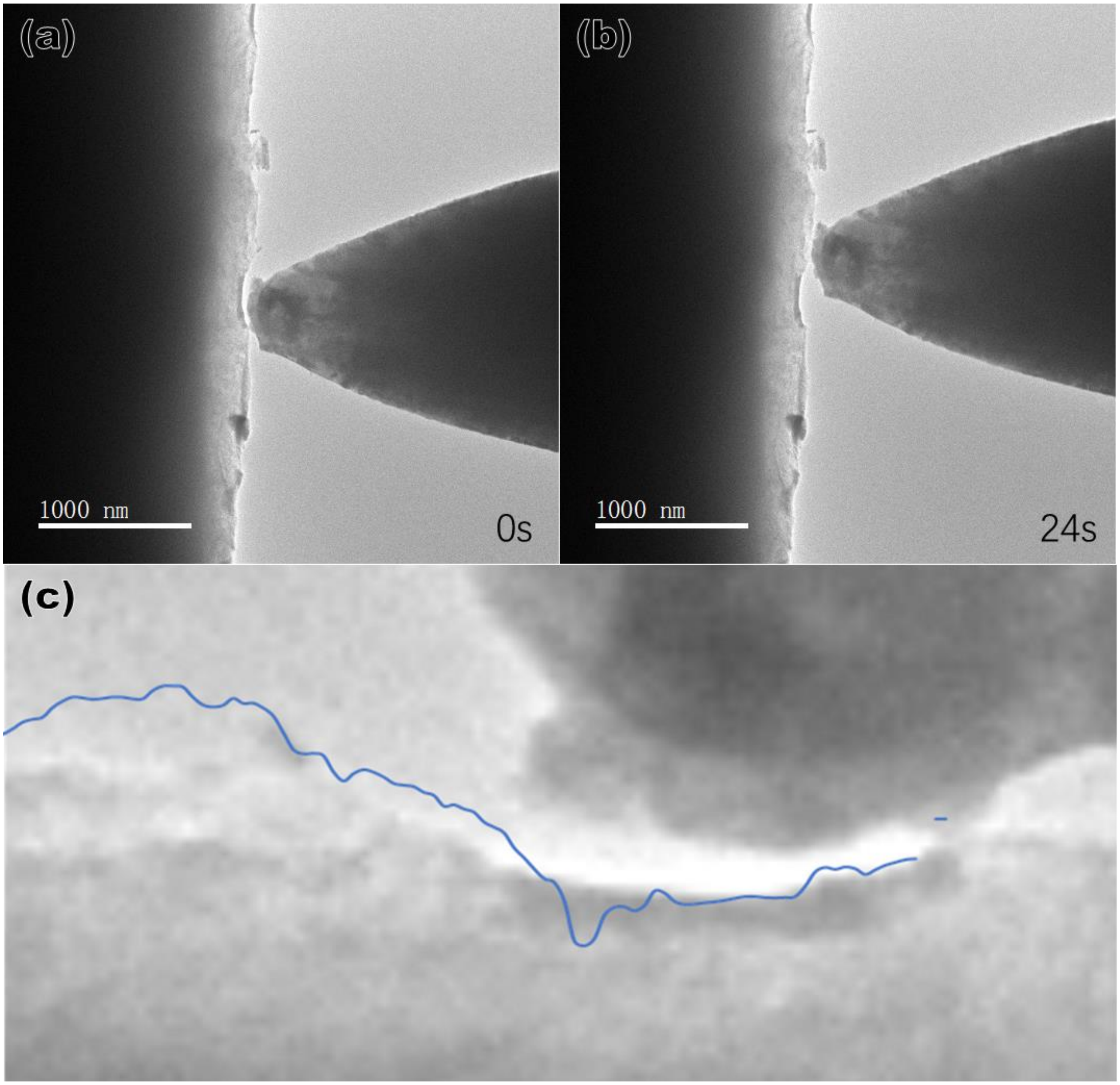

Figure 54 STM performed by the nano-manipulation holder. TEM imaging of the scanning tunneling mapping of a W tip on the edge of a Cu film at (a) t=0s and (b) t=24s. (c) is the topography from the scanning superimposed on the TEM image.

BIBLOGRAPHY

[1] M. I. Hoffert, K. Caldeira, A. K. Jain, E. F. Haites, L. D. Harvey, S. D. Potter*, et al.*, "Energy implications of future stabilization of atmospheric CO_2 content," *Nature,* vol. 395, pp. 881-884, 1998.

[2] O. Morton, "Solar energy: A new day dawning?: Silicon Valley sunrise," *Nature,* vol. 443, pp. 19-22, Sep 2006.

[3] V. Smil, *Energy in nature and society: general energetics of complex systems*. Cambridge, Mass.: The MIT Press, 2008.

[4] W. A. Hermann, "Quantifying global exergy resources," *Energy,* vol. 31, pp. 1685-1702, Sep 2006.

[5] "International Energy Outlook 2011," pp. U.S. Energy Information Administration, www.eia.gov/ieo/pdf/0484(2011).pdf, 2011.

[6] D. M. Chapin, C. S. Fuller, and G. L. Pearson, "A new silicon p-n junction photocell for converting solar radiation into electrical power," *Journal of Applied Physics,* vol. 25, pp. 676-677, 1954.

[7] D. A. Cusano, "CdTe solar cells and photovoltaic heterojunctions in II-VI compounds," *Solid-State Electronics,* vol. 6, pp. 217-232, 1963.

[8] K. Mitchell, A. L. Fahrenbruch, and R. H. Bube, "Structure and electrical properties of CdS and CdTe thick-films for solar cell applications," *Journal of Vacuum Science & Technology,* vol. 12, pp. 909-911, 1975.

[9] L. L. Kazmerski, F. R. White, and G. K. Morgan, "Thin-film $CuInSe_2$-CdS heterojunction solar cells," *Applied Physics Letters,* vol. 29, pp. 268-270, 1976.

[10] H. W. Schock and R. Noufi, "CIGS-based solar cells for the next millennium," *Progress in Photovoltaics,* vol. 8, pp. 151-160, Jan-Feb 2000.

[11] T. J. Coutts and C. R. Osterwald, "The quantum efficiency of CdS/$CuInSe_2$ and In_2O_3-Sn/InP solar-cells," *Solar Cells,* vol. 22, pp. 195-209, Nov 1987.

[12] A. Shah, P. Torres, R. Tscharner, N. Wyrsch, and H. Keppner, "Photovoltaic technology: The case for thin-film solar cells," *Science,* vol. 285, pp. 692-698, Jul 1999.

[13] I. Repins, M. A. Contreras, B. Egaas, C. DeHart, J. Scharf, C. L. Perkins*, et al.*, "19.9%-efficient ZnO/CdS/$CuInGaSe_2$ solar cell with 81.2% fill factor," *Progress in Photovoltaics,* vol. 16, pp. 235-239, May 2008.

[14] P. Jackson, D. Hariskos, E. Lotter, S. Paetel, R. Wuerz, R. Menner*, et al.*, "New world record efficiency for Cu(In,Ga)Se_2 thin-film solar cells beyond 20%," *Progress in Photovoltaics,* vol. 19, pp. 894-897, Nov 2011.

[15] M. J. Romero, H. Du, G. Teeter, Y. F. Yan, and M. M. Al-Jassim, "Comparative study of the luminescence and intrinsic point defects in the kesterite Cu_2ZnSnS_4 and chalcopyrite Cu(In,Ga)Se_2 thin films used in photovoltaic applications," *Physical Review B,* vol. 84, p. 165324, Oct 2011.

[16] "First Solar Reaches 4 Gigawatt Manufacturing Milestone," pp. News release, First Solar Inc., http://investor.firstsolar.com/releasedetail.cfm?ReleaseID=583448, 2011.

[17] "Japan’s Largest Solar Panel Factory Reaches Full Commercial Operations," pp. Press release, Solar Frontier K. K., http://www.solar-frontier.com/eng/news/2011/C002132.html, 2011.

[18] M. Tao, *Terawatt Solar Photovoltaics: Roadblocks and Opportunities*: Springer, 2014.

[19] C. S. Tao, J. Jiang, and M. Tao, "Natural resource limitations to terawatt-scale solar cells," *Solar Energy Materials and Solar Cells,* vol. 95, pp. 3176-3180, 2011.

[20] K. Ito and T. Nakazawa, "Electrical and optical-properties of stannite-type quaternary semiconductor thin films," *Japanese Journal of Applied Physics Part 1-Regular Papers Short Notes & Review Papers,* vol. 27, pp. 2094-2097, Nov 1988.

[21] B. R. Pamplin, "A systematic method of deriving new semiconducting compounds by structural analogy," *Journal of Physics and Chemistry of Solids,* vol. 25, pp. 675-684, 1964.

[22] A. Walsh, S. Chen, S. H. Wei, and X. G. Gong, "Kesterite Thin‐Film Solar Cells: Advances in Materials Modelling of Cu2ZnSnS4," *Advanced Energy Materials,* vol. 2, pp. 400-409, 2012.

[23] C. Catlow, Z. Guo, M. Miskufova, S. Shevlin, A. Smith, A. Sokol*, et al.*, "Advances in computational studies of energy materials," *Philosophical Transactions of the Royal Society of London A: Mathematical, Physical and Engineering Sciences,* vol. 368, pp. 3379-3456, 2010.

[24] C. Persson, "Electronic and optical properties of Cu 2 ZnSnS 4 and Cu 2 ZnSnSe 4," *Journal of Applied Physics,* vol. 107, p. 053710, 2010.

[25] J. Paier, R. Asahi, A. Nagoya, and G. Kresse, "Cu 2 ZnSnS 4 as a potential photovoltaic material: a hybrid Hartree-Fock density functional theory study," *Physical Review B,* vol. 79, p. 115126, 2009.

[26] A. Walsh, S. Chen, X. Gong, S. H. Wei, J. Ihm, and H. Cheong, "Crystal structure and defect reactions in the kesterite solar cell absorber Cu 2 ZnSnS 4 (CZTS): theoretical insights," in *AIP Conference Proceedings*, 2011, pp. 63-64.

[27] A. Walsh, S.-H. Wei, S. Chen, and X. Gong, "Design of quaternary chalcogenide photovoltaic absorbers through cation mutation," in *Photovoltaic Specialists Conference (PVSC), 2009 34th IEEE*, 2009, pp. 001875-001878.

[28] Y. Zhang, X. Sun, P. Zhang, X. Yuan, F. Huang, and W. Zhang, "Structural properties and quasiparticle band structures of Cu-based quaternary semiconductors for photovoltaic applications," *Journal of Applied Physics,* vol. 111, p. 063709, 2012.

[29] J. Raulot, C. Domain, and J. Guillemoles, "Ab initio investigation of potential indium and gallium free chalcopyrite compounds for photovoltaic application," *Journal of Physics and Chemistry of Solids,* vol. 66, pp. 2019-2023, 2005.

[30] A. Shavel, J. Arbiol, and A. Cabot, "Synthesis of Quaternary Chalcogenide Nanocrystals: Stannite Cu2Zn x Sn y Se1+ x+ 2 y," *Journal of the American Chemical Society,* vol. 132, pp. 4514-4515, 2010.

[31] I. Olekseyuk, L. Gulay, I. Dydchak, L. Piskach, O. Parasyuk, and O. Marchuk, "Single crystal preparation and crystal structure of the Cu 2 Zn/Cd, Hg/SnSe 4 compounds," *Journal of Alloys and Compounds,* vol. 340, pp. 141-145, 2002.

[32] S. Schorr, "The crystal structure of kesterite type compounds: A neutron and X-ray diffraction study," *Solar Energy Materials and Solar Cells,* vol. 95, pp. 1482-1488, 2011.

[33] H. Nozaki, T. Fukano, S. Ohta, Y. Seno, H. Katagiri, and K. Jimbo, "Crystal structure determination of solar cell materials: Cu 2 ZnSnS 4 thin films using X-ray anomalous dispersion," *Journal of Alloys and Compounds,* vol. 524, pp. 22-25, 2012.

[34] S. Siebentritt and S. Schorr, "Kesterites—a challenging material for solar cells," *Progress in Photovoltaics: Research and Applications,* vol. 20, pp. 512-519, 2012.

[35] S. Chen, X. Gong, A. Walsh, and S.-H. Wei, "Electronic structure and stability of quaternary chalcogenide semiconductors derived from cation cross-substitution of II-VI and I-III-VI 2 compounds," *Physical Review B,* vol. 79, p. 165211, 2009.

[36] D. B. Mitzi, O. Gunawan, T. K. Todorov, and D. A. R. Barkhouse, "Prospects and performance limitations for Cu–Zn–Sn–S–Se photovoltaic technology," *Philosophical Transactions of the Royal*

Society of London A: Mathematical, Physical and Engineering Sciences, vol. 371, p. 20110432, 2013.

[37] S. C. Riha, B. A. Parkinson, and A. L. Prieto, "Compositionally Tunable Cu2ZnSn (S1–x Se x) 4 Nanocrystals: Probing the Effect of Se-Inclusion in Mixed Chalcogenide Thin Films," *Journal of the American Chemical Society,* vol. 133, pp. 15272-15275, 2011.

[38] K.-J. Yang, D.-H. Son, S.-J. Sung, J.-H. Sim, Y.-I. Kim, S.-N. Park*, et al.*, "A band-gap-graded CZTSSe solar cell with 12.3% efficiency," *Journal of Materials Chemistry A,* vol. 4, pp. 10151-10158, 2016.

[39] K. Ito and T. Nakazawa, "Electrical and optical properties of stannite-type quaternary semiconductor thin films," *Japanese Journal of Applied Physics,* vol. 27, p. 2094, 1988.

[40] W. Wang, M. T. Winkler, O. Gunawan, T. Gokmen, T. K. Todorov, Y. Zhu*, et al.*, "Device Characteristics of CZTSSe Thin-Film Solar Cells with 12.6% Efficiency," *Advanced Energy Materials,* vol. 4, pp. n/a-n/a, 2014.

[41] K. Wang, O. Gunawan, T. Todorov, B. Shin, S. J. Chey, N. A. Bojarczuk*, et al.*, "Thermally evaporated Cu_2ZnSnS_4 solar cells," *Applied Physics Letters,* vol. 97, p. 143508, Oct 2010.

[42] A. Redinger, D. M. Berg, P. J. Dale, and S. Siebentritt, "The consequences of kesterite equilibria for efficient solar cells," *Journal of the American Chemical Society,* vol. 133, pp. 3320-3323, Mar 2011.

[43] K. Jimbo, R. Kimura, T. Kamimura, S. Yamada, W. S. Maw, H. Araki*, et al.*, "Cu_2ZnSnS_4-type thin film solar cells using abundant materials," *Thin Solid Films,* vol. 515, pp. 5997-5999, May 2007.

[44] H. Katagiri, K. Jimbo, S. Yamada, T. Kamimura, W. S. Maw, T. Fukano*, et al.*, "Enhanced conversion efficiencies of Cu_2ZnSnS_4-based thin film solar cells by using preferential etching technique," *Applied Physics Express,* vol. 1, p. 41201, Apr 2008.

[45] L. Grenet, S. Bernardi, D. Kohen, C. Lepoittevin, S. Noël, N. Karst*, et al.*, "$Cu_2ZnSn(S_{1-x}Se_x)_4$ based solar cell produced by selenization of vacuum deposited precursors," *Solar Energy Materials and Solar Cells,* vol. 101, pp. 11-14, 2012.

[46] T. K. Todorov, K. B. Reuter, and D. B. Mitzi, "High-efficiency solar cell with earth-abundant liquid-processed absorber," *Advanced Materials,* vol. 22, pp. E156-E159, May 2010.

[47] D. A. R. Barkhouse, O. Gunawan, T. Gokmen, T. K. Todorov, and D. B. Mitzi, "Device characteristics of a 10.1% hydrazine-processed $Cu_2ZnSn(Se,S)_4$ solar cell," *Progress in Photovoltaics,* vol. 20, pp. 6-11, Jan 2012.

[48] S. Bag, O. Gunawan, T. Gokmen, Y. Zhu, T. K. Todorov, and D. B. Mitzi, "Low band gap liquid-processed CZTSe solar cell with 10.1% efficiency," *Energy & Environmental Science,* vol. 5, pp. 7060-7065, May 2012.

[49] T. K. Todorov, J. Tang, S. Bag, O. Gunawan, T. Gokmen, Y. Zhu*, et al.*, "Beyond 11% efficiency: Characteristics of state-of-the-art $Cu_2ZnSn(S,Se)_4$ solar cells," *Advanced Energy Materials,* p. doi: 10.1002/aenm.201200348, 2012.

[50] G. M. Ford, Q. J. Guo, R. Agrawal, and H. W. Hillhouse, "Earth abundant element $Cu_2Zn(Sn_{1-x}Ge_x)S_4$ nanocrystals for tunable band gap solar cells: 6.8% efficient device fabrication," *Chemistry of Materials,* vol. 23, pp. 2626-2629, May 2011.

[51] Q. Guo, G. M. Ford, W.-C. Yang, C. J. Hages, H. W. Hillhouse, and R. Agrawal, "Enhancing the performance of CZTSSe solar cells with Ge alloying," *Solar Energy Materials and Solar Cells,* vol. 105, pp. 132-136, 2012.

[52] Q. Guo, G. M. Ford, W. C. Yang, B. C. Walker, E. A. Stach, H. W. Hillhouse*, et al.*, "Fabrication of 7.2% efficient CZTSSe solar cells using CZTS nanocrystals," *Journal of the American Chemical Society,* vol. 132, pp. 17384-17386, Dec 2010.

[53] A. Ennaoui, M. Lux-Steiner, A. Weber, D. Abou-Ras, I. Kotschau, H. W. Schock*, et al.*, "Cu_2ZnSnS_4 thin film solar cells from electroplated precursors: Novel low-cost perspective," *Thin Solid Films,* vol. 517, pp. 2511-2514, Feb 2009.

[54] M. Ganchev, J. Iljina, L. Kaupmees, T. Raadik, O. Volobujeva, A. Mere*, et al.*, "Phase composition of selenized $Cu_2ZnSnSe_4$ thin films determined by X-ray diffraction and Raman spectroscopy," *Thin Solid Films,* vol. 519, pp. 7394-7398, Aug 2011.

[55] N. Bärsch, J. Jakobi, S. Weiler, and S. Barcikowski, "Pure colloidal metal and ceramic nanoparticles from high-power picosecond laser ablation in water and acetone," *Nanotechnology,* vol. 20, p. 445603, 2009.

[56] J. H. Dickerson and A. R. Boccaccini, *Electrophoretic Deposition of Nanomaterials*. New York: Springer, 2012.

[57] M. T. Winkler, W. Wang, O. Gunawan, H. J. Hovel, T. K. Todorov, and D. B. Mitzi, "Optical designs that improve the efficiency of $Cu_2ZnSn(S, Se)_4$ solar cells," *Energy & Environmental Science,* vol. 7, pp. 1029-1036, 2014.

[58] A. Redinger, K. Hoenes, X. Fontane, V. Izquierdo-Roca, E. Saucedo, N. Valle*, et al.*, "Detection of a ZnSe secondary phase in coevaporated $Cu_2ZnSnSe_4$ thin films," *Applied Physics Letters,* vol. 98, p. 101907, Mar 7 2011.

[59] B. Shin, O. Gunawan, Y. Zhu, N. A. Bojarczuk, S. J. Chey, and S. Guha, "Thin film solar cell with 8.4% power conversion efficiency using an earth-abundant Cu_2ZnSnS_4 absorber," *Progress in Photovoltaics,* vol. 21, pp. 72-76, Jan 2013.

[60] G. Wang, W. Zhao, Y. Cui, Q. Tian, S. Gao, L. Huang*, et al.*, "Fabrication of a $Cu_2ZnSn(S,Se)_4$ Photovoltaic Device by a Low-Toxicity Ethanol Solution Process," *ACS Appl Mater Interfaces,* vol. 5, pp. 10042-7, Oct 23 2013.

[61] B. K. Michael, Z. Shuyi, D. Yingwen, W. Hongjie, F. Minghao, Z. Kui*, et al.*, "Reversible precipitation/dissolution of precious-metal clusters in perovskite-based catalyst materials: Bulk versus surface re-dispersion," *Journal of Catalysis,* vol. 293, pp. 145-148, 2012.

[62] I. D. Olekseyuk, I. V. Dudchak, and L. V. Piskach, "Phase equilibria in the Cu_2S-ZnS-SnS_2 system," *Journal of Alloys and Compounds,* vol. 368, pp. 135-143, Apr 2004.

[63] I. V. Dudchak and L. V. Piskach, "Phase equilibria in the Cu_2SnSe_3-$SnSe_2$-ZnSe system," *Journal of Alloys and Compounds,* vol. 351, pp. 145-150, Mar 10 2003.

[64] A. Nagoya, R. Asahi, R. Wahl, and G. Kresse, "Defect formation and phase stability of Cu_2ZnSnS_4 photovoltaic material," *Physical Review B,* vol. 81, p. 113202, Mar 2010.

[65] J. J. Scragg, T. Ericson, T. Kubart, M. Edoff, and C. Platzer-Bjorkman, "Chemical insights into the instability of Cu_2ZnSnS_4 films during annealing," *Chemistry of Materials,* vol. 23, pp. 4625-4633, Oct 2011.

[66] A. R. Jeong, W. Jo, S. Jung, J. Gwak, and J. H. Yun, "Enhanced exciton separation through negative energy band bending at grain boundaries of $Cu_2ZnSnSe_4$ thin-films," *Applied Physics Letters,* vol. 99, p. 82103, Aug 2011.

[67] J. W. Li, D. B. Mitzi, and V. B. Shenoy, "Structure and electronic properties of grain boundaries in earth-abundant photovoltaic absorber $Cu_2ZnSnSe_4$," *Acs Nano,* vol. 5, pp. 8613-8619, Nov 2011.

[68] A. Walsh, S. Y. Chen, S. H. Wei, and X. G. Gong, "Kesterite thin-film solar cells: Advances in materials modelling of Cu_2ZnSnS_4," *Advanced Energy Materials,* vol. 2, pp. 400-409, Apr 2012.

[69] T. Maeda, S. Nakamura, and T. Wada, "First-principles calculations of vacancy formation in In-free photovoltaic semiconductor $Cu_2ZnSnSe_4$," *Thin Solid Films,* vol. 519, pp. 7513-7516, Aug 2011.

[70] J. B. Li, V. Chawla, and B. M. Clemens, "Investigating the role of grain boundaries in CZTS and CZTSSe thin film solar cells with Scanning Probe Microscopy," *Advanced Materials,* vol. 24, pp. 720-723, Feb 2012.

[71] J. M. Raulot, C. Domain, and J. F. Guillemoles, "Ab initio investigation of potential indium and gallium free chalcopyrite compounds for photovoltaic application," *Journal of Physics and Chemistry of Solids,* vol. 66, pp. 2019-2023, Nov 2005.

[72] S. Y. Chen, X. G. Gong, A. Walsh, and S. H. Wei, "Defect physics of the kesterite thin-film solar cell absorber Cu_2ZnSnS_4," *Applied Physics Letters,* vol. 96, p. 21902, Jan 2010.

[73] S. Y. Chen, J. H. Yang, X. G. Gong, A. Walsh, and S. H. Wei, "Intrinsic point defects and complexes in the quaternary kesterite semiconductor Cu_2ZnSnS_4," *Physical Review B,* vol. 81, p. 245204, Jun 2010.

[74] Q. Guo, G. M. Ford, W.-C. Yang, C. J. Hages, H. W. Hillhouse, and R. Agrawal, "Enhancing the performance of CZTSSe solar cells with Ge alloying," *Solar Energy Materials and Solar Cells,* vol. 105, pp. 132-136, 2012.

[75] V. Chawla and B. Clemens, "Effect of composition on high efficiency CZTSSe devices fabricated using co-sputtering of compound targets," in *Photovoltaic Specialists Conference (PVSC), 2012 38th IEEE*, 2012, pp. 002990-002992.

[76] G. Brammertz, M. Buffiere, S. Oueslati, H. ElAnzeery, K. B. Messaoud, S. Sahayaraj*, et al.*, "Characterization of defects in 9.7% efficient $Cu_2ZnSnSe_4$-CdS-ZnO solar cells," *Applied Physics Letters,* vol. 103, p. 163904, 2013.

[77] I. Repins, C. Beall, N. Vora, C. DeHart, D. Kuciauskas, P. Dippo*, et al.*, "Co-evaporated $Cu_2ZnSnSe_4$ films and devices," *Solar Energy Materials and Solar Cells,* vol. 101, pp. 154-159, 2012.

[78] D. B. Williams and C. B. Carter, "The transmission electron microscope," in *Transmission electron microscopy*, ed: Springer, 1996, pp. 3-17.

[79] L. A. Giannuzzi and F. A. Stevie, "A review of focused ion beam milling techniques for TEM specimen preparation," *Micron,* vol. 30, pp. 197-204, 1999.

[80] L. Li, "Atomic-scale Polarization Structures and Domain Dynamics in BiFeO3 Thin Films," 2016.

[81] P. D. Nellist and S. J. Pennycook, *Scanning Transmission Electron Microscopy: Imaging and Analysis*: Springer, 2011.

[82] G. Möllenstedt and H. Düker, "Beobachtungen und messungen an biprisma-interferenzen mit elektronenwellen," *Zeitschrift für Physik,* vol. 145, pp. 377-397, 1956.

[83] M. Lehmann and H. Lichte, "Tutorial on off-axis electron holography," *Microscopy and Microanalysis,* vol. 8, pp. 447-466, 2002.

[84] S. S. Schmidt, "Microscopic properties of grain boundaries in Cu (In, Ga) Se2 and CuInS2 thin-film solar cells studied by transmission electron microscopy," 2011.

[85] D. Gabor, "A new microscopic principle," *Nature,* vol. 161, pp. 777-778, 1948.

[86] G. Wentzel, "Eine verallgemeinerung der quantenbedingungen für die zwecke der wellenmechanik," *Zeitschrift für Physik A Hadrons and Nuclei,* vol. 38, pp. 518-529, 1926.

[87] A. Weickenmeier and H. Kohl, "Computation of absorptive form factors for high-energy electron diffraction," *Acta Crystallographica Section A: Foundations of Crystallography,* vol. 47, pp. 590-597, 1991.

[88] J. W. S. del Busto, "Study of solar cells by electron holography," 2012.

[89] P. Formanek and E. Bugiel, "On specimen tilt for electron holography of semiconductor devices," *Ultramicroscopy,* vol. 106, pp. 292-300, 2006.

[90] D. A. Long and D. Long, *Raman spectroscopy* vol. 206: McGraw-Hill New York, 1977.

[91] A. N. Chiaramonti, L. J. Thompson, W. F. Egelhoff, B. C. Kabius, and A. K. Petford-Long, "In situ TEM studies of local transport and structure in nanoscale multilayer films," *Ultramicroscopy,* vol. 108, pp. 1529-1535, 11// 2008.

[92] O. L. Warren, Z. Shan, S. A. S. Asif, E. A. Stach, J. W. Morris Jr, and A. M. Minor, "In situ nanoindentation in the TEM," *Materials Today,* vol. 10, pp. 59-60, 4// 2007.

[93] S. J. Kim, A. Kargar, D. Wang, G. W. Graham, and X. Pan, "Lithiation of Rutile TiO2-Coated Si NWs Observed by in Situ TEM," *Chemistry of Materials,* vol. 27, pp. 6929-6933, 2015.

[94] H. Olin, F. Althoff, and K. Svensson, "Micropositioning device," ed: Google Patents, 2004.

[95] P. Patil, D. Phase, S. Kulkarni, S. Ghaisas, S. Kulkarni, S. Kanetkar*, et al.*, "Pulsed-laser–induced reactive quenching at liquid-solid interface: Aqueous oxidation of iron," *Physical review letters,* vol. 58, p. 238, 1987.

[96] H. Hamaker, "Formation of a deposit by electrophoresis," *Transactions of the Faraday Society,* vol. 35, pp. 279-287, 1940.

[97] T. Ishihara, K. Shimose, T. Kudo, H. Nishiguchi, T. Akbay, and Y. Takita, "Preparation of Yttria ‐ Stabilized Zirconia Thin Films on Strontium ‐ Doped LaMnO3 Cathode Substrates via Electrophoretic Deposition for Solid Oxide Fuel Cells," *Journal of the American Ceramic Society,* vol. 83, pp. 1921-1927, 2000.

[98] F. Chen and M. Liu, "Preparation of yttria-stabilized zirconia (YSZ) films on La 0.85 Sr 0.15 MnO 3 (LSM) and LSM–YSZ substrates using an electrophoretic deposition (EPD) process," *Journal of the European Ceramic Society,* vol. 21, pp. 127-134, 2001.

[99] J. H. Scofield, A. Duda, D. Albin, B. L. Ballard, and P. K. Predecki, "Sputtered molybdenum bilayer back contact for copper indium diselenide-based polycrystalline thin-film solar cells," *Thin Solid Films,* vol. 260, pp. 26-31, 1995/05/01 1995.

[100] G. Zoppi, N. S. Beattie, J. D. Major, R. W. Miles, and I. Forbes, "Electrical, morphological and structural properties of RF magnetron sputtered Mo thin films for application in thin film photovoltaic solar cells," *Journal of Materials Science,* vol. 46, pp. 4913-4921, 2011.

[101] X. Dai, A. Zhou, L. Feng, Y. Wang, J. Xu, and J. Li, "Molybdenum thin films with low resistivity and superior adhesion deposited by radio-frequency magnetron sputtering at elevated temperature," *Thin Solid Films,* vol. 567, pp. 64-71, 9/30/ 2014.

[102] S. A. Pethe, E. Takahashi, A. Kaul, and N. G. Dhere, "Effect of sputtering process parameters on film properties of molybdenum back contact," *Solar Energy Materials and Solar Cells,* vol. 100, pp. 1-5, 5// 2012.

[103] P. M. P. Salomé, J. Malaquias, P. A. Fernandes, and A. F. d. Cunha, "Mo bilayer for thin film photovoltaics revisited," *Journal of Physics D: Applied Physics,* vol. 43, p. 345501, 2010.

[104] H.-M. Wu, S.-C. Liang, Y.-L. Lin, C.-Y. Ni, H.-Y. Bor, D.-C. Tsai*, et al.*, "Structure and electrical properties of Mo back contact for Cu(In, Ga)Se2 solar cells," *Vacuum,* vol. 86, pp. 1916-1919, 7/20/ 2012.

[105] C.-Y. Su, K.-H. Liao, C.-T. Pan, and P.-W. Peng, "The effect of deposition parameters and post treatment on the electrical properties of Mo thin films," *Thin Solid Films,* vol. 520, pp. 5936-5939, 7/1/ 2012.

[106] Z.-H. Li, E.-S. Cho, and S. J. Kwon, "Molybdenum thin film deposited by in-line DC magnetron sputtering as a back contact for Cu(In,Ga)Se2 solar cells," *Applied Surface Science,* vol. 257, pp. 9682-9688, 9/1/ 2011.

[107] M. Jubault, L. Ribeaucourt, E. Chassaing, G. Renou, D. Lincot, and F. Donsanti, "Optimization of molybdenum thin films for electrodeposited CIGS solar cells," *Solar Energy Materials and Solar Cells,* vol. 95, Supplement 1, pp. S26-S31, 5// 2011.

[108] K. Orgassa, H. W. Schock, and J. H. Werner, "Alternative back contact materials for thin film Cu(In,Ga)Se2 solar cells," *Thin Solid Films,* vol. 431–432, pp. 387-391, 5/1/ 2003.

[109] J. J. Scragg, T. Kubart, J. T. Wätjen, T. Ericson, M. K. Linnarsson, and C. Platzer-Björkman, "Effects of back contact instability on Cu2ZnSnS4 devices and processes," *Chemistry of Materials,* vol. 25, pp. 3162-3171, 2013.

[110] J. J. Scragg, P. J. Dale, D. Colombara, and L. M. Peter, "Thermodynamic Aspects of the Synthesis of Thin-Film Materials for Solar Cells," *ChemPhysChem,* vol. 13, pp. 3035-3046, 2012.

[111] C. Shi, X. Liu, and R. Chuai, "Piezoresistive sensitivity, linearity and resistance time drift of polysilicon nanofilms with different deposition temperatures," *Sensors,* vol. 9, pp. 1141-1166, 2009.

[112] S. B. Zhang, S.-H. Wei, and A. Zunger, "Stabilization of ternary compounds via ordered arrays of defect pairs," *Physical Review Letters,* vol. 78, pp. 4059-4062, 1997.

[113] S. B. Zhang, S. H. Wei, A. Zunger, and H. Katayama-Yoshida, "Defect physics of the $CuInSe_2$ chalcopyrite semiconductor," *Physical Review B,* vol. 57, pp. 9642-9656, Apr 1998.

[114] S. H. Wei, S. B. Zhang, and A. Zunger, "Effects of Ga addition to $CuInSe_2$ on its electronic, structural, and defect properties," *Applied Physics Letters,* vol. 72, pp. 3199-3201, Jun 1998.

[115] S. H. Wei and S. B. Zhang, "Defect properties of $CuInSe_2$ and $CuGaSe_2$," *Journal of Physics and Chemistry of Solids,* vol. 66, pp. 1994-1999, Nov 2005.

[116] C. Persson and A. Zunger, "Anomalous grain boundary physics in polycrystalline $CuInSe_2$: The existence of a hole barrier," *Physical Review Letters,* vol. 91, p. 266401, Dec 2003.

[117] Y. Yan, R. Noufi, and M. M. Al-Jassim, "Grain-boundary physics in polycrystalline $CuInSe_2$ revisited: Experiment and theory," *Physical Review Letters,* vol. 96, p. 205501, May 2006.

[118] Y. Yan, C. S. Jiang, R. Noufi, S. H. Wei, H. R. Moutinho, and M. M. Al-Jassim, "Electrically benign behavior of grain boundaries in polycrystalline $CuInSe_2$ films," *Physical Review Letters,* vol. 99, p. 235504, Dec 2007.

[119] S. H. Wei, S. B. Zhang, and A. Zunger, "Effects of Na on the electrical and structural properties of $CuInSe_2$," *Journal of Applied Physics,* vol. 85, pp. 7214-7218, May 1999.

[120] S. Siebentritt, S. Sadewasser, M. Wimmer, C. Leendertz, T. Eisenbarth, and M. C. Lux-Steiner, "Evidence for a neutral grain-boundary barrier in chalcopyrites," *Physical Review Letters,* vol. 97, p. 146601, Oct 2006.

[121] C. S. Jiang, R. Noufi, J. A. AbuShama, K. Ramanathan, H. R. Moutinho, J. Pankow*, et al.*, "Local built-in potential on grain boundary of $Cu(In,Ga)Se_2$ thin films," *Applied Physics Letters,* vol. 84, pp. 3477-3479, May 2004.

[122] C. S. Jiang, R. Noufi, K. Ramanathan, J. A. AbuShama, H. R. Moutinho, and M. M. Al-Jassim, "Does the local built-in potential on grain boundaries of $Cu(In,Ga)Se_2$ thin films benefit photovoltaic performance of the device?," *Applied Physics Letters,* vol. 85, pp. 2625-2627, Sep 2004.

[123] S. Sadewasser, T. Glatzel, S. Schuler, S. Nishiwaki, R. Kaigawa, and M. C. Lux-Steiner, "Kelvin probe force microscopy for the nano scale characterization of chalcopyrite solar cell materials and devices," *Thin Solid Films,* vol. 431, pp. 257-261, May 2003.

[124] M. J. Hetzer, Y. M. Strzhemechny, M. Gao, M. A. Contreras, A. Zunger, and L. J. Brillson, "Direct observation of copper depletion and potential changes at copper indium gallium diselenide grain boundaries," *Applied Physics Letters,* vol. 86, p. 162105, Apr 2005.

[125] H. Monig, Y. Smith, R. Caballero, C. A. Kaufmann, I. Lauermann, M. C. Lux-Steiner*, et al.*, "Direct evidence for a reduced density of deep level defects at grain boundaries of $Cu(In, Ga)Se_2$ thin films," *Physical Review Letters,* vol. 105, p. 116802, Sep 2010.

[126] U. Rau, K. Taretto, and S. Siebentritt, "Grain boundaries in $Cu(In, Ga)(Se, S)_2$ thin-film solar cells," *Applied Physics a-Materials Science & Processing,* vol. 96, pp. 221-234, Jul 2009.

[127] K. Taretto, U. Rau, and J. H. Werner, "Numerical simulation of grain boundary effects in $Cu(In,Ga)Se_2$ thin-film solar cells," *Thin Solid Films,* vol. 480, pp. 8-12, Jun 2005.

[128] M. Gloeckler, J. R. Sites, and W. K. Metzger, "Grain-boundary recombination in $Cu(In,Ga)Se_2$ solar cells," *Journal of Applied Physics,* vol. 98, p. 113704, Dec 2005.

[129] A. Nateprov, V. C. Kravtsov, G. Gurieva, and S. Schorr, "Single crystal X-ray structure investigation of Cu2ZnSnSe4," *Surface Engineering and Applied Electrochemistry,* vol. 49, pp. 423-426, 2013.

[130] S. Schorr, H.-J. Hoebler, and M. Tovar, "A neutron diffraction study of the stannite-kesterite solid solution series," *European Journal of Mineralogy,* vol. 19, pp. 65-73, 2007.

[131] M. Y. Valakh, O. Kolomys, S. Ponomaryov, V. Yukhymchuk, I. Babichuk, V. Izquierdo ‐ Roca*, et al.*, "Raman scattering and disorder effect in Cu_2ZnSnS_4," *physica status solidi (RRL)-Rapid Research Letters,* vol. 7, pp. 258-261, 2013.

[132] S. Bag, O. Gunawan, T. Gokmen, Y. Zhu, T. K. Todorov, and D. B. Mitzi, "Low band gap liquid-processed CZTSe solar cell with 10.1% efficiency," *Energy Environ. Sci.,* vol. 5, pp. 7060-7065, 2012.

[133] I. Dudchak and L. Piskach, "Phase equilibria in the Cu 2 SnSe 3–SnSe 2–ZnSe system," *Journal of alloys and compounds,* vol. 351, pp. 145-150, 2003.

[134] I. Olekseyuk, I. Dudchak, and L. Piskach, "Phase equilibria in the Cu 2 S–ZnS–SnS 2 system," *Journal of alloys and compounds,* vol. 368, pp. 135-143, 2004.

[135] H. Du, F. Yan, M. Young, B. To, C.-S. Jiang, P. Dippo*, et al.*, "Investigation of combinatorial coevaporated thin film Cu2ZnSnS4. I. Temperature effect, crystalline phases, morphology, and photoluminescence," *Journal of Applied Physics,* vol. 115, p. 173502, 2014.

[136] H. Katagiri, K. Jimbo, M. Tahara, H. Araki, and K. Oishi, "The influence of the composition ratio on CZTS-based thin film solar cells," in *MRS proceedings*, 2009, pp. 1165-M04-01.

[137] A. Redinger, D. M. Berg, P. J. Dale, R. Djemour, L. Gütay, T. Eisenbarth*, et al.*, "Route Toward High-Efficiency Single-Phase Cu \$ _ {\ bf 2} \$ ZnSn (S, Se) \$ _ {\ bf 4} \$ Thin-Film Solar Cells: Model Experiments and Literature Review," *IEEE Journal of Photovoltaics,* vol. 1, pp. 200-206, 2011.

[138] A. Redinger, K. Hönes, X. Fontané, V. Izquierdo-Roca, E. Saucedo, N. Valle*, et al.*, "Detection of a ZnSe secondary phase in coevaporated Cu 2 ZnSnSe 4 thin films," *Applied Physics Letters,* vol. 98, p. 101907, 2011.

[139] D. B. Mitzi, O. Gunawan, T. K. Todorov, K. Wang, and S. Guha, "The path towards a high-performance solution-processed kesterite solar cell," *Solar Energy Materials and Solar Cells,* vol. 95, pp. 1421-1436, 2011.

[140] K. Ito, *Copper zinc tin sulfide-based thin film solar cells*: John Wiley & Sons, 2014.

[141] D. M. Berg, R. Djemour, L. Gütay, G. Zoppi, S. Siebentritt, and P. J. Dale, "Thin film solar cells based on the ternary compound Cu 2 SnS 3," *Thin Solid Films,* vol. 520, pp. 6291-6294, 2012.

[142] G. Marcano, C. Rincon, L. De Chalbaud, D. Bracho, and G. S. Pérez, "Crystal growth and structure, electrical, and optical characterization of the semiconductor Cu 2 SnSe 3," *Journal of Applied Physics,* vol. 90, pp. 1847-1853, 2001.

[143] Y. Peter and M. Cardona, *Fundamentals of semiconductors: physics and materials properties*: Springer Science & Business Media, 2010.

[144] Y.-T. Lin, J.-B. Shi, Y.-C. Chen, C.-J. Chen, and P.-F. Wu, "Synthesis and characterization of tin disulfide (SnS 2) nanowires," *Nanoscale research letters,* vol. 4, p. 694, 2009.

[145] F. Sava, A. Lorinczi, M. Popescu, G. Socol, E. Axente, I. Mihailescu*, et al.*, "Amorphous SnSe~ 2 films," *Journal of optoelectronics and advanced materials,* vol. 8, p. 1367, 2006.

[146] J. Vidal, S. Lany, M. d'Avezac, A. Zunger, A. Zakutayev, J. Francis*, et al.*, "Band-structure, optical properties, and defect physics of the photovoltaic semiconductor SnS," *Applied Physics Letters,* vol. 100, p. 032104, 2012.

[147] P. Sinsermsuksakul, J. Heo, W. Noh, A. S. Hock, and R. G. Gordon, "Atomic layer deposition of tin monosulfide thin films," *Advanced Energy Materials,* vol. 1, pp. 1116-1125, 2011.

[148] M. A. Franzman, C. W. Schlenker, M. E. Thompson, and R. L. Brutchey, "Solution-phase synthesis of SnSe nanocrystals for use in solar cells," *Journal of the American Chemical Society,* vol. 132, pp. 4060-4061, 2010.

[149] G. Liu, T. Schulmeyer, J. Brötz, A. Klein, and W. Jaegermann, "Interface properties and band alignment of Cu 2 S/CdS thin film solar cells," *Thin Solid Films,* vol. 431, pp. 477-482, 2003.

[150] S. Kashida, W. Shimosaka, M. Mori, and D. Yoshimura, "Valence band photoemission study of the copper chalcogenide compounds, Cu 2 S, Cu 2 Se and Cu 2 Te," *Journal of Physics and Chemistry of Solids,* vol. 64, pp. 2357-2363, 2003.

[151] J. Y. Seto, "The electrical properties of polycrystalline silicon films," *Journal of Applied Physics,* vol. 46, pp. 5247-5254, 1975.

[152] C. Persson and A. Zunger, "Compositionally induced valence-band offset at the grain boundary of polycrystalline chalcopyrites creates a hole barrier," *Applied Physics Letters,* vol. 87, pp. 211904-211904-3, 2005.

[153] S. S. Schmidt, "Microscopic properties of grain boundaries in $Cu(In,Ga)_2$ and $CuInS_2$ thin-film solar cells studied by transmission electron microscopy," ed, 2011.

[154] Y. Yan, R. Noufi, and M. Al-Jassim, "Grain-boundary physics in polycrystalline $CuInSe_2$ revisited: experiment and theory," *Physical review letters,* vol. 96, p. 205501, 2006.

[155] M. Hetzer, Y. Strzhemechny, M. Gao, S. Goss, M. Contreras, A. Zunger*, et al.*, "On microscopic compositional and electrostatic properties of grain boundaries in polycrystalline $CuIn_{1-x}Ga_xSe_2$," *Journal of Vacuum Science & Technology B: Microelectronics and Nanometer Structures,* vol. 24, pp. 1739-1745, 2006.

[156] P. Xu, S. Chen, B. Huang, H.-J. Xiang, X.-G. Gong, and S.-H. Wei, "Stability and electronic structure of Cu 2 ZnSnS 4 surfaces: First-principles study," *Physical Review B,* vol. 88, p. 045427, 2013.

[157] Y. Zhu, M. Milas, M.-G. Han, J. Rameau, and M. Sfeir, "Multimodal Optical Nanoprobe for Advanced In-Situ Electron Microscopy," *Microscopy Today,* vol. 20, pp. 32-37, 2012.

[158] J. R. Jokisaari, "Characterization of structure and properties of thin film crystals and ferroelectric BiFeO3-a coupled TEM, SPM, and optical probe approach," University of Michigan, 2016.